# Investigation into the mechanical behaviour of bio-cemented sands using the discrete element method

Zhang, A.

**DOI**
10.4233/uuid:68dbd40d-dfce-4e04-9756-2179c08d6bd3

**Publication date**
2024

**Document Version**
Final published version

**Citation (APA)**
Zhang, A. (2024). *Investigation into the mechanical behaviour of bio-cemented sands using the discrete element method*. [Dissertation (TU Delft), Delft University of Technology]. https://doi.org/10.4233/uuid:68dbd40d-dfce-4e04-9756-2179c08d6bd3

# INVESTIGATION INTO THE MECHANICAL BEHAVIOUR OF BIO-CEMENTED SANDS USING THE DISCRETE ELEMENT METHOD

# INVESTIGATION INTO THE MECHANICAL BEHAVIOUR OF BIO-CEMENTED SANDS USING THE DISCRETE ELEMENT METHOD

## Dissertation

for the purpose of obtaining the degree of doctor
at Delft University of Technology
by the authority of the Rector Magnificus, Prof. dr. ir. T.H.J.J. van der Hagen,
chair of the Board for Doctorates
to be defended publicly on Monday 13 May 2024 at 12:30 o'clock

by

**Aoxi ZHANG**

Master of Engineering in Highway and Railway Engineering,
Sun Yat-sen University, China
born in Hubei, China

This dissertation has been approved by the promotors

Composition of the doctoral committee:

| | |
|---|---|
| Rector Magnificus, | chairperson |
| Prof. dr. ir. T. J. Heimovaara, | Delft University of Technology, promotor |
| Dr. ir. A. C. Dieudonné, | Delft University of Technology, copromotor |
| | |
| Independent members: | |
| Prof. dr. ir. F. Collin, | University of Liège, Belgium |
| Prof. dr. C. O'Sullivan, | Imperial College London, UK |
| Prof. dr. K. G. Gavin, | Delft University of Technology |
| Prof. dr. H. M. Jonkers, | Delft University of Technology |
| Dr. ir. L. A. van Paassen, | Arizona State University, USA / Boskalis |

*Keywords:* Bio-cemented soil, Discrete element method, Mechanical behaviour, Microstructure, Coordination number, Strain localisation, Small–strain stiffness

*Printed by:* Gildeprint Drukkerijen - Enschede

Email: A.Zhang-1@tudelft.nl

ISBN: 978-94-6384-578-6

An electronic version of this dissertation is available at
http://repository.tudelft.nl/.

To my beloved family and everyone who helped me

# CONTENTS

# SUMMARY

Bio-mediated methods, such as microbially induced carbonate precipitation (MICP) and enzyme induced carbonate precipitation (EICP), have gained considerable attention as alternatives to invasive ground improvement techniques. MICP and EICP use biogeochemical processes to drive carbonate precipitation and bind soil grains, thereby improving the mechanical performance of soils. While MICP and EICP have the potential to transform geotechnical engineering, challenges persist, particularly in understanding the spatial distribution of the precipitated minerals and predicting the associated mechanical improvement. This thesis addresses these uncertainties and sheds light on the role of the microstructure on the mechanical behaviour of bio-cemented sands and the effectiveness of the bio-cementation treatment.

To this end, experimental observations on the microstructure of bio-cemented sands are first reviewed. Four typical carbonate distribution patterns are identified depending on the location of the precipitated carbonates with respect to the granular assembly: grain bridging, contact cementing, grain coating, and pore filling. The discrete element method (DEM) is then used to investigate the effect of the aforementioned carbonate distribution patterns on the mechanical behaviour of bio-cemented sands. A toolbox based on the open-source DEM platform YADE, called Cementor, is developed for modelling various crystal distribution patterns and contents.

DEM models of bio-cemented sand samples with different properties, i.e. distribution pattern and mass content of carbonates (up to 3%), are subjected to drained triaxial compression tests under various confinements. It is found that carbonates in the pattern of coating and pore filling have a negligible influence on the mechanical response of the material. In contrast, grain bridging and contact cementing lead to a noticeable improvement in stiffness, peak strength and dilatancy. The difference in the macroscopic behaviour of the cemented samples is explained by microscopic indicators such as the effective coordination number and bond breakage evolution.

Some experimental studies surprisingly show that MICP-treated sands can exhibit a lower residual strength than uncemented sands. Such a phenomenon has been observed experimentally but not explained. The presented DEM model offers insights into this behaviour. It was found that carbonates precipitated in the bridging distribution pattern are more likely to form a metastable structure. This metastable structure is prone to relative movement of particles, which in turn leads to the development of shear bands and, overall, a lower residual strength than the uncemented sample.

The variation in the microscopic properties of bio-cemented sands leads to uncertainty of mechanical improvements gained from bio-mediated treatment. It is crucial to develop a probing method to gain confidence in the treatment. Seismic measurements can be used to probe the treated soil. To evaluate the seismic response of bio-cemented sands, DEM samples with different characteristics, including properties of the host sand (void ratio, uniformity of particle size distribution) and properties of the precipitated minerals (distribution pattern, content, Young's modulus), are modelled and subjected to static probing to examine the small-strain stiffness. These factors are all found to affect the small-strain stiffness of bio-cemented sands, hence, the seismic response. Microscopic analysis indicates that there are two mechanisms which, together, determine the overall efficiency in improving the small-strain stiffness of bio-cemented sands: the number of effective bonds and the ability of a single bond to improve stiffness.

This thesis contributes to the understanding of the macroscopic mechanical behaviour of bio-cemented sands from the microscopic point of view. In particular, the role of crystal distribution patterns is highlighted by explicitly modelling the precipitated carbonates in pre-defined locations. The findings of this thesis can support the prediction of the mechanical behaviour of bio-cemented soils and guide the design of MICP/ EICP treatment.

# SAMENVATTING

Bodemverbeteringsmethoden, zoals microbieel geïnduceerde carbonaatprecipitatie (MICP) en enzym geïnduceerde carbonaatprecipitatie (EICP), hebben aanzienlijk meer aandacht gekregen als alternatief voor invasieve grondverbeteringstechnieken. De methoden MICP en EICP maken gebruik van bio-geo-chemische processen om carbonaatprecipitatie aan te sturen en bodemkorrels te binden waardoor de grondmechanische prestaties van bodems worden verbeterd. Hoewel MICP en EICP het potentieel hebben om de geotechniek te transformeren, wordt de praktische inzet van deze methoden verhinderd door verscheidene onzekerheden. In het bijzonder is er onzekerheid in de ruimtelijke verdeling van de neergeslagen mineralen en, daaropvolgend, de verkregen grondmechanische verbeteringen. Dit proefschrift gaat in op deze onzekerheden en werpt een licht op de invloed van bodemstructuur op het mechanisch gedrag van bio-gecementeerd zand en de effectiviteit van bio-cementatiebehandelingen.

Hiertoe behandelt dit proefschrift de volgende zaken. Experimentele observaties van de microstructuur van bio-gecementeerd zand zijn beoordeeld waarbij vier typische carbonaatverdelingspatronen zijn geïdentificeerd, afhankelijk van de locatie van de neergeslagen carbonaten ten opzichte van het korrelskelet: korreloverbrugging, contactcementering, korrelcoating en poriënvulling. Om onderzoek te doen naar de impact van deze patronen op het grondmechanisch gedrag, is de discrete-elementenmethode (DEM) toegepast om fundamenteel begrip te krijgen van het mechanische gedrag van bio-gecementeerd zand. In dit proefschrift is een DEM-toolbox ontwikkeld, gebaseerd op het open-source DEM-platform YADE. Deze toolbox kan gebruikt worden voor het modelleren van verschillende kristaldistributiepatronen.

DEM-modellen van bio-gecementeerde zandmonsters zijn onderworpen aan gedraineerde triaxiaal-compressieproeven onder verschillende spanningsniveaus. Voor deze zandmonsters is gevarieerd met het distributiepatroon en het massagehalte van carbonaten (tot 3%). Modellering wijst uit dat carbonaten in het coatingpatroon slechts in geringe mate bijdragen aan verbeteringen in de grondmechanische eigenschappen, en dat poriënvulling hier een verwaarloosbare invloed op heeft. Carbonaten die neerslaan in patronen van brugvorming en contactcementering leiden daarentegen tot een merkbare verbetering in stijfheid, piekste rkte en dilatantie van de gecementeerde monsters. Het verschil in macroscopisch gedrag kan worden verklaard aan de hand van microscopische indicatoren, zoals het coördinatiegetal en de evolutie van de bindingsbreuk.

Sommige experimentele onderzoeken tonen verrassenderwijs aan dat met MICP behandeld zand in de resttoestand een lagere sterkte kan vertonen dan ongecementeerd zand. Een dergelijk fenomeen is experimenteel waargenomen, maar niet verklaard. Het gepresenteerde DEM-model biedt inzicht in dit gedrag. Zo is uit modellering ondervonden dat carbonaten die neerslaan in het overbruggende distributiepatroon eerder een metastabiele structuur vormen. Deze metastabiele structuur is gevoelig voor relatieve bewegingen van deeltjes, wat op zijn beurt leidt tot afschuiving, en, voor het gehele ongecementeerde monster, een lagere reststerkte.

Variaties in de bodemstructuur van biogecementeerde zandgronden leiden tot een algehele onzekerheid in de grondmechanische verbetering die kan worden verkregen door het toepassen van biogemedieerde behandelingen. Het is van cruciaal belang om een onderzoeksmethode te vinden die deze onzekerheden kan reduceren. De seismische meting kan worden gebruikt om effectiviteit van de behandeling te onderzoeken. Om de seismische respons van bio-gecementeerd zand te evalueren zijn DEM-monsters met verschillende kenmerken, waaronder eigenschappen van het ontvangende zandmonster (poriëngehalte, uniformiteit van de korrelverdeling) en eigenschappen van de neergeslagen mineralen (verdelingspatroon, gehalte, Young's modulus) gebruikt. Om de stijfheid bij kleine rekken te onderzoeken is de grondrespons gemodelleerd bij een statische sondering. De gevarieerde eigenschappen blijken allemaal van invloed te zijn op de stijfheid bij lage korrelspanning, en dus op de seismische respons. Microscopische analyse van de bodemstructuur wijst uit dat er twee mechanismen bepalend zijn voor de verbetering van de stijfheid van biogecementeerd zand onder lage korrelspanningen: het aantal effectieve bindingen dat wordt aangegaan, en het vermogen van een enkele binding om de stijfheid te verbeteren.

Dit proefschrift draagt bij aan het begrip van grondmechanisch gedrag van biogecementeerd zand door het analyseren van de bodemstructuur na een biogemedieerde behandeling. In het bijzonder wordt de rol van kristalverdelingspatronen benadrukt door de neergeslagen carbonaten expliciet te modelleren op vooraf gedefinieerde locaties. De bevindingen van dit proefschrift kunnen worden ingezet om het grondmechanische gedrag van bio-gecementeerde bodems beter te voorspellen en daarmee MICP/EICP-behandelingen te ondersteunen.

# 1

# INTRODUCTION

## 1.1. BACKGROUND

Land resources have become increasingly limited due to continued population growth and the demands of human activities. According to the United Nations, the world's population reached 8 billion in mid-November 2022 and is expected to grow by nearly 2 billion over the next 30 years. At the same time, there is a huge demand for infrastructure to support the growing population. This demand is even greater in major cities. Land resources, as the basis of human activity, are precious. However, land resources are limited by, among others, the presence of soils with poor mechanical properties, which cannot be directly used for construction. Consequently, these soils need to be reinforced to improve their mechanical properties before use, a process usually referred to as soil or ground improvement.

Conventional soil improvement techniques include jet grouting, deep mixing, dynamic compaction and sand or stone columns. These techniques have several advantages. In particular, the required materials (e.g. Portland cement used in jet grouting and deep mixing) are widely available at relatively low cost, which makes these conventional techniques widely used in geotechnical engineering. However, these techniques also suffer from limitations. For example, the production of Portland cement is an energy-intensive process, which releases large amounts of $CO_2$, which accelerates global warming (Worrell *et al.*, 2001; Jonkers *et al.*, 2010). Some synthetic materials used in chemical grouting are toxic, leading to water pollution. In addition, most conventional soil improvement techniques are invasive and can disturb the surrounding structures and environment. Therefore, they cannot be used in heavily urbanised or protected natural environments.

Geotechnical engineers are always looking for efficient, economical and sustainable methods for ground improvement. With the aim of reaching net-zero emissions by 2050, technologies without carbon emissions or with low carbon emissions are even more urgently needed. Inspired by natural bio-mineralisation processes, bio-mediated methods have been developed and introduced to geotechnical engineering for soil improvement. Microbially induced carbonate precipitation (MICP) and enzyme induced carbonate precipitation (EICP) belong to this family of methods. They use biological processes to drive carbonate precipitation and cement soils, thereby improving their mechanical performance. MICP and EICP have demonstrated the capability for ground improvement (van Paassen *et al.*, 2010; Zeng *et al.*, 2021), liquefaction mitigation (Xiao *et al.*, 2018; Darby *et al.*, 2019), protection against soil erosion (Salifu *et al.*, 2016; Jiang & Soga, 2017; Shahin *et al.*, 2020; Clarà Saracho *et al.*, 2021; Wang *et al.*, 2023), dust control (Hamdan & Kavazanjian Jr, 2016), heavy metal removal (Li *et al.*, 2013, 2016; Chen *et al.*, 2017; Zeng *et al.*, 2023), remediation of desiccation cracking (Liu *et al.*, 2020). Compared to the aforementioned conventional ground improvement methods, this family of methods consumes less energy (DeJong *et al.*, 2013) and causes less disturbance to the surrounding infrastructures during the treatment (He *et al.*, 2019). In addition, the needed ingredients are injected in solution form, which exhibits low viscosity, thus making MICP or EICP possible for long-distance treatment. Despite these advantages, it should also be noted that MICP and EICP through urea hydrolysis produce ammonium as a by-product, which causes environmental concerns if ammonium accumulates in soils and groundwater. Therefore, post-treatment for removing $NH_4^+$ is needed to make MICP and EICP potential eco-friendly alternatives to conventional soil improvement methods (Lee *et al.*, 2019).

## 1.2. BRIEF INTRODUCTION TO MICP AND EICP TREATMENTS

### 1.2.1. FROM PROCESSES TO IMPLEMENTATION

Microbially induced carbonate precipitation (MICP) and enzyme induced carbonate precipitation (EICP) use biogeochemical processes to drive carbonate precipitation. Several pathways exist for the production and precipitation of calcium carbonate, of which urea hydrolysis is probably the most regarded in ground engineering. In its simplest form, the main processes involved in MICP and EICP through urea hydrolysis can be described by the following reaction:

$$CO(NH_2)_2 + Ca^{2+} + 2H_2O \xrightarrow{\text{urease}} 2NH_4^+ + CaCO_3\downarrow \tag{1.1}$$

In the presence of dissolved calcium (generally provided by a solution of calcium chloride), the carbonate ions resulting from urea hydrolysis combine with calcium ions to precipitate in the form of calcium carbonate. Note that urease is necessary to catalyse the hydrolysis of urea. The enzyme is directly used in EICP, while urease-producing bacteria (e.g. *Sporosarcina pasteurii*) are used in MICP. Finally, as noted in the previous section, ammonium is generated as a by-product of ureolysis.

Figure 1.1 illustrates how MICP and EICP treatments can be implemented in the field. Solutions of calcium chloride and urea are injected through an injection well. In the case of MICP or EICP, urease-producing bacteria or urease is also injected into the subsurface. As the bio-mineralisation process takes place, calcium carbonate particles precipitate in the pore space and can bond soil grains, leading to an improvement in the soil mechanical properties. It should be noted that bio-cementation is most effective in granular materials (especially sand) where permeability is sufficient to allow easy transport of the substrates and pores are sufficiently large for bacterial growth. Therefore, both terms sand and soil are used interchangeably in this thesis.

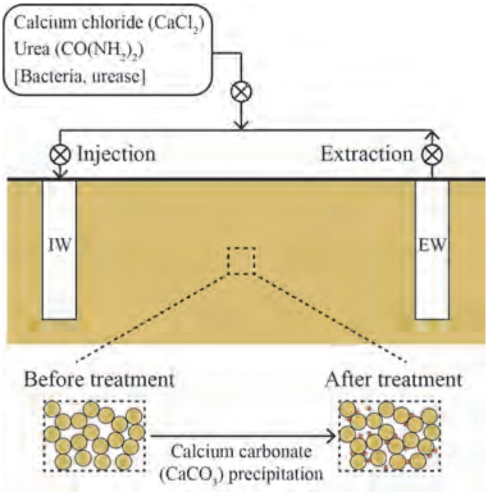

Figure 1.1: Illustration of an MICP or EICP treatment. IW stands for the injection well and EW stands for the extraction well. Adapted from Zeng *et al.* (2022).

Four activities are involved in the development of an optimal MICP or EICP treatment, as demonstrated in Figure 1.2: the definition and implementation of a treatment programme, monitoring and characterisation, performance evaluation and optimisation. These four steps are part of a cycle. Starting from, for instance, the treatment programme, a set of input variables needs to be defined. These include the concentration of the cementation solution, bacterial culture, pH, and the number of injection cycles. The design of the treatment programme is crucial to achieve satisfactory performance of bio-cemented soils, as it affects the size, morphology, spatial distribution and distribution pattern of the precipitated crystals, hence the engineering properties of bio-cemented soils (Al Qabany & Soga, 2013; Dhami *et al.*, 2013; Cheng *et al.*, 2019; Xiao *et al.*, 2021b). During the treatment, various tools can be used to monitor the process of bio-cementation in laboratory experiments or field tests. These include X-ray micro-computed tomography (micro-CT) to characterise the size, spatial distribution and distribution pattern of the precipitated crystals (Dadda *et al.*, 2017; Terzis & Laloui, 2018, 2019a), X-ray diffraction (XRD) to characterise the morphology of the precipitated crystals (van Paassen, 2009; Xu *et al.*, 2020; Saracho *et al.*, 2021; Ma *et al.*, 2022), and seismic measurements to monitor the seismic response in the laboratory and field scales (van Paassen *et al.*, 2010). The information obtained in this part supports the understanding and modelling of the bio-chemo-hydro-mechanical processes affecting the soil, and the evaluation of the engineering performance of the bio-cemented soils. If the performance of the treated soils does not meet the objective (e.g. the target strength needed for the application), an optimisation process follows, in which actions such as tuning the injection cycles and adjusting the treatment programme are needed. More detailed reviews of the design of treatment programme, optimisation and applications of bio-cementation methods can be found in DeJong *et al.* (2013), Phillips *et al.* (2013), Terzis & Laloui (2019b), Tang *et al.* (2020), Yu *et al.* (2022), Kumar *et al.* (2023) and Liu *et al.* (2023), among others. The bio-cementation treatment cycle is deemed complete once the objective is achieved.

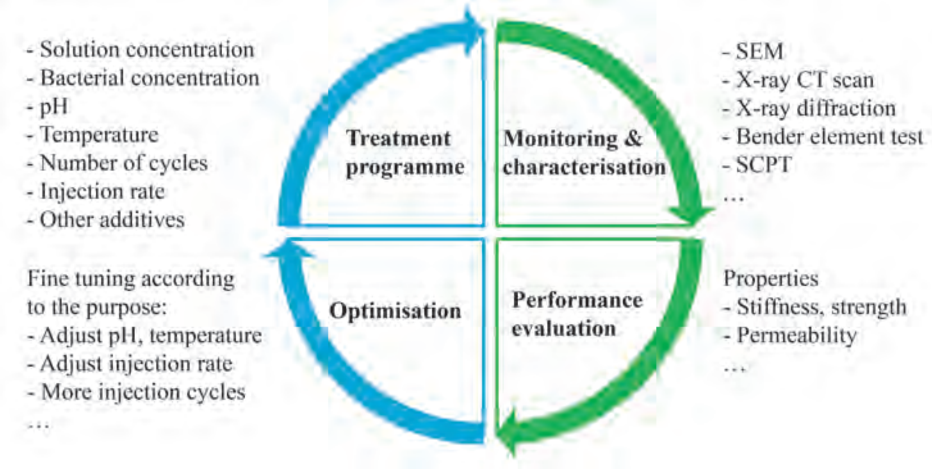

Figure 1.2: Illustration of a complete MICP or EICP treatment. The contributions of this thesis lie in the parts indicated in green.

### 1.2.2. MECHANICAL PROPERTIES OF BIO-CEMENTED SOILS

As mentioned above, the precipitation of calcium carbonate leads to an improvement in the mechanical performance of soils. The main features of the mechanical behaviour of bio-cemented soils are presented in this section.

A set of uniaxial compressive strength (UCS) data of soils treated by MICP (van Paassen *et al.*, 2010; Cheng *et al.*, 2013; Mujah *et al.*, 2019; Hoang *et al.*, 2018; Terzis & Laloui, 2019a) is plotted against the carbonate content in Figure 1.3. The UCS directly reflects the magnitude of strength improvement of a specimen upon bio-treatment, as sands being cohesionless granular materials exhibit a null uniaxial compressive strength.

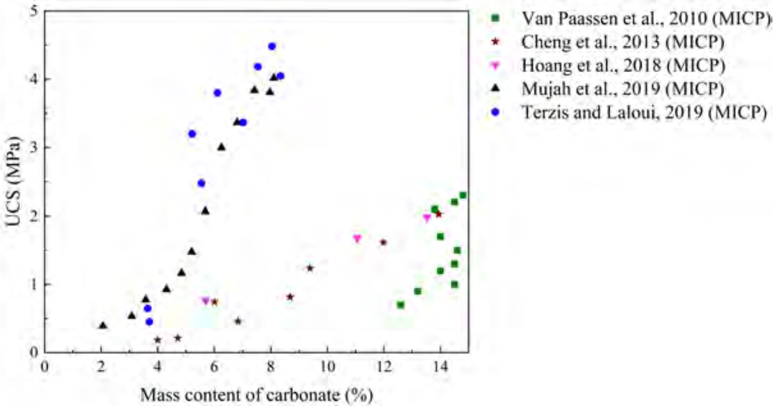

Figure 1.3: Experimental results on the variation of uniaxial compression strength (UCS) with carbonate content of bio-cemented soils.

The following conclusions can be drawn from Figure 1.3:

- The uniaxial compressive strength increases with increasing $CaCO_3$ content, for a given soil and treatment protocol.
- The relationship between the uniaxial compressive strength and the carbonate content is not unique. Among others, differences in treatment performance can be attributed to differences in the host sand properties (e.g. particle size distribution, initial void ratio) and treatment programme (e.g. urease activity and cementation solution). Relevant information concerning the data reported in Figure 1.3 is summarised in Table 1.1.
- The general trend mentioned above is not always true. Within the same testing campaign, the uniaxial compressive strength can vary in a large range even for the same $CaCO_3$ content. For example, in van Paassen *et al.* (2010), for a carbonate content of around 14%, the UCS varies from 1.2 to 2.1 MPa. Moreover, very high $CaCO_3$ contents can even lead to a lower UCS than less cemented samples, within the same testing campaign.

Table 1.1: Experimental test information from the literature.

| Experiment | Soil properties | $e_0$ | BS (U/ml) | CS (mol/L) |
|---|---|---|---|---|
| van Paassen *et al.* (2010) | $D_{50} = 0.166$ mm<br>$C_u = 1.64$ | NR | 18.3 | 1 |
| Cheng *et al.* (2013) | $D_{50} = 0.68$ mm<br>$C_u = 1.33$ | 0.64 | 10 | 1 |
| Mujah *et al.* (2019) | $D_{50} = 0.25$ mm<br>$C_u = 1.65$ | 0.67 | 32 | 0.25 |
| Hoang *et al.* (2018) | $D_{50} = 0.36$ mm<br>$C_u = 1.63$ | 0.58 | 4 to 5 | 0.3 |
| Terzis & Laloui (2019a) | $D_{50} = 0.39$ mm<br>$C_u = 1.6$ | 0.69 | NR | 0.25 |

Note: $e_0$ is the initial void ratio. BS stands for bacteria solution and is described by the urease activity (U), with 1 U = 1 $\mu$mol urea hydrolysed per minute. CS stands for cementation solution and consists of equimolar urea and $CaCl_2$. NR means not reported. $D_{50}$ is the grain size for which 50% of the grains by weight are finer. $C_u$ is the uniformity coefficient.

The mechanical behaviour of bio-cemented soils under different stress conditions has been evaluated by conducting triaxial compression tests. Figure 1.4 presents the stress-strain response and volumetric response of bio-cemented soils with different $CaCO_3$ contents subjected to drained triaxial compression test under two different confining pressures (Nafisi *et al.*, 2020). The main findings are summarised as follows.

- Bio-cemented soil shows an obvious increase in stiffness. In addition, higher $CaCO_3$ content leads to higher stiffness values. This trend is observed at both confining pressures presented in Figure 1.4.

- The peak strength of bio-cemented soils is higher than that of the untreated soils at the same confining pressure. The peak strength increases with both $CaCO_3$ content and confining pressure. The residual strength of lightly bio-cemented soils is approximately the same as that of uncemented soils at a confining pressure of 100 kPa. On the other hand, the moderately and heavily bio-cemented soils exhibit higher residual strength than the uncemented soil. In addition, the difference between the peak and residual strengths, which describes the brittleness of the specimen, increases with the $CaCO_3$ content.

- Bio-cemented soils exhibit higher dilatancy than untreated soils. The improvement in dilatancy increases with $CaCO_3$ content but decreases with confining pressure.

The experimental results described above indicate that soils treated with MICP and EICP can exhibit an increase in soil stiffness, strength and dilatancy. The extent of the mechanical improvement of bio-cemented soil is related to the amount of precipitated carbonates, but there is no direct and unique relationship between both. In addition, the

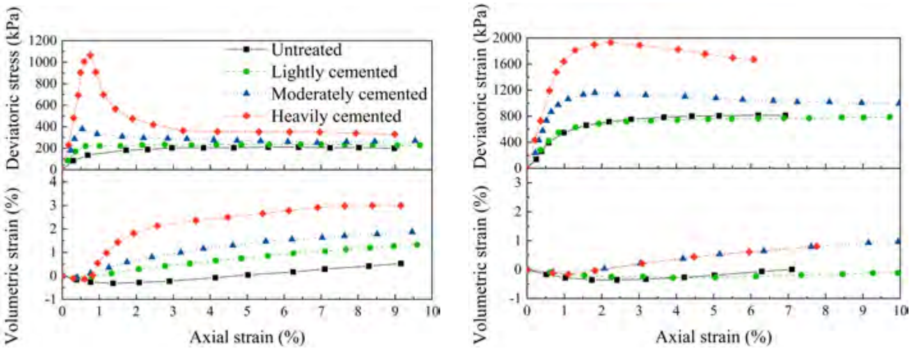

(a) (b)

Figure 1.4: Stress-strain behaviour and volumetric response of bio-cemented samples subjected to a drained triaxial compression test under a confining pressure of (a) 100 kPa and (b) 400 kPa, data adopted from Nafisi *et al.* (2020). The lightly cemented sample corresponds to a carbonate content by mass of 0.7 %, and the moderately and heavily cemented sample corresponds to a carbonate content of 2% and 2.6%, respectively.

constitutive relationship of bio-cemented soil shows a complex behaviour, with strain hardening or strain softening behaviour, depending not only on the properties of the soil to be treated, but also on the confinement and the calcium carbonate content. This thesis aims to improve the understanding of the complex mechanical behaviour of bio-cemented soils.

## 1.3. MOTIVATION AND RESEARCH OBJECTIVES

As discussed in Section 1.2.2, soils treated by MICP and EICP generally show improvements in mechanical properties. One of the critical challenges hindering the practical application of these techniques is the uncertainty of the mechanical improvements (van Paassen *et al.*, 2010; Krishnan *et al.*, 2021; Montoya *et al.*, 2021; Xiao *et al.*, 2021b). Indeed, this uncertainty makes it difficult to predict and rely on the mechanical behaviour of bio-treated soils. To remove the barriers and facilitate the application of MICP and EICP, a fundamental understanding of the mechanical behaviour of bio-cemented soils is essential.

It is widely accepted that the macroscopic mechanical behaviour of soil is dominated by its microscopic characteristics. To gain fundamental insights into the mechanical behaviour of bio-cemented soils, it is important to consider the micro-scale properties of bio-cemented soils. Accordingly, this thesis aims to contribute to the understanding of the mechanical behaviour of bio-cemented sands by focusing on the impact of the microscopic properties on the global soil response. The findings are expected to guide the design for MICP and EICP treatment and thus facilitate the applications of these techniques. Specifically, the key objectives of this thesis are to:

1. Characterise the microstructure of bio-cemented soils, with a particular focus on the typical distribution patterns of precipitated carbonates.
2. Develop a discrete element modelling (DEM) algorithm to study bio-cemented

sands with various carbonate distribution patterns and their combinations, as well as different calcium carbonate contents.

3. Evaluate how each carbonate distribution pattern affects the stress-strain and volumetric responses of bio-cemented sands under various loading conditions.

4. Pave the basis for exploring a way to probe the effectiveness and efficiency[1] of MICP and EICP treatment.

Overall, the contribution of this thesis lies in the monitoring and characterisation part and performance evaluation part of an MICP or EICP treatment, as shown in Figure 1.2. The findings of this thesis are expected to support the design and optimisation of the treatment, hence facilitating the practical applications of MICP or EICP.

## 1.4. THESIS OUTLINE

This thesis consists of 6 chapters organised as follows:

Chapter 2 describes and conceptualises the microstructure of bio-cemented sands as observed experimentally. The microstructure of bio-cemented sands is characterised by the distribution of the precipitated carbonate crystals with respect to the granular skeleton. An open-source toolbox, called Cementor, is then developed to model bio-cemented sands with different microstructures using the discrete element method.

In Chapter 3, bio-cemented samples with different carbonate distribution patterns are prepared utilising the toolbox developed in Chapter 2. These samples are subjected to drained triaxial compression to evaluate the impact of carbonate distribution patterns on the mechanical behaviour of bio-cemented sands. The effects of the carbonate distribution pattern, carbonate content and confining pressure are investigated. The macroscopic mechanical behaviour of bio-cemented sands with different carbonate distribution patterns is understood from the microscopic point of view. In particular, an effective coordination number is proposed to describe microstructures of bio-cemented soils accounting for different distribution patterns of cement agents. A detailed comparison between the effective coordination number, the widely-used coordination number and the mechanical coordination number is presented in Appendix A.

In Chapter 3, the bio-cemented samples with a certain carbonate distribution pattern was found to exhibit a lower residual strength than that of the untreated sand. This a priori unexpected behaviour is also reported in the literature, although it has not been explained. Therefore, Chapter 4 sheds light on the residual strength of bio-cemented sands. The residual strength of DEM samples with a given carbonate distribution pattern is systematically evaluated. Factors that may affect the residual strength of bio-cemented sands are investigated. The underlying mechanisms are analysed based on observations across scales.

Carbonates precipitated in different distribution patterns show distinct effectiveness and efficiency in mechanical improvements, leading to uncertainty in mechanical improvements after treatment. Therefore, it is important to evaluate the performance of the

---

[1] In this thesis, the effectiveness is defined as the capacity to produce a desired result. In particular, an MICP treatment is considered effective if it leads to mechanical improvement. Mechanical efficiency refers to the extent of mechanical improvement resulting from the precipitation of a given mass of the carbonate.

treatment using tools that be deployed in the field, such as geophysical measurement. Chapter 5 investigates the small-strain stiffness of bio-cemented sands, aiming at supporting the use of geophysical measurements to assess the efficiency and effectiveness of MICP treatment. In this chapter, sand samples with different characteristics (particle size distribution and dense state) are generated and cemented numerically. The mechanical response of bio-cemented samples at small strains is evaluated. The difference in effectiveness and efficiency of bio-cementation with different characteristics is understood from the microscopic analysis.

Finally, Chapter 6 summarises the main conclusions of this thesis. In addition, recommendations for future research are presented.

# 2

# CONCEPTUALISATION AND DEM MODELLING OF BIO-CEMENTED SANDS

---

Parts of this chapter have been published in Zhang & Dieudonné (2023b) and Zhang & Dieudonné (2024).

## 2.1. INTRODUCTION

In recent decades, bio-cementation soil improvement methods have attracted significant attention as alternatives to conventional stabilisation techniques. These methods, which include microbially induced carbonate precipitation (MICP) and enzyme induced carbonate precipitation (EICP), use biogeochemical processes to drive carbonate precipitation and cement soil grains, thereby improving the material mechanical performance. Soils treated through MICP or EICP exhibit an increase in stiffness, strength and dilatancy (see van Paassen *et al.*, 2010; Al Qabany & Soga, 2013; Montoya & Dejong, 2013; Chu *et al.*, 2014; Cheng *et al.*, 2016; Hoang *et al.*, 2018; Liu *et al.*, 2019; Terzis & Laloui, 2019a; Tang *et al.*, 2020; Nafisi *et al.*, 2020; Xiao *et al.*, 2021b, among others), yet often with variable magnitudes, even at equal calcium carbonate contents. Several reasons can explain this variability: differences in distribution patterns of the precipitated minerals (DeJong *et al.*, 2010; Lin *et al.*, 2016; Mujah *et al.*, 2017; Wang *et al.*, 2022), precipitation of different polymorphs of calcium carbonate (i.e. vaterite, aragonite or calcite) or amorphous calcium carbonate (van Paassen, 2009; Terzis & Laloui, 2019b), and inhomogeneity of the treated samples (Xiao *et al.*, 2021b; Zhang & Dieudonné, 2023b).

This chapter sheds light on the distribution patterns of the precipitated carbonates. Carbonate particles distributed in different patterns may contribute differently to the mechanical performance of bio-cemented soils and hence account for the variability of improvement. However, in practice, bio-cemented soil samples exhibit complex combinations of distribution patterns so that the effects of carbonate distribution patterns cannot be easily assessed experimentally. Therefore, numerical modelling is needed as an important step towards a better understanding of the material behaviour and thus facilitating the applications of MICP.

The discrete element method (DEM) is preferred as it can model granular materials with abundant microscopic details. Two approaches have been used to model cemented soils using the discrete element method in previous studies. The most commonly adopted approach consists of simulating the effects of cementation by introducing virtual bonds (such as parallel bonds) between soil grains (Utili & Nova, 2008; Shen *et al.*, 2016; Feng *et al.*, 2017; Yang *et al.*, 2019). This method implicitly assumes contact cementing between grains. Overall, the approach is able to capture some features of cemented soils, such as the increase in peak strength and dilatancy, but may lead to an underestimation of the ultimate strength as the bonds disappear after breakage (Feng *et al.*, 2017). Furthermore, the mass content of carbonate is only taken into account implicitly in the model. An alternative modelling approach is representing the cement agents using real particles (Wang & Leung, 2008a,b; Evans *et al.*, 2014; Li *et al.*, 2017; Khoubani, 2018). In this case, different distribution patterns and the mass content of calcium carbonate can be taken into account, leading, among others to a better representation of the post-peak behaviour. The main drawback of this approach is the computational cost associated with the increased number of particles.

In this chapter, typical microstructures of bio-cemented sands are characterised and conceptualised in Section 2.2. Section 2.3 briefly introduces the background of the methodology used in this thesis. In Section 2.4, an open-source toolbox named Cementor is developed to model bio-cemented sands with various microstructures which are explicitly represented in 3D DEM. Illustrative examples are given in Section 2.5.

## 2.2. MICROSTRUCTURE CHARACTERISATION

### 2.2.1. CRYSTAL DISTRIBUTION PATTERNS

Microscopic observations using scanning electron microscopy (SEM) (van Paassen, 2009; Al Qabany & Soga, 2013; Feng & Montoya, 2015; Lin *et al.*, 2016; Hoang *et al.*, 2018; Mahawish *et al.*, 2018; Cheng *et al.*, 2019; Xiao *et al.*, 2021a) and X-ray micro-CT scanning (Dadda *et al.*, 2017; Terzis & Laloui, 2018; Saracho *et al.*, 2021) have shown that bio-cemented soils exhibit various microstructures depending on the pore-scale distribution of the precipitated calcium carbonate crystals with respect to the host granular skeleton. In general, four typical carbonate distribution patterns can be identified, which are illustrated in Figure 2.1, namely bridging, contact cementing, grain coating and pore filling. Specifically,

- In the case of a bridging distribution (Figure 2.1(a)), calcium carbonate crystals are located at the gap between sand grains and connect sand grains.
- In the case of contact cementing (Figure 2.1(b)), calcium carbonate particles are located around sand-sand contacts, forming a cement chain.
- For grain coating (Figure 2.1(c)), carbonates are attached to the surface of sand grains.
- In the case of pore filling, carbonate particles are distributed in the pore space of the host sand and do not bind sand grains (Figure 2.1(d)).

Note that in the case of contact cementing, the cemented sand grains are already in contact with each other prior to cementation, while the bridging type of distribution corresponds to the formation of carbonate bonds between sand grains which were initially not in contact. The conceptualised microstructures are further reproduced in 3D DEM, in which both sand and carbonate particles are idealised as spheres, as shown in Figure 2.1. More details on DEM modelling are given in Section 2.4.

Several factors are known to affect the distribution pattern of calcium carbonates and can be partly controlled. These include the treatment conditions, such as the concentration of the injected solutions (Okwadha & Li, 2010; Al Qabany *et al.*, 2012; Cheng *et al.*, 2019) and the solution pH (Okwadha & Li, 2010), the use of additional ingredients such as powdered milk (Almajed *et al.*, 2019), soil properties (e.g. particle size distribution) (Lin *et al.*, 2016), its degree of saturation (Cheng *et al.*, 2013), temperature (Cheng *et al.*, 2016). For instance, Cheng *et al.* (2019) found that urease activity can affect the distribution pattern of the precipitated crystals, and that $CaCO_3$ is majorly accumulated at the gaps between sand grains for treatment with a low urease activity (1.25 U/mL). Cheng *et al.* (2016) found that crystals from MICP treatment at 50°C were more likely to cover the surface of the sand grains as a coating-like layer. By contrast, for MICP treatment at ambient temperature, parts of the crystals were found to cover the contact areas of sand grains.

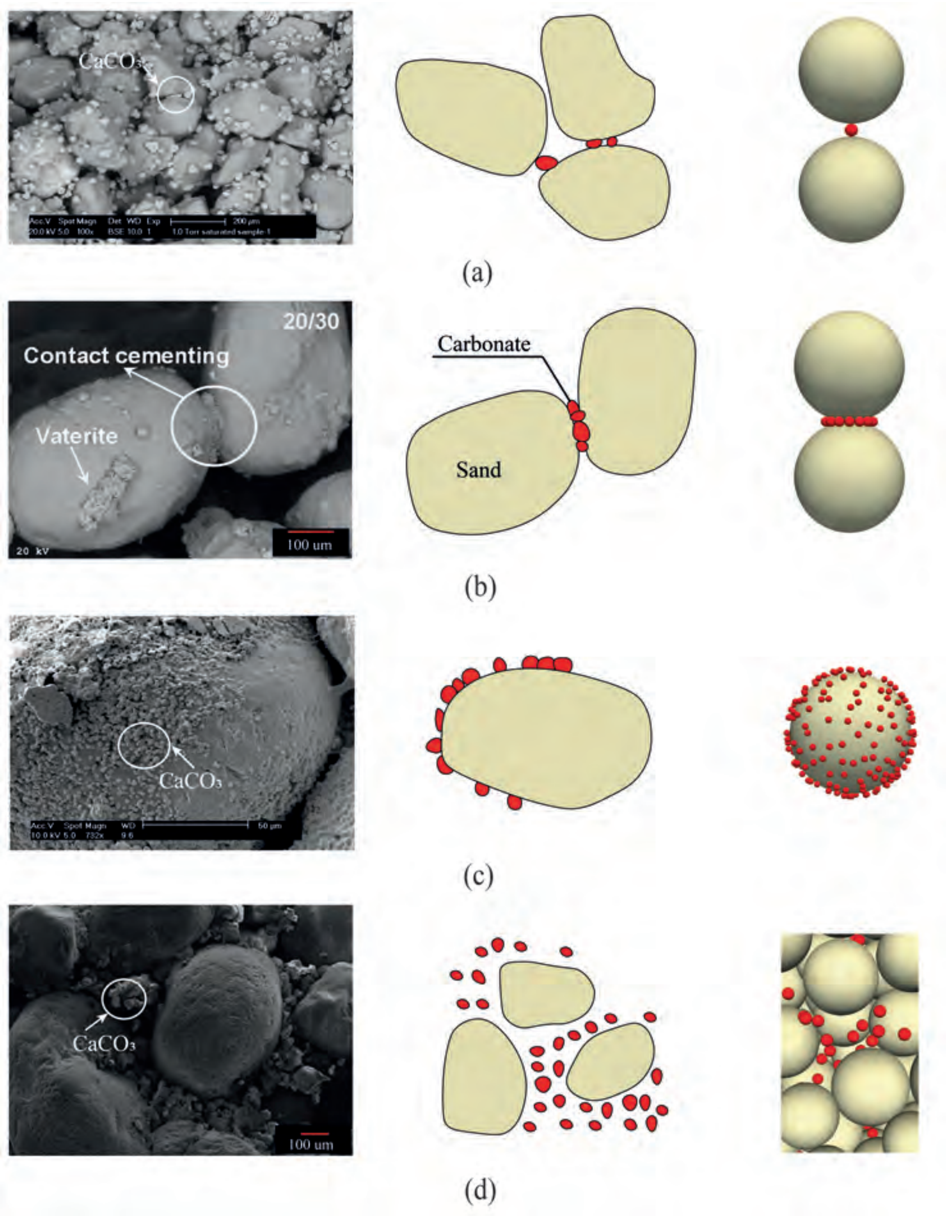

Figure 2.1: Microstructure (left), conceptualisation (middle) and idealisation in DEM (right) of the four distribution patterns: (a) bridging (SEM image from van Paassen (2009)), (b) contact cementing (SEM image from Lin *et al.* (2016)), (c) grain coating (SEM image from Cheng *et al.* (2016)) and (d) pore filling (SEM image from Wu *et al.* (2021)).

### 2.2.2. SIZE OF THE PRECIPITATED CRYSTALS

The sizes of the precipitated crystals can be measured from SEM images and micro-CT scans. Cheng *et al.* (2016) investigated the microstructure of bio-cemented sands using SEM and found that treatment temperature affects the typical crystal size. For sand samples treated by MICP at ambient temperature, the size of the precipitated crystals ranges from 20 to 50 µm. The crystals are smaller for samples treated at 50°C, with typical sizes of 2-5 µm. A similar size range of crystals was also reported by van Paassen (2009). Besides temperature, crystal size is also affected by other factors. It was found by Mujah *et al.* (2019) that the size of $CaCO_3$ crystals varies with bacteria concentration and cementation concentration (which is the equimolar amount of urea and calcium). Treatment with high bacteria concentration (32 U/mL) and low cementation concentration (0.25 M, M for molarity) led to $CaCO_3$ crystals over 20 µm. By contrast, the size of $CaCO_3$ crystals is relatively smaller (less than 10 µm) for treatment with a combination of high bacteria (32 U/mL) and high cementation concentration (1 M). Ma *et al.* (2022) observed the crystal sizes varied from 0.25 µm to 150 µm depending on the reaction conditions. The larger calcite was formed at low bacterial density, while crystals with relatively small sizes were observed at high bacterial density.

## 2.3. DISCRETE ELEMENT METHOD

### 2.3.1. BACKGROUND

The discrete element method (DEM) has been widely used for modelling granular materials such as powders and soils since it was proposed by Cundall & Strack (1979). The main reasons for using DEM in this thesis include that:

- DEM allows precise control of sample characteristics, including void ratio, particle size distribution and fabric, which cannot be easily controlled, if at all possible, in experiments.
- DEM can provide full access to the particle-scale information, which benefits the understanding of the macroscopic material behaviour from a microscopic perspective.

Despite these advantages, DEM is computationally costly, which has limited its application to large-scale engineering projects. Recent developments in the computing power of processors, as well as parallel computing and GPU (graphics processing unit) acceleration benefit DEM simulations.

A DEM simulation proceeds by continuously looping the following steps (O'Sullivan, 2011):

1. Contact detection: knowing the positions and geometry (radius) of all discrete particles at the current time step, contacts between two particles can be detected.
2. Solving interaction forces: for all the contacts, the interaction forces are calculated according to predefined contact law. The contact law used in DEM simulations presented in this thesis will be introduced in the corresponding chapter.

3. Force integration: for each particle, the forces and torques acting on that object are integrated, and the acceleration of each particle is calculated according to Newton's second law.

4. Updating positions: the displacement and rotation of each particle are computed by integrating its acceleration and updating its position.

### 2.3.2. DEM MODELLING OF BIO-CEMENTED SOILS

To model the effect of cementation in soils using DEM, the most common approach is to implicitly model the cementation agents by directly introducing cohesive bonds between sand grains. Such approach was adopted in Utili & Nova (2008), Jiang *et al.* (2014) and Shen *et al.* (2016), among others. The general idea of this approach is illustrated in Figure 2.2. Using this approach, Feng *et al.* (2017) and Yang *et al.* (2017, 2019) carried out DEM studies on bio-cemented sands. The main features of the mechanical behaviour of bio-cemented sands, namely the increase in stiffness and strength as compared to the uncemented sample, were captured in their DEM models, demonstrating that DEM is an effective tool for studying the mechanical behaviour of bio-cemented sands. Besides the reproduction of the macroscopic mechanical behaviour of bio-cemented sand, Feng *et al.* (2017) gave insights into the evolution of microscale quantities such as the coordination number (which describes the average number of contacts per particle), bond breakage ratio (which is the ratio of number of broken bonds and number of bonds at initial stage) during the triaxial compression tests. The results were discussed and compared to experimental results, showing a good match. Yang *et al.* (2017, 2019) focused on the evolution of contact force distribution of DEM bio-cemented samples subjected to drained triaxial compression (Yang *et al.*, 2017) and undrained one (Yang *et al.*, 2019), respectively. It is worth pointing out that a rigid wall boundary was used for triaxial compression simulations in both Feng *et al.* (2017) and Yang *et al.* (2017), while Yang *et al.* (2019) implemented a flexible boundary for triaxial compression simulation. The authors found that the brittle behaviour of heavily bio-cemented sand was captured by using flexible boundary walls, which overcame the limitation of rigid wall boundary.

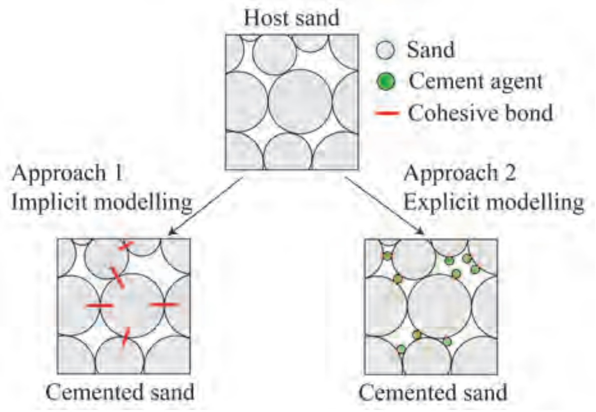

Figure 2.2: Illustration of two approaches of reproducing cementation in a soil sample in DEM.

Another approach to model cemented soils in DEM is to represent the cement agents using cohesive particles, as illustrated in Figure 2.2. This approach was adopted, for example, by Wang & Leung (2008a,b) to simulate artificially cemented soils in the 2D conditions. The idea of generating cement agents inside the host sample proposed by Wang & Leung (2008a,b) is illustrated in Figure 2.3. Inspired by the above work, Wu *et al.* (2023) extended this approach into the 3D case and applied it to model bio-cemented sands. The modelled bio-cemented sample was subjected to uniaxial compression in DEM, and the failure patterns were analysed from the point of view of deviatoric strain, particle rotation and displacement. Besides having a random distribution of cohesive particles in the host sample, as described in the aforementioned cases, the cementing particles can be placed at pre-defined locations. For instance, Evans *et al.* (2014) explicitly modelled the carbonate particles of bio-cemented sand in DEM, hypothesising that the carbonate particles were located around sand-sand contacts. In their study, the bonding strength was assigned following a Weibull distribution to mimic the inhomogeneous bond strength in the cement phase in bio-cemented soils. Evans *et al.* (2014) reported that using such an approach, the ductile behaviour of bio-cemented sand under tensile loading can be captured.

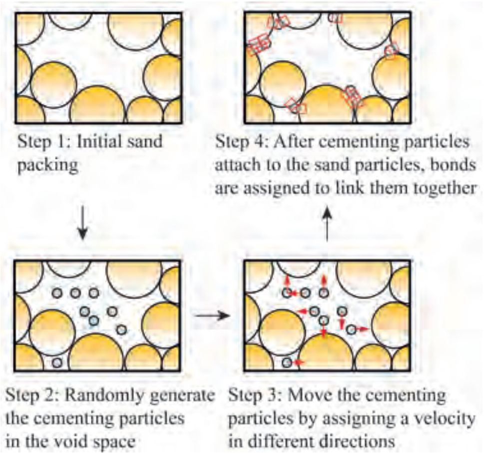

Figure 2.3: Illustration of a procedure for positioning the cementing particles in DEM, reprinted from Wang & Leung (2008b). The grey particles represent the cementing particles, and the yellow particles represent sand grains.

Comparing the two approaches demonstrated in Figure 2.2, approach 1 appears to be easier in the process of sample preparation, as cohesive bonds are directly deployed at sand grain contacts. By contrast, approach 2 requires more effort to prepare the sample since an additional step of placing cementation particles is required. In addition, there are fewer model parameters to be calibrated to match the DEM simulation results to experiment data using approach 1. Moreover, approach 2 consumes much more computational resources than approach 1 as more particles are introduced in approach 2, in general. However, approach 1 suffers from limitations in capturing the mechanical behaviour of (bio-)cemented soils. For instance, the cohesive bonds directly deployed between sand grains will disappear upon failure, which cannot capture the post-breakage behaviour of cementation. In fact, the broken cementation particles still remain in the pore space or attach to sand grains and may play a role in the post-peak mechanical response. In addition, directly deploying cohesive bonds between sand grains assumes the cementation is precipitated at sand-sand contacts, while this is only one of the patterns of cementation distribution as presented in Figure 2.1. In this sense, approach 2 is favoured as it offers the possibility to represent different microstructures of bio-cemented soils.

## 2.4. DEM MODELLING OF DIFFERENT MICROSTRUCTURES

In this thesis, the second approach (Figure 2.2) is adopted to model bio-cemented samples with different microstructures. For this purpose, a toolbox called Cementor is developed. Cementor aims at introducing fines (i.e. calcium carbonate particles in the case of bio-cemented sands) at specific positions within an assembly made up of spherical grains. The toolkit enables the modelling of various types of microstructures, including bridging, contact cementing, coating and their combinations. Cementor is compatible with the open-source platform for discrete element modelling YADE (Yet another dynamic engine) Šmilauer *et al.* (2021). The overall structure of Cementor and the algorithms used for modelling the different distribution patterns are described below. It should be noted that pore filling type is not introduced in the presented toolbox, as it can be modelled straightforwardly in YADE.

### 2.4.1. OVERALL STRUCTURE

The flowchart to generate cemented samples with a single distribution pattern is presented in Figure 2.4. The procedure starts with importing a host sample (the generation of the host sample is not covered in this chapter but can be found in YADE Examples). Thereafter, all particles need to be fixed by blocking all their degrees of freedom, which ensures that the initial fabric of the host material is preserved during the process of introducing fines. The fines generation process, indicated inside the dashed rectangle zone in Figure 2.4, starts after that. It contains four steps:

1. **Enter input parameters**. Different input parameters are used to generate the target microstructure, as summarised in Table 2.1. The definition of each parameter can be found in Section 2.4.2. The input parameters control the number and size of fines to be generated and, therefore, the fine content of the sample. The fine content can be defined by either mass or volume. In this chapter, the fine content is the ratio of the mass of fines to the mass of the host material. The meaning of each parameter is given in the following subsections. Besides the input parameters listed in Table 2.1, other parameters, such as those related to the material properties (density, Young's modulus, etc.) and contact properties (friction angle, cohesive strength, etc.), need to be introduced. These are not discussed in this chapter as they depend on the specific material and contact law used in the DEM simulation. A detailed introduction to the adopted contact law and associated parameters can be found in Chapter 3.

Table 2.1: Input parameters for controlling the number and size of fines.

| Microstructure type | Input parameters |
|---|---|
| Bridging | $TR_{\text{min}}$, $TR_{\text{max}}$ |
| Contact cementing | $T_{CC}$, $N_{CC}$ |
| Coating | $T_{CO}$, $N_{CO}$, $\alpha$ |

2. **Generate raw fines with a defined distribution pattern**. At this stage, the radius and coordinates of the fines are computed using the algorithms described in the following subsections.

3. **Update interactions**. The newly generated fines have not been assigned with interactions. Therefore, we run one "blank"step to detect contact detection and build interactions.

4. **Remove the undesired fines from the raw fines**. Part of the raw fines generated in step 2 may be problematic. For instance, they can unreasonably penetrate into other particles. These fines are undesired, and they are removed at this stage. Note that the criterion for removing undesired fines varies depending on the target microstructure. According to the definition of each type of microstructure, a fine particle in the pattern of bridging has two sand-fine contacts, a fine particle in the pattern of contact cementing has two sand-fine contacts and two fine-fine contacts, and a fine particle in the coating pattern has one sand-fine contact. Therefore, the fines whose number of interactions is not equal to 2 in the case of bridging, 4 in the case of contact cementing, and 1 in the case of coating will be removed.

After the above-described steps, the fixed particles are set free by unblocking all their degrees of freedom. Finally, the cemented sample can be saved. The algorithms used to generate raw fines, as mentioned in step 2, are described in the following subsections.

### 2.4.2. SINGLE DISTRIBUTION PATTERN

#### BRIDGING

Bridging refers to the distribution of fines which fill in the gaps between sand grains. The gap size distribution is a known feature for a given host sand sample. Therefore, we reproduce the bridging type of microstructure by defining the target minimum and maximum radii of fines, namely $TR_{\text{min}}$ and $TR_{\text{max}}$. In Cementor, we loop through all pairs of sand particles to get the coordinates of the centres of both sand particles, $C_{s1}$ and $C_{s2}$, and their radii $r_{s1}$ and $r_{s2}$. The gap distance $d$ of this pair of sand particles is calculated as:

$$d = \|\overrightarrow{C_{s1}C_{s2}}\| - r_{s1} - r_{s2} \tag{2.1}$$

as depicted in Figure 2.5. For gaps that satisfy $TR_{\text{min}} \leq d \leq TR_{\text{max}}$, a fine particle of radius $r = d/2$ is inserted. It should be noted that $r$ is a theoretical value while the computation is done with a finite precision. Therefore, it is suggested to slightly round up $r$ to facilitate contact detection in DEM. The centre $C_f$ of the fine particle to be introduced is given by

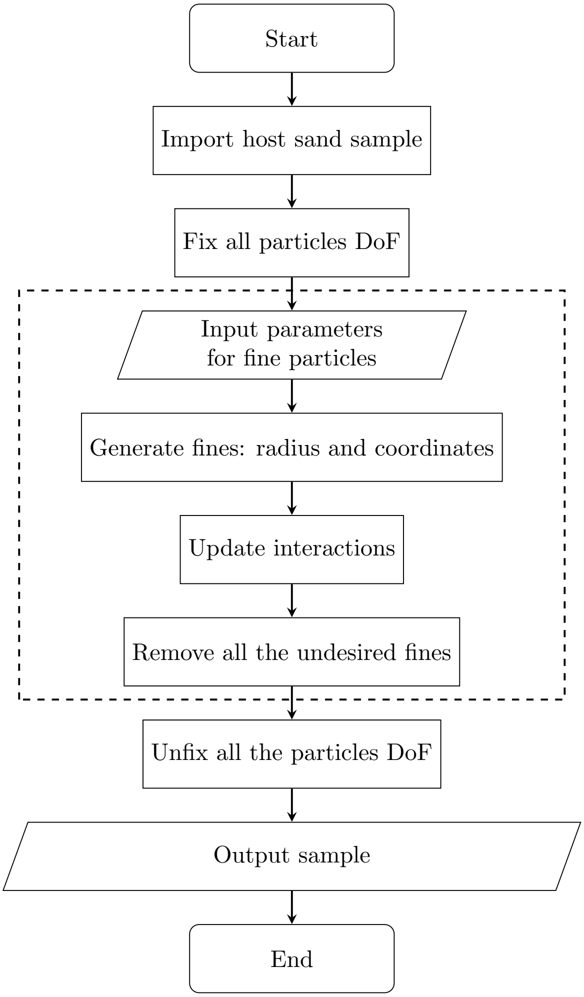

Figure 2.4: Flowchart for generating samples containing fines (i.e. $CaCO_3$) with different microstructures. DoF stands for degree of freedom.

its position vector:

$$\overrightarrow{OC_f} = \overrightarrow{OC_{s1}} + \overrightarrow{C_{s1}C_f} = \overrightarrow{OC_{s1}} + (r_{s1} + r)\,\frac{\overrightarrow{C_{s1}C_{s2}}}{\|\overrightarrow{C_{s1}C_{s2}}\|} \tag{2.2}$$

where $O$ $(0,0,0)$ is the origin of the space.

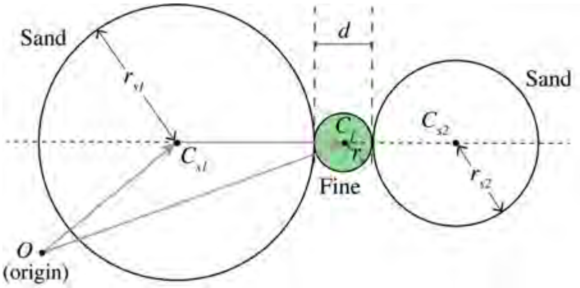

Figure 2.5: Geometry of the bridging pattern.

### CONTACT CEMENTING

Contact cementing refers to a type of microstructure where fines are located around the sand-sand contact points. This type of microstructure was first modelled in 3D DEM by Evans *et al.* (2014). For a given host sand sample, the existing sand-sand contacts can be accessed from YADE. A percentage $T_{CC}$ of all sand-sand contacts is randomly selected in order to be cemented. For each selected sand-sand contact, a set of fines is introduced around the sand-sand contact point and forms a chain (Figure 2.6). All fines of a given chain are in contact with each other and have the same size. The number of fines in each chain $N_{CC}$ is an input parameter. The radius $r$ of the fines can then be determined from the input parameter $N_{CC}$, the radii of the two sand particles in contact, $r_{s1}$ and $r_{s2}$, and the overlap $d$ of these two sand grains. These last quantities can be obtained from YADE.

The fine radius $r$ can be expressed as (Figure 2.6):

$$r = r_c \sin\left(\frac{\pi}{N_{CC}}\right) \tag{2.3}$$

where the chain radius $r_c$ is given by (Figure 2.6):

$$r_c = \sqrt{(r_{s1} + r)^2 - \left(r_{s1} - \frac{d}{2} + h\right)^2} \tag{2.4}$$

with $h$, the distance between the contact point $P$ and the chain centre $C_c$, given by:

$$h = \frac{(r_{s1} - r_{s2})\left(r + \frac{d}{2}\right)}{r_{s1} + r_{s2} - d} \tag{2.5}$$

Note that the contact point $P$ lies along the line connecting $C_{s1}$ and $C_{s2}$ and is the middle point of the overlap.

The coordinates of all $N_{CC}$ fines of a given chain can be determined knowing the position of any of these fines. Therefore, the coordinates of the chain centre $C_c$ should first be obtained. Its position vector is given by:

$$\overrightarrow{OC_c} = \overrightarrow{OP} + h\vec{j} \tag{2.6}$$

where the coordinates of the contact point $P$ are known from YADE, and $\vec{j}$ is a unit vector which direction is from the centre of the sand particle with the largest radius towards the centre of the sand particle with the smallest radius. Accordingly, it is defined as:

$$\vec{j} = \frac{\overrightarrow{C_{s1}C_{s2}}}{\|\overrightarrow{C_{s1}C_{s2}}\|} \tag{2.7}$$

where $C_{s1}$ and $C_{s2}$ are known from YADE.

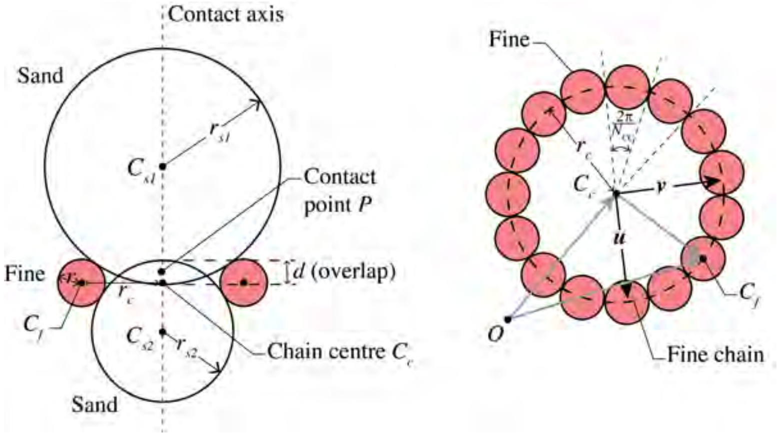

Figure 2.6: Geometry of the contact cementing pattern, demonstrated with 15 fines on a chain.

After $C_c$ is obtained, the coordinates of the fine particles in the chain are calculated as follows (as suggested on `https://math.stackexchange.com/questions/3317798`):

1. We define a non-zero vector $\vec{w}$ orthogonal to $\vec{j} = (a, b, c)$. In 3D, there is an infinite number of vectors perpendicular to $\vec{j}$. We construct one of them, $\vec{w}$, according to the following strategy. We initially set $\vec{w} = (a, b, c)$, and then find the smallest coordinate $a$, $b$ or $c$ in absolute value. We set this value to zero, and swap the other two coordinates and negate the first one. For example, if $|a| \leq |b|$ and $|a| \leq |c|$, we set $a$ to 0, swap $b$ and $c$ and negate $c$. Consequently, $\vec{w} = (0, -c, b)$. Thereby, $\vec{w}$ is perpendicular to $\vec{j}$ at any time, since $\vec{j} \cdot \vec{w} = a0 - bc + cb = 0$.

2. We convert $\vec{w}$ into a vector $\vec{u}$ of magnitude $r_c$:

$$\vec{u} = r_c \frac{\vec{w}}{\|w\|} \tag{2.8}$$

3. We construct a vector $\vec{v}$ perpendicular to $\vec{j}$ and $\vec{u}$ such that:

$$\vec{v} = \vec{j} \times \vec{u} \tag{2.9}$$

4. We determine the coordinates of the centre $C_f$ of one of the fines as:

$$\overrightarrow{OC_f} = \overrightarrow{OC_c} + \overrightarrow{C_c C_f} = \overrightarrow{OC_c} + \vec{u}\cos(\alpha) + \vec{v}\sin(\alpha) \tag{2.10}$$

   where $\alpha$ is an arbitrary angle.

5. We compute all $N_{CC}$ coordinates of the fines centres on the chain as:

$$\overrightarrow{OC_f^k} = \overrightarrow{OC_c} + \vec{u}\cos\left(\frac{2\pi k}{N_{CC}}\right) + \vec{v}\sin\left(\frac{2\pi k}{N_{CC}}\right). \tag{2.11}$$

   where $k = 0, 1, 2, ..., N_{CC} - 1$.

The above algorithm is applied on all the selected sand-sand contacts so that all raw fines with contact cementing type of microstructure are obtained.

### COATING

Coating refers to a microstructure where fines attach to one sand grain only. There are three input parameters controlling the number and size of coating fines: the proportion $T_{CO}$ of sand particles to be coated, the target number $N_{CO}$ of fines coating each selected sand grain, and the ratio $\alpha$ of the radius of the coated sand particle to the radius of the fine particle. Accordingly, in the case of coating, the fine size is linked to the coated sand grain such that $r = \alpha r_s$. The sand particles to be coated are randomly selected from all the sand grains. For each of the selected sand grains, the fines are randomly distributed on the surface of that sand grain, as demonstrated in Figure 2.7. The coordinates of the centre of each fine is given by:

$$\overrightarrow{OC_f} = \overrightarrow{OC_s} + (r_s + r)\,\vec{n} \tag{2.12}$$

where $\vec{n}$ is a random unit vector in the 3D space. Note that since the fines are randomly generated, it is possible that the generated fines overlap with each other, which may cause large repulsive force and an unstable situation. These fines can be detected since their number of interactions is larger than one, and they will be removed as described in Figure 2.4.

## 2.4.3. MIXED-TYPE MICROSTRUCTURE

Cementor is able to generate samples with mixed distribution patterns, namely, a sample exhibiting more than one microstructure pattern. The functions for generating the involved microstructures can be activated by assigning input parameters as listed in Table 2.1 to the corresponding functions. The process is the same as described in Figure 2.4. Specifically, fines with each type of microstructure are generated separately. After that, all the generated fines are assessed to identify the undesired fines. The criterion for determining the undesired fines is the same as described before. Finally, all the undesired fines are removed, and the sample with fines is output.

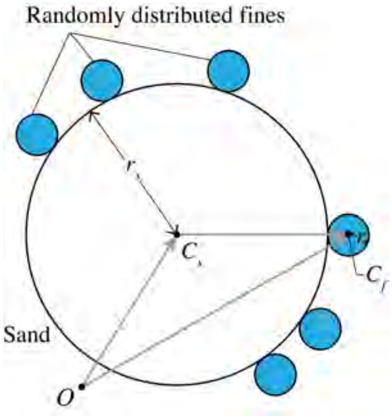

Figure 2.7: Geometry of the coating pattern.

## 2.5. ILLUSTRATIVE EXAMPLES

Examples of DEM samples with different types of microstructures are presented in this section. In the first phase, 3500 host grains are generated inside a cubic domain (0.17 × 0.17 × 0.17 $m^3$) formed by six rigid walls. The particle size distribution of the host grains follows a uniform distribution with a mean grain diameter $d_{50}$ of 2.49 mm. The initial sample is consolidated to a confining pressure of 100 kPa and saved as the host sample. In the second phase, Cementor is used to introduce fine particles within the host sample and form target microstructures. Figure 2.8 shows cemented samples with bridging, contact cementing and coating microstructures, as well as a sample with a combination of these distribution patterns. All the fine-containing samples have a fine content of about 2% by mass. For the sample with a mixed microstructure, the relative proportion of fines in bridging, contact cementing and coating pattern is 1:1:2. The input parameters for generating these samples are given in Table 2.2. Note that for the samples with a single fine distribution pattern, only the parameters associated with the microstructure under consideration are assigned. Other parameters are set equal to 0 by default. In the toolbox, the physical properties of the sample are also provided as preliminary information, including the number of fines, the mass content of fines and the proportion of fines in each distribution pattern. In addition, the coordination number with respect to the solid phase, namely, sand ($Z^s$) and fine ($Z^f$), are given as outputs of Cementor. They are defined as:

$$Z^{\Phi} = \frac{\sum_{i=1}^{N^{\Phi}} C_i}{N^{\Phi}} \tag{2.13}$$

where Φ represents either the sand (s) or fine (f) phase, $C_i$ denotes the number of contacts that particle $i$ (in phase Φ) has, and $N^{\Phi}$ is the number of particles in phase Φ of the assembly. The information of the example samples is presented in Table 2.2.

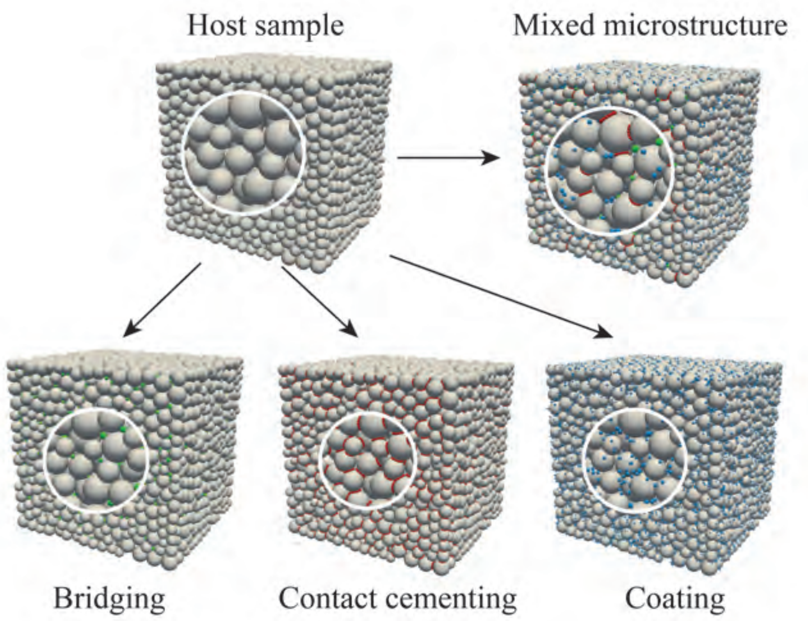

Figure 2.8: Illustration of DEM samples with different microstructures (carbonate content of 2%).

Table 2.2: Characteristics of the example samples (carbonate content of 2%).

| Microstructure type | Input parameters | Output | | |
|---|---|---|---|---|
| | | Number of fines | $Z^s$ | $Z^f$ |
| Grain bridging | $TR_{\text{min}} = 0.0003$ m,<br>$TR_{\text{max}} = 0.000863$ m | 4816 | 7.57 | 2 |
| Contact cementing | $T_{CC} = 75$, $N_{CC} = 15$ | 89340 | 55.87 | 4 |
| Coating | $T_{CO} = 96$, $N_{CO} = 50$, $\alpha = 6.67$ | 22878 | 11.36 | 1 |
| Mixed type | $TR_{\text{min}} = 0.0003$ m,<br>$TR_{\text{max}} = 0.00075$ m,<br>$T_{CC} = 70$, $N_{CC} = 15$,<br>$T_{CO} = 45$, $N_{CO} = 50$, $\alpha = 6.67$ | 33994 | 21.02 | 2.9 |

## 2.6. CONCLUSIONS

Bio-cemented soils exhibit different microstructures depending on the pore-scale distribution of the precipitated calcium carbonate crystals with respect to the host granular skeleton. Four typical carbonate distribution patterns can be identified from microscopic observations, namely grain bridging, contact cementing, coating and pore filling. Being able to model explicitly the different microstructures is an important step towards a better understanding of the material behaviour.

In this chapter, the complex microstructures of bio-cemented soils are characterised and simplified to focus on the main features of the carbonate distribution patterns. Cementor, a toolbox designed to introduce carbonates in various target microstructures within a granular packing, is developed. Cementor can be straightforwardly used with the DEM platform YADE. The developed toolbox can be used to model bio-cemented soils with a single carbonate distribution pattern and mixed carbonate distribution patterns, as well as different carbonate contents.

# 3

# EFFECTS OF CARBONATE DISTRIBUTION PATTERN ON THE MECHANICAL BEHAVIOUR OF BIO-CEMENTED SANDS

---

Parts of this chapter have been published in Zhang & Dieudonné (2023b).

## 3.1. INTRODUCTION

Soils treated with bio-mediated methods, such as microbially induced carbonate precipitation (MICP) and enzyme induced carbonate precipitation (EICP), generally show an improvement in strength, stiffness and dilatancy (Feng & Montoya, 2015; Han *et al.*, 2016; Lin *et al.*, 2016; Terzis *et al.*, 2016; Ahenkorah *et al.*, 2020; Konstantinou *et al.*, 2021; Xiao *et al.*, 2021b; Xu *et al.*, 2021; Nafisi *et al.*, 2021; Zeng *et al.*, 2021). A critical challenge for the implementation of bio-mediated methods in engineering projects is the uncertainty of the improvement in mechanical properties. Indeed, the mechanical improvement can vary over a wide range, even for the same calcium carbonate content (see Figure 1.3). Experimental evidence suggests that the precipitated carbonate can display different distribution patterns. Crystals can form at grain–grain contacts (contact cementing), connect soil grains that are initially not in contact with each other (bridging), precipitate on the grain surface (coating), or fill in the void space (pore filling). More details on the microscopic observations of carbonate distribution patterns are presented in Chapter 2. The various carbonate distribution patterns can account for the variability of the mechanical improvement of bio-cementation.

In this chapter, the discrete element method is used to investigate the role of the carbonate distribution pattern on the mechanical performance of bio-cemented sands. Four types of bio-cemented samples are modelled such that each sample contains only one carbonate distribution pattern. The DEM samples are then subjected to drained triaxial compression at different confining pressures. The effect of carbonate distribution pattern, confining pressure and carbonate content on the mechanical performance of bio-cemented sands is investigated. The role of the microstructure and bond breakage evolution on the macroscopic response is thoroughly analysed.

## 3.2. DISCRETE ELEMENT MODEL

### 3.2.1. INTER-PARTICLE CONTACT LAWS

The discrete element simulations are performed using the open-source platform YADE (Šmilauer *et al.*, 2021). A cohesive-frictional contact model, based on the classical linear elastic-plastic law from Cundall & Strack (1979) and accounting for rolling and twisting resistance, is used. Details of this contact model can be found in Bourrier *et al.* (2013) and Šmilauer *et al.* (2021).

For two spheres of radii $R_1$ and $R_2$ in contact, the normal force $\vec{F}_n$, incremental shear force $\Delta\vec{F}_s$, incremental rolling moment $\Delta\vec{M}_r$ and incremental twisting moment $\Delta\vec{M}_{tw}$ are calculated as:

$$\vec{F}_n = k_n u_n \vec{n} \tag{3.1}$$

$$\Delta\vec{F}_s = -k_s \Delta\vec{u}_s \tag{3.2}$$

$$\Delta\vec{M}_r = -k_r \Delta\vec{\theta}_r \tag{3.3}$$

$$\Delta\vec{M}_{tw} = -k_{tw} \Delta\vec{\theta}_{tw} \tag{3.4}$$

where $u_n$ is the relative normal displacement of the two spheres, $\vec{n}$ is the normal contact vector, $\Delta\vec{u}_s$ is the incremental tangential displacement, and $\Delta\vec{\theta}_r$ and $\Delta\vec{\theta}_{tw}$ are the relative rotations due to rolling and twisting respectively. $k_n$, $k_s$, $k_r$ and $k_{tw}$ are the contact normal stiffness, tangential stiffness, rolling stiffness and twisting stiffness, respectively. They are given by:

$$k_n = \frac{2E_1R_1E_2R_2}{E_1R_1+E_2R_2} \tag{3.5}$$

$$k_s = \nu k_n \tag{3.6}$$

$$k_r = \alpha_r R_1 R_2 k_s \tag{3.7}$$

$$k_{tw} = \alpha_{tw} R_1 R_2 k_s \tag{3.8}$$

where $E_i$ $(i = 1,2)$ is the modulus of elasticity of sphere $i$, $\nu$ is the shearing stiffness coefficient, and $\alpha_r$ and $\alpha_{tw}$ are the rolling and twisting stiffness coefficients respectively.

The normal, shear, rolling and twisting resistances are equal to:

$$F_n^{\max} = \sigma_{coh}\min(R_1,R_2)^2 \tag{3.9}$$

$$F_s^{\max} = \|\vec{F}_n\|\tan\varphi_c' + \sigma_{coh}\min(R_1,R_2)^2 \tag{3.10}$$

$$M_r^{\max} = \|\vec{F}_n\|\eta_r\min(R_1,R_2) \tag{3.11}$$

$$M_{tw}^{\max} = \|\vec{F}_n\|\eta_{tw}\min(R_1,R_2) \tag{3.12}$$

where $\sigma_{coh}$ is a cohesive strength parameter which controls the adhesion forces in the normal and tangential directions. $\varphi_c'$ is the contact friction angle, and $\eta_r$ and $\eta_{tw}$ are the resistance coefficients of rolling and twisting, respectively. In general, an increase in the contact friction angle $\varphi_c'$ leads to an increase in peak strength and dilatancy, but has limited influence on ultimate strength. On the other hand, an increase in the resistance coefficients $\eta_r$ and $\eta_{tw}$ results in an increase in both peak and ultimate strengths, as well as in dilatancy. Further discussion on the effects of the contact model parameters on the macroscopic response of granular assemblies is available in Aboul Hosn *et al.* (2017).

### 3.2.2. SAMPLE PREPARATION AND MODEL PARAMETERS

Bio-cemented samples with different carbonate distribution patterns are generated from the same host sand (i.e. the uncemented sand). The procedure for preparing DEM samples of host sand and bio-cemented soil is as follows:

1. The size of the representative element volume (REV) is determined for the host sample. Indeed, the number of sand particles should be large enough so that the assembly can be considered to be statistically representative. In the meantime, it should be small enough to ensure computational efficiency (Drugan & Willis, 1996; O'Sullivan, 2011; Guo & Zhao, 2016). To identify the size of the REV, five sand assemblies with the same particle size distribution but different numbers of grains, namely 1000, 2000, 3500, 5000 and 7000, are generated. For each sample size, five realisations are generated by varying the random seed. All assemblies (i.e. 25 in total) are consolidated to the same initial porosity of 0.439 and the same initial isotropic pressure of 100 kPa. Then, each sample is subjected to a drained triaxial compression test under 100 kPa of confinement. Figure 3.1 compares the stress-strain responses of assemblies with different numbers of particles. A scattered response is observed among specimens with 1000 grains. As the number

of grains increases, the variation in the stress-strain responses between the different realisations decreases. Moreover, as shown in Figure 3.1(f), the average stress-strain curves tend to converge once the number of grains reaches 3500. This indicates that a number of particles larger than 3500 can be used to produce a stable and reliable response. With the consideration of computational costs and the ability of the host sample to accept different amounts of carbonate particles, a number of 7000 grains is selected for the host sand sample.

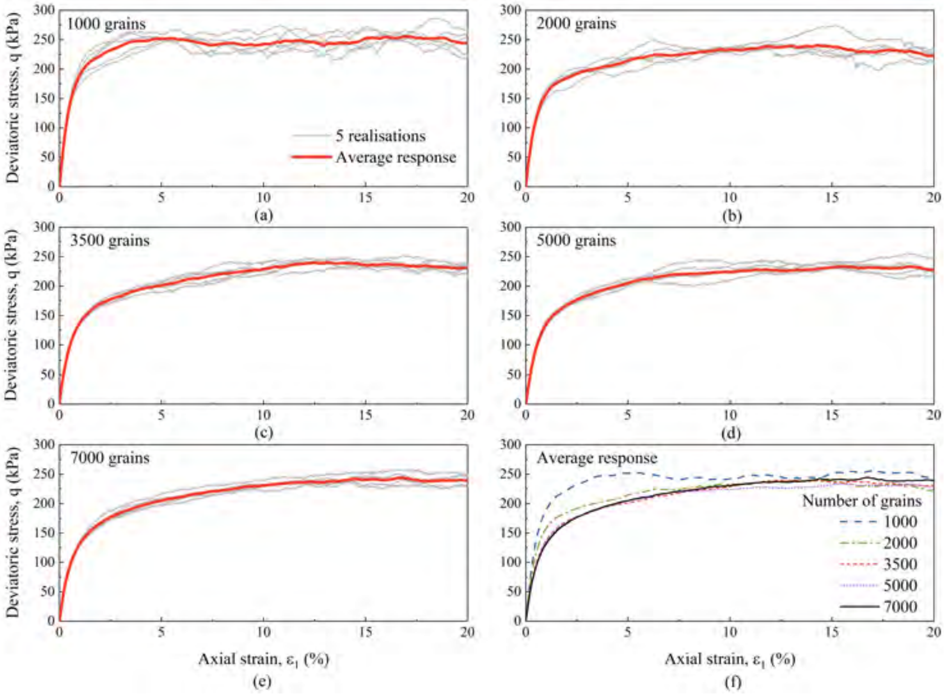

Figure 3.1: Stress-strain responses of assemblies with different grain numbers.

2. A sand packing containing 7000 sand particles is generated. The original particle size distribution can be found in Figure 3.2. The particles are randomly located inside a 7 cm × 7 cm × 14 cm box formed by six rigid walls. There is no contact between the particles at this stage.

3. The radius expansion method incorporated in YADE is used for isotropic compression. Accordingly, the radius of the sand particles is increased proportionally to their initial size until reaching a confining pressure of 100 kPa. The radius expansion is then turned off to fix the size of the particles, and the inter-particle friction angle is adjusted to reach a target porosity of 0.439. During this process, the rigid walls are controlled by a servomechanism to maintain the confining pressure. Once the target porosity is reached, the friction angle is set to the value which is used for the deviatoric loading stage. For samples tested under higher confining pressures (i.e.

200 kPa and 400 kPa), the confining pressure is further increased by moving the lateral walls. The particle size distribution of the host sand after radius expansion is shown in Figure 3.2.

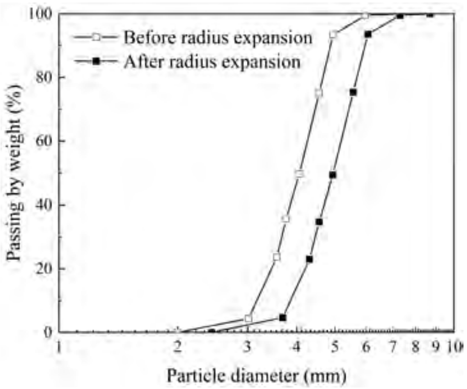

Figure 3.2: Particle size distribution (PSD) of the uncemented (host) sand before and after radius expansion.

4. After the generation of the host sand sample at different confining pressures, Cementor, the algorithm developed in Chapter 2 (Zhang & Dieudonné, 2024), is used to introduce the carbonate particles at the designed positions and obtain the bio-cemented samples with different distribution patterns. Bio-cemented samples with 3 different carbonate contents are investigated in this chapter, namely 1%, 2% and 3% of carbonate mass content $m_c$ (mass of carbonates over the total mass of the sample). Illustrations of the four types of bio-cemented samples are presented in Figure 3.3. The size and number of carbonate particles of bio-cemented samples are summarised in Table 3.1. Figure 3.4 shows uniform distributions of the carbonate content along the height of the sample is achieved.

Table 3.1: Characteristics of bio-cemented samples subjected to the drained triaxial compression under 100 kPa of confinement.

| Property | $CaCO_3$ radii (mm) | $CaCO_3$ number | Initial porosity |
|---|---|---|---|
| Bridging | 0.3 – 0.86 | 7338 – 9665 | 0.434/ 0.429/ 0.422 |
| Contact cementing | 0.12 – 0.37 | 79830 – 191657 | 0.434/ 0.428/ 0.422 |
| Coating | 0.18 – 0.65 | 22899 – 68625 | 0.434/ 0.428/ 0.422 |
| Pore filling | 0.42 | 11537 – 34484 | 0.434/ 0.428/ 0.423 |
| Note: Initial porosity of samples with 1%/ 2%/ 3% of carbonate. | | | |

The parameters used for the sand and carbonate particles are listed in Table 3.2. The parameters of the sand particles correspond to rough sand grains. The Young's modulus of quartz is around 97 GPa (Peng & Redfern, 2013), while the Young's modulus of calcite is around 88.2 GPa (Ekprasert *et al.*, 2020). Accordingly, the Young's modulus of carbonate is assumed to be 0.9 times the Young's modulus of sand. The shearing stiffness coefficient,

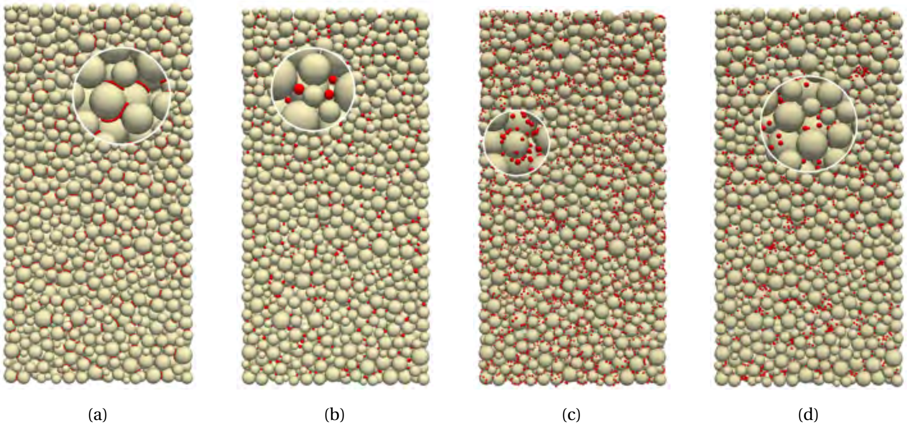

Figure 3.3: DEM samples of idealised bio-cemented sands displaying different distribution patterns: (a) contact cementing, (b) bridging, (c) grain coating, and (d) pore filling.

friction angle, rolling and twisting stiffnesses, and rolling and twisting resistances of carbonate particles are assumed to be the same as those of the sand particles given the lack of experimental data. In this chapter, the aforementioned parameters are maintained constant throughout the simulations, including after bond breakage. However, it should be noted that the experimental study by Ren *et al.* (2021) suggested that the residual strength of cemented grains is slightly greater than the one of uncemented grains due to the formation of debris at the grain surface. Cohesion is only applied on initial sand-carbonate (S-C) and carbonate-carbonate (C-C) contacts and vanishes once a bond is broken. The cohesive strength of sand-sand (S-S) contacts is set equal to 0. The cohesive strength of S-C contacts is set equal to 10 MPa. The cohesive strength of C-C contacts is assumed to be 5 times smaller than that of sand-cement contacts. The determination of $\sigma_{coh}^{S-C}$ and $\sigma_{coh}^{C-C}$ is discussed in detail in Section 3.2.4.

Table 3.2: Properties of the particles used in the DEM simulations.

| Property | Symbol | Unit | Sand (S) | Carbonate (C) |
|---|---|---|---|---|
| Density | $\rho$ | kg/m$^3$ | 2650 | 2710 |
| Young's modulus | E | MPa | 200 | 180 |
| Shearing stiffness coefficient | $\nu$ | - | 0.3 | 0.3 |
| Friction angle | $\varphi'_c$ | ° | 19 | 19 |
| Rolling stiffness coefficient | $\alpha_r$ | - | 0.8 | 0.8 |
| Twisting stiffness coefficient | $\alpha_{tw}$ | - | 0.8 | 0.8 |
| Rolling resistance coefficient | $\eta_r$ | - | 0.15 | 0.15 |
| Twisting resistance coefficient | $\eta_{tw}$ | - | 0.15 | 0.15 |
| Cohesive strength of S-C contacts | $\sigma_{coh}^{S-C}$ | MPa | 10 | |
| Cohesive strength of C-C contacts | $\sigma_{coh}^{C-C}$ | MPa | 2 | |

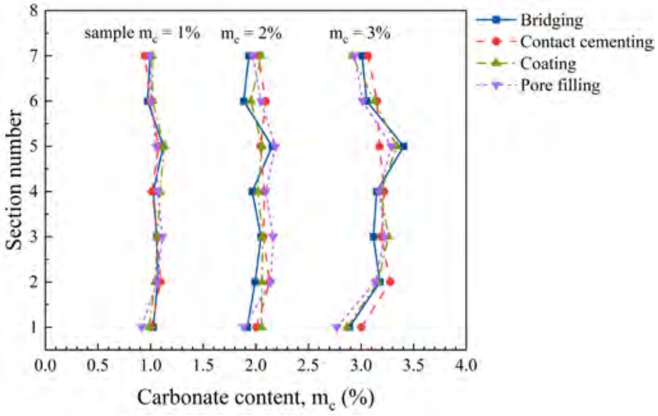

Figure 3.4: Carbonate content distribution along sample height. Data in this figure are from bio-cemented samples with various carbonate contents subjected to the drained triaxial compression test under 100 kPa of confinement.

The uncemented sample and idealised bio-cemented samples are subjected to drained triaxial loading. The deviatoric loading is conducted by a servomechanism which maintains a constant confining pressure on the four lateral walls. All walls are frictionless. The bottom wall is fixed, while a constant strain rate is applied on the top wall. The strain rate is set as 1/s to speed up the simulations. The inertial number $I$ is used to verify quasi-static conditions of the packing (Da Cruz *et al.*, 2005; Rakhimzhanova *et al.*, 2019; Jiang *et al.*, 2019). It is defined as:

$$I = \dot{\varepsilon}\bar{d}\sqrt{\rho/p'} \tag{3.13}$$

where $\dot{\varepsilon}$ is the strain rate, $\bar{d}$ is the mean diameter of particles in the sample, $\rho$ is the particle density and $p'$ is the mean effective stress. The inertial number of uncemented sand is $7.16 \times 10^{-4}$ for $p' = 100$ kPa, which is smaller than the suggested value $1 \times 10^{-3}$ by Da Cruz *et al.* (2005). The inertial number of bio-cemented samples is lower than that of the uncemented sample, as cemented samples have a much smaller mean particle diameter than the uncemented sample. Consequently, quasi-static conditions are ensured for all simulations.

### 3.2.3. RESULTS PROCESSING

In the following, the mean effective stress $p'$ and deviatoric stress $q$ are defined as:

$$p' = \frac{\sigma_1 + \sigma_2 + \sigma_3}{3} \tag{3.14}$$

$$q = \sigma_1 - \frac{\sigma_2 + \sigma_3}{2} \tag{3.15}$$

where $\sigma_1$, $\sigma_2$ and $\sigma_3$ are the three principle effective stresses, which are calculated as the ratio of the (normal) forces on the wall to the surface area of the corresponding wall. Note that all the stresses are positive in compression. $\sigma_1$ is the axial stress, while $\sigma_2$ and $\sigma_3$ are the radial (confining) stresses.

The volumetric strain $\varepsilon_v$ is defined as:

$$\varepsilon_v = \varepsilon_1 + \varepsilon_2 + \varepsilon_3 \tag{3.16}$$

where $\varepsilon_1$, $\varepsilon_2$ and $\varepsilon_3$ are the strains in the three principle directions. They are logarithmic strains defined as:

$$\varepsilon_i = \ln\left(\frac{l_i}{L_i}\right) \tag{3.17}$$

where $l$ and $L$ are the current and initial lengths of the specimen in the concerned direction $i$ = 1, 2 or 3, respectively. Note that the volumetric strain is positive for dilation, and the axial strain in the loading direction ($\varepsilon_1$) is positive for compression.

### 3.2.4. PARAMETRIC STUDY

In this section, parametric studies are carried out to evaluate the effect of $\sigma_{coh}^{S-C}$ and the ratio of $\sigma_{coh}^{C-C}$ to $\sigma_{coh}^{S-C}$ on the mechanical behaviour of DEM bio-cemented samples. To evaluate the effect of $\sigma_{coh}^{S-C}$, samples cemented in the form of grain bridging and contact cementing, and with 1% carbonate content, are subjected to drained triaxial compression under 100 kPa of confinement. To evaluate the effect of the ratio of $\sigma_{coh}^{C-C}$ to $\sigma_{coh}^{S-C}$, only samples with contact cementing are used as $\sigma_{coh}^{C-C}$ is only introduced in that type of cementation. Other parameters are consistent with the ones indicated in Table 3.2.

Figure 3.5 shows the stress-strain curves and volumetric responses of samples with various $\sigma_{coh}^{S-C}$. It can be seen that a value of $\sigma_{coh}^{S-C} = 4$ MPa leads to an obvious improvement in peak stress for the bridging type of sample, while it leads to negligible improvement for the contact cementing type of sample. The peak stress of both bridging and contact cementing type of samples increases with increasing $\sigma_{coh}^{S-C}$. Referring to the experimental results reviewed in Figure 1.4, the peak stress of a lightly bio-cemented sample with $m_c = 0.7\%$ is around 225 kPa from a drained triaxial compression test under 100 kPa of confining pressure. Based on this clue, $\sigma_{coh}^{S-C}$ is set equal to 10 MPa.

A parametric study is carried out to test the mechanical responses of contact cementing type of samples with various ratios of $\sigma_{coh}^{C-C}$ to $\sigma_{coh}^{S-C}$ (while $\sigma_{coh}^{S-C} = 10$ MPa). The results are compared in Figure 3.6. No significant difference can be seen between the results from different ratios of $\sigma_{coh}^{C-C}$ to $\sigma_{coh}^{S-C}$. In addition, it has been observed by Montoya & Feng (2015) that failure tends to occur in the cement phase. Consequently, a ratio ( $\sigma_{coh}^{C-C} / \sigma_{coh}^{S-C}$) of 0.2 is used in this chapter.

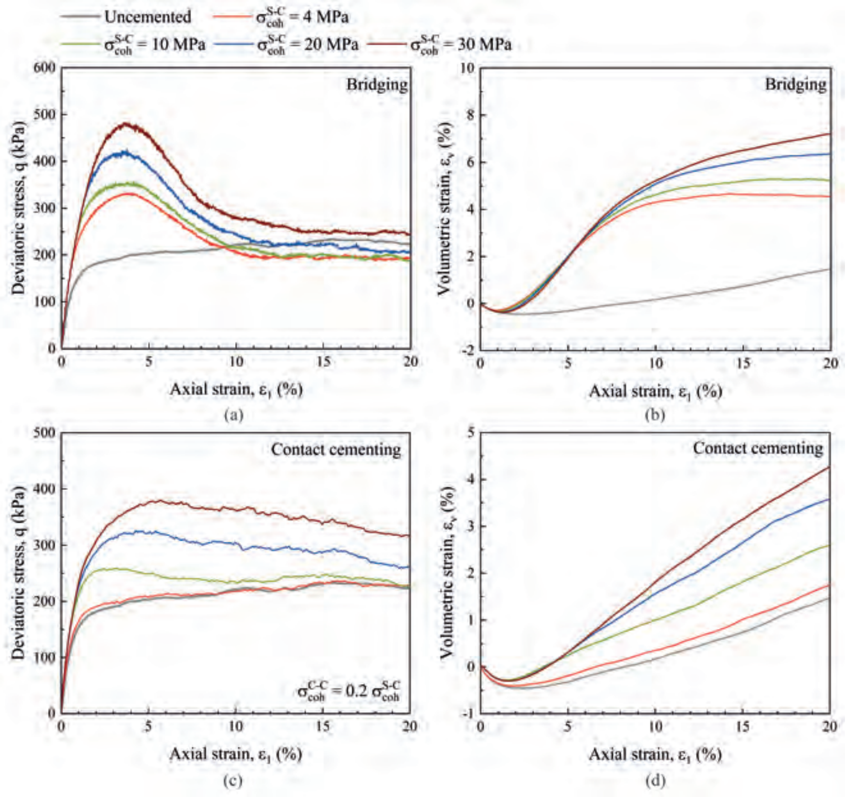

(a) (b) (c) (d)

Figure 3.5: Effect of $\sigma_{coh}^{S-C}$ on the (a) stress-strain response and (b) volumetric response of cemented samples with grain bridging, and (c) stress-strain response and (d) volumetric response of samples with contact cementing. For all tests, the carbonate content is equal to 1% and the confining pressure is 100 kPa.

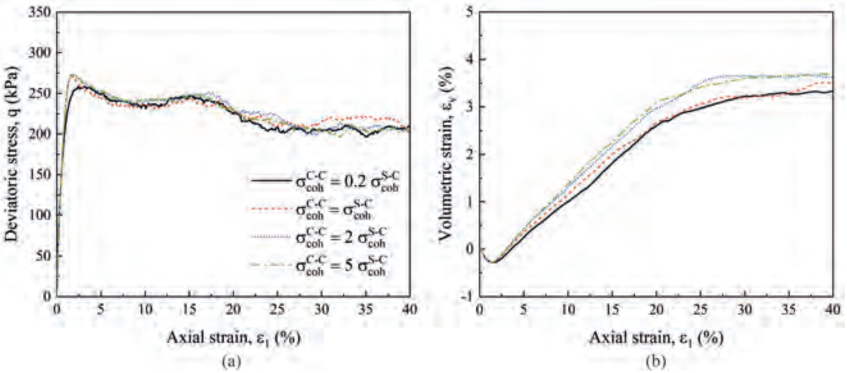

(a) (b)

Figure 3.6: Parametric study on the effect of $\sigma_{coh}^{C-C}$ / $\sigma_{coh}^{S-C}$ on the mechanical response of contact cementing type of samples ($m_C$ = 1%, confining pressure = 100 kPa). (a) Stress-strain response and (b) volumetric response.

## 3.3. RESULTS AND DISCUSSION

### 3.3.1. MACROSCOPIC RESPONSES

#### EFFECTS OF THE CARBONATE DISTRIBUTION PATTERN

The effects of the carbonate distribution pattern on the mechanical response of bio-cemented sands are highlighted in Figure 3.7. It reveals that carbonates distributed in the patterns of bridging and contact cementing significantly affect the stiffness (denoted $E_{50}$ in Figure 3.7a), strength and volumetric response of samples with 1% of carbonate content. Coating type results in a slight improvement of strength and dilatancy, while pore filling has negligible effects on the response of the material. The stress-strain responses, and in particular the yielding pattern, of contact cementing and bridging are fundamentally different. The sample with bridging cementation exhibits a higher peak strength and relatively brittle yielding as compared to contact cemented samples, whose behaviour is associated with strain-softening. This difference in mechanical response can be explained by different initial carbonate distribution patterns and different evolutions of the carbonate distribution upon shearing, which is further discussed based on microscopic observations in Section 3.3.2.

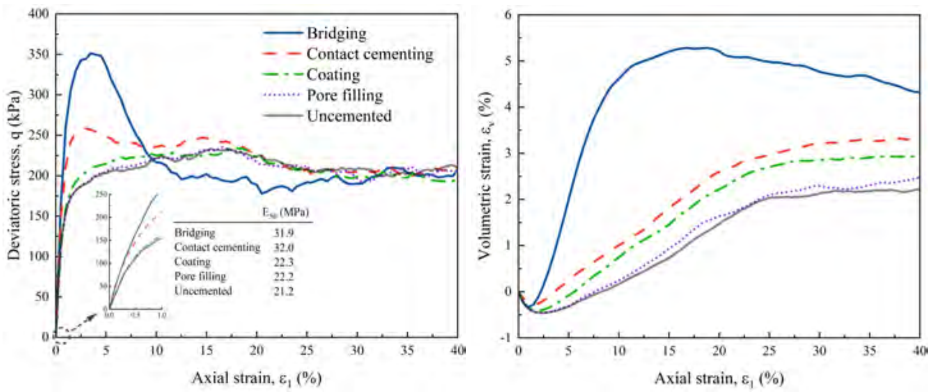

(a) (b)

Figure 3.7: Effects of the carbonate distribution pattern on the shear response of bio-cemented samples with 1% of carbonate content and under a confining pressure of 100 kPa. (a) Stress-strain response and (b) volumetric response.

Figure 3.7b shows that both bridging and contact cementing types exhibit obvious dilatancy enhancement as a result of particle bonding. This enhancement in dilatancy of bio-cemented sands is generally observed in experimental studies (see Wang & Leung, 2008b; Nafisi *et al.*, 2020; Wu *et al.*, 2021, among others). The enhancement can be attributed to the irregular particle clusters formed of sand grains and binders (Shen *et al.*, 2016). These clusters lead to a more open soil structure and larger volumetric strain upon shearing as compared to the uncemented material. In addition, the unbroken clusters prevent the high void space from collapsing, thereby maintaining a high volumetric strain at large strain, as reported by Wang & Leung (2008b). Finally, the bio-cemented sample with a coating pattern shows an increase in dilatancy, which can be attributed to the additional interlocking of particles upon shearing. This can be inferred from the evolution of the coordination number of carbonates, which is discussed in Section 3.3.2.

### EFFECTS OF THE CONFINING PRESSURE

Figure 3.8 shows the results of triaxial simulations on bio-cemented samples with 1% of carbonate content at confining pressures of 200 kPa and 400 kPa, respectively. Qualitatively, the mechanical behaviour of each type of bio-cemented samples under 200 kPa and 400 kPa confinement is similar to the corresponding case at 100 kPa. On the other hand, the improvement in strength for bridging and contact cementing becomes negligible with respect to the effect of the increasing confining pressure. This finding is consistent with experimental observations from Feng & Montoya (2015) and Nafisi *et al.* (2020), in which lightly bio-cemented samples exhibit limited improvement in strength under a confining pressure of 400 kPa.

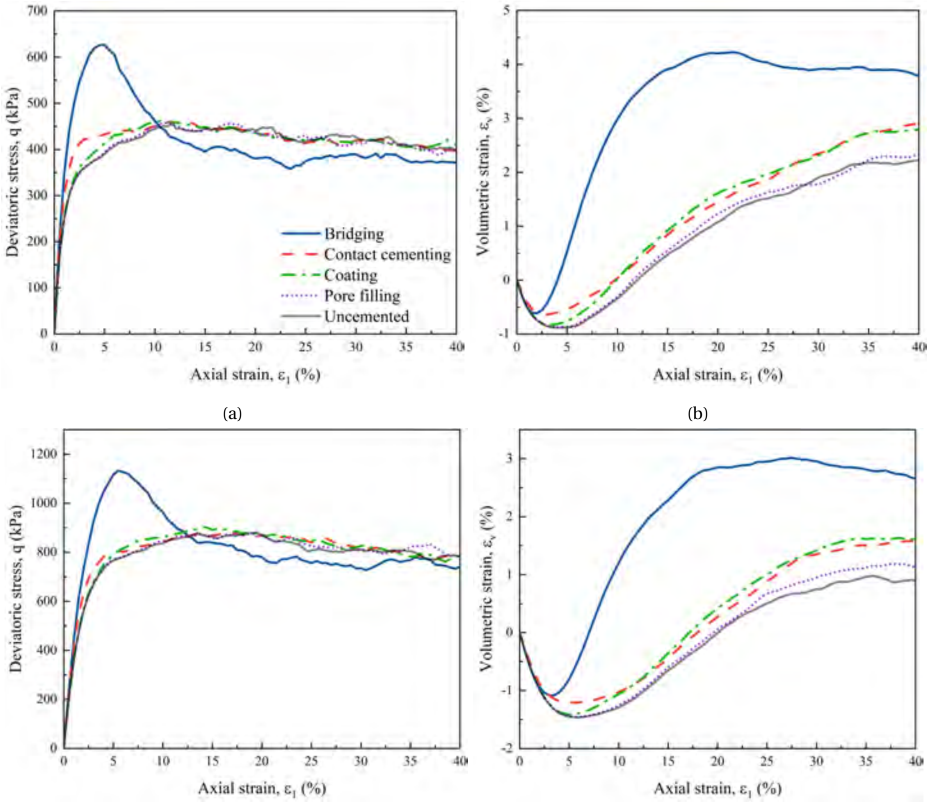

(a)

(b)

(c)

(d)

Figure 3.8: Effects of the confining pressure on the mechanical response of bio-cemented samples with 1% of carbonate content. (a) Stress-strain response and (b) volumetric response upon shearing under a confining pressure of 200 kPa, (c) stress-strain response and (d) volumetric response upon shearing under a confining pressure of 400 kPa.

### EFFECTS OF CARBONATE CONTENT

Cemented samples with carbonate contents up to 3% show similar mechanical behaviour as samples with a carbonate content of 1% in general. Figure 3.9 and Figure 3.10 show the strength envelopes at the peak and ultimate states ($\varepsilon_1 = 40\%$), and their evolution with the carbonate content, in the case of bridging and contact cementing samples. The effective friction angle ($\phi'$) and cohesion ($c'$) at each state are derived using linear Mohr-Coulomb criteria. Figure 3.9 shows that a higher carbonate content leads to a higher peak strength in both bridging and contact cementing cases. Moreover, the increase in peak strength is associated with increases in both friction angle and cohesion in the case of bridging, while the increase in peak strength for contact cementing case mainly arises from an increase in cohesion rather than friction. The friction angle at the ultimate state of both bridging and contact cementing samples remains fairly constant with increasing carbonate content, as shown in Figure 3.10. The relationship between carbonate content and improvement in cohesion is further elaborated in Figure 3.11, from which a linear relationship can be inferred between carbonate content and peak cohesion. This finding is consistent with what has been reported by Wu *et al.* (2021). In addition, the increase in peak cohesion with increasing carbonate contents is higher for contact cementing than for bridging pattern. The cohesion at the ultimate state is low, especially for the contact cementing case. This can be attributed to the large amount of broken bonds at the ultimate state, which is discussed in Section 3.3.2.

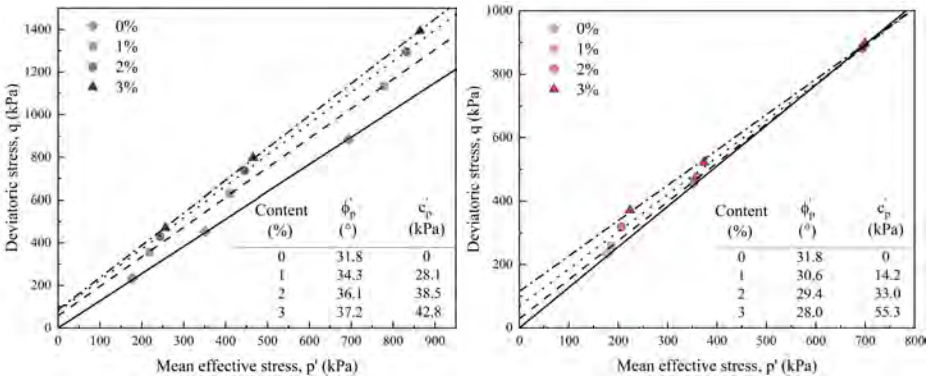

(a) (b)

Figure 3.9: Peak strength envelopes for different carbonate contents: (a) bridging and (b) contact cementing.

It should be noted that, in the case of coating, there is a clear trend of increase in strength with the increasing of carbonate content, as shown in Figure 3.12a. This behaviour is further associated with an improvement in dilatancy. On the other hand, there is a negligible effect of carbonate on the mechanical behaviour of pore filling type of samples, as shown in Figure 3.12b. This could be attributed to the relatively low carbonate content (up to 3%) in the present study. This finding is in agreement with what had been observed from DEM studies on pore-filling type of methane hydrate soils (Brugada *et al.*, 2010; Ding *et al.*, 2022, among others).

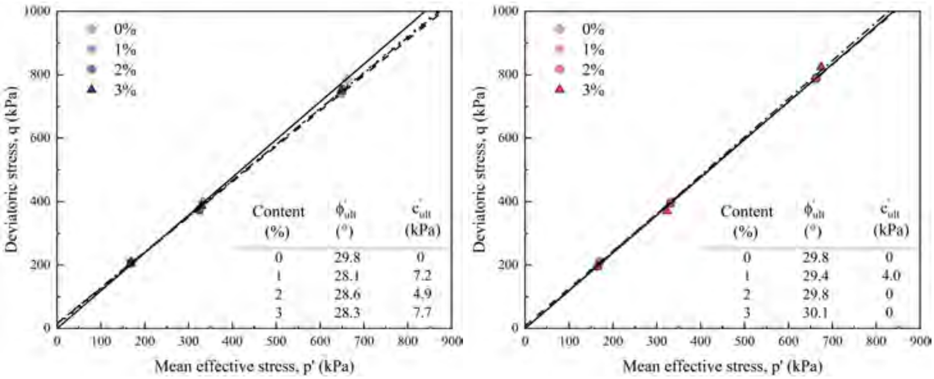

(a)

(b)

Figure 3.10: Ultimate strength envelopes for different carbonate contents: (a) bridging and (b) contact cementing.

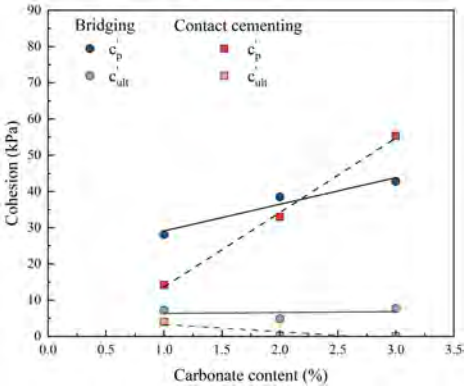

Figure 3.11: Evolution of the cohesion at peak and ultimate states with carbonate content in the case of bridging and contact cementing.

It is worth pointing out that samples with pore filling carbonates can refer to bimodal or gap-graded soils. Gap-graded soils are mixtures of coarse and cohesionless fine grains having a gap or measurable difference between their sizes (Sufian *et al.*, 2021; Otsubo *et al.*, 2022; Yilmaz *et al.*, 2023). Figure 3.13 presents the particle size distribution of a pore filling type of sample ($m_c = 3\%$). We see that the grain sizes of the cemented sample show a gap-graded feature. Consequently, the studies on the mechanical behaviour of gap-graded soils are relevant for cemented samples with pore filling carbonates, especially when the carbonate content is high (above 3%), which is not covered in this chapter. When the carbonate content is below 3%, the carbonate particles hardly affect the mechanical behaviour of the sample, as found in this chapter. With the increase in carbonate content (or the increase in fine content for a gap-graded soil), the mechanical behaviour of the soil evolves from a sand-dominated material to a fine-dominated one. In the sand-dominated stage (low fine content), fines are hardly involved in the contact network. The contribution to overall stress largely arises from the sand-sand contacts, as reported by de Frias Lopez *et al.* (2016) and Otsubo *et al.* (2022). In the fine-dominated stage (high fine content), the fine-fine contacts form the major load-bearing skeleton. Note that a transitional fine content can be identified which is the boundary between the sand-dominated stage and the fine-dominated stage. The transitional fine content of soil varies with the coarse-fine size ratio ($D_{50}^{coarse}/D_{50}^{fine}$). The coarse-fine size ratio of the pore filling sample presented in Figure 3.13 is 5.89. According to the findings by Zuo & Baudet (2015) and Yilmaz *et al.* (2023), the transitional fine content of the sample with coarse-fine size ratio equal to 5.89 may lie in the range of 20% to 50%, which is far beyond the 3% considered here. This suggests that the mechanical behaviour of the cemented samples with pore filling presented in this chapter is sand-dominated. More details from the microscopic investigation are presented in Section 3.3.2, which can further support the dominant role of sand grains in presented pore filling samples.

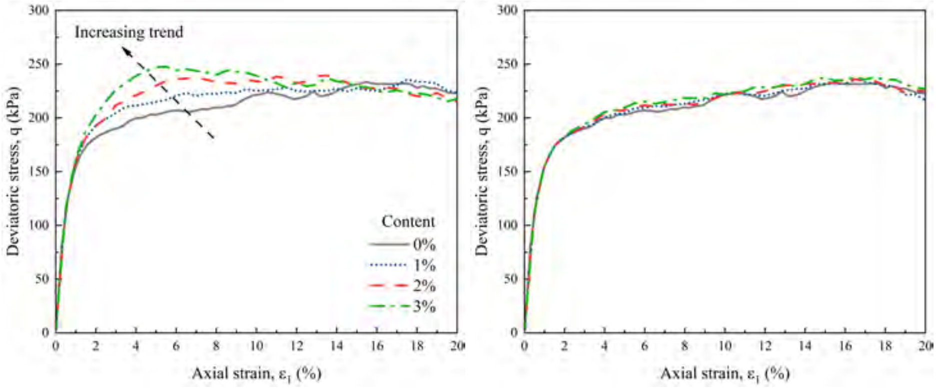

(a) (b)

Figure 3.12: Effects of carbonate content on the stress–strain response under a confining pressure of 100 kPa. Samples with (a) coating and (b) pore filling distribution patterns.

The constitutive behaviour of the DEM samples (both the uncemented sample and the bio-cemented samples) presented in this section are compared with experimental

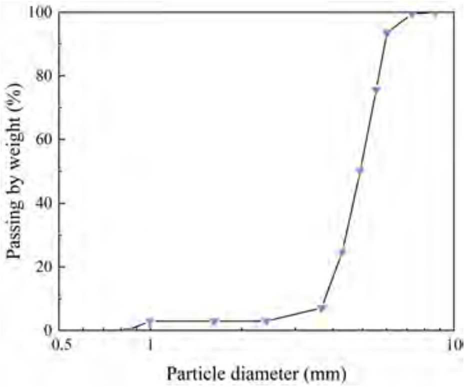

Figure 3.13: Particle size distribution of a pore filling type of sample with 3% of carbonate, showing a gap-graded feature. The coarse-fine size ratio is 5.89.

data (see Figure 1.4) for model validation. It is found that the DEM models qualitatively capture the macroscopic responses observed in experiments. Specifically, the evolution of the stress-strain relationship and the volumetric response of the DEM model for the uncemented sample shows good agreement with the experimental results in general. In addition, the DEM models capture the changes in constitutive behaviour due to the bio-cementation, such as the increase in stiffness, stress and dilatancy, as well as strain hardening and strain softening behaviours, which are also consistent with those observed experimentally.

## 3.3.2. MICROSCOPIC OBSERVATIONS

### COORDINATION NUMBERS

The coordination number $Z$ can be used to describe granular assemblies and, in particular, the average number of contacts per particle. In the case of structured polyphasic soils, the coordination number of the different (solid) phases provides better insights into the effects of the phases on the granular structure than the overall coordination number. The coordination number related to phase $\Phi$ is defined as:

$$Z^{\Phi} = \frac{\sum_{i=1}^{N^{\Phi}} C_i}{N^{\Phi}} \tag{3.18}$$

where $\Phi$ represents either the sand (s) or carbonate (c) phase, leading to the coordination number of sand ($Z^s$) and carbonate ($Z^c$), respectively. $C_i$ denotes the number of contacts that particle $i$ (in phase $\Phi$) has, and $N^{\Phi}$ is the number of particles in phase $\Phi$ of the assembly.

Figure 3.14 presents the evolution of the coordination numbers for sand and carbonate particles during the triaxial compression test under 100 kPa of confinement. Figure 3.14a shows that contact cementing increases drastically $Z^s$. This increase of $Z^s$ is associated with the fact that each carbonate particle initially introduces two S-C contacts. In addition, for the same carbonate content (1%), the contact cementing sample involves the largest number of carbonate particles (78765 for contact cementing, 7338 for bridging, 22893 for coating and 11448 for pore filling). Consequently, this distribution pattern leads to the highest $Z^s$ among all the cemented samples with a given carbonate content. Bridging and coating also exhibit a large increase in $Z^s$ as carbonate particles connect to sand grains, which results in an increase in the number of contacts of sand grains. $Z^s$ of pore filling sample behaves similarly to the uncemented sample. It drops initially and becomes stable at around 3 to 3.5. Note that this trend is generally observed in dense DEM samples (Rothenburg & Kruyt, 2004; Guo & Zhao, 2013). The similarity between $Z^s$ in the cases of pore filling and the uncemented sample can be attributed to the negligible number of contacts introduced by carbonates to the sand grains. This can also be inferred from Figure 3.14b, which shows that $Z^c$ of pore filling remains at a very low value close to 0, indicating that carbonates in the case of pore filling are basically not involved in the particle matrix. $Z^c$ in the case of contact cementing starts at 4, as each carbonate particle connects to two sand grains and its two neighbouring carbonates initially. Similarly, $Z^c$ in the cases of bridging and coating is initially equal to 2 and 1, respectively, as each carbonate particle connects respectively to two or one sand grains. $Z^c$ of contact cementing and bridging gradually decrease during shearing due to the loss of sand-carbonate connections. On the other hand, $Z^c$ in the case of coating shows a moderate increase as some of the carbonates gain new contacts with other particles during shearing.

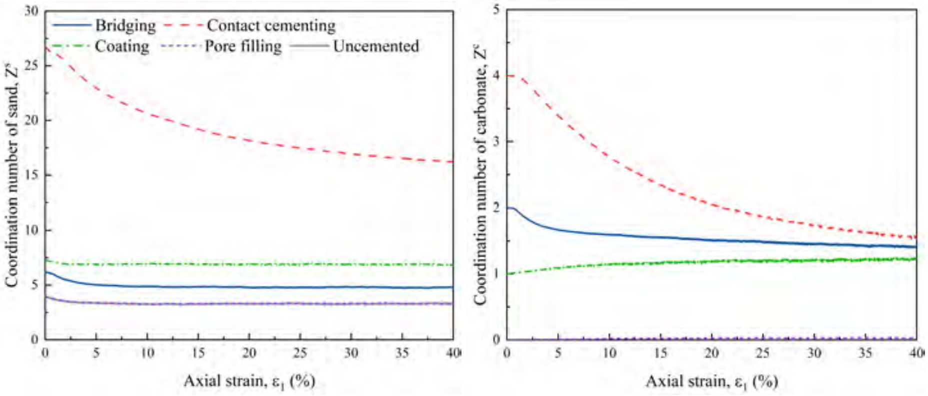

(a) (b)

Figure 3.14: Evolution of coordination numbers of the (a) sand and (b) carbonate phases for samples with 1% of carbonate content subjected to triaxial compression under 100 kPa of confinement.

The mechanical coordination number $Z_m$ can further be used to describe the mechanical contribution of granular assemblies. Following Thornton (2000), the mechanical coordination number of phase Φ is defined in this chapter as:

$$Z_m^{\Phi} = \frac{\sum_{i=1}^{N^{\Phi}} C_i - N_1^{\Phi}}{N^{\Phi} - N_1^{\Phi} - N_0^{\Phi}} \tag{3.19}$$

where $N_0^{\Phi}$ is the number of particles in phase Φ without any contact and $N_1^{\Phi}$ is the number of particles in phase Φ with one contact only.

The mechanical coordination number for sand and carbonate are shown in Figure 3.15. $Z_m^s$ and $Z^s$ exhibit similar trends for all types of samples. In contrast, $Z_m^c$ evolves differently as $Z^c$ in the cases of bridging, coating and pore filling. $Z_m^c$ in the case of bridging almost keeps constant at 2. $Z_m^c$ of coating starts from 0 and evolves around 2. Pore filling begins with 0 and shows a large fluctuation at the beginning and goes above 2.

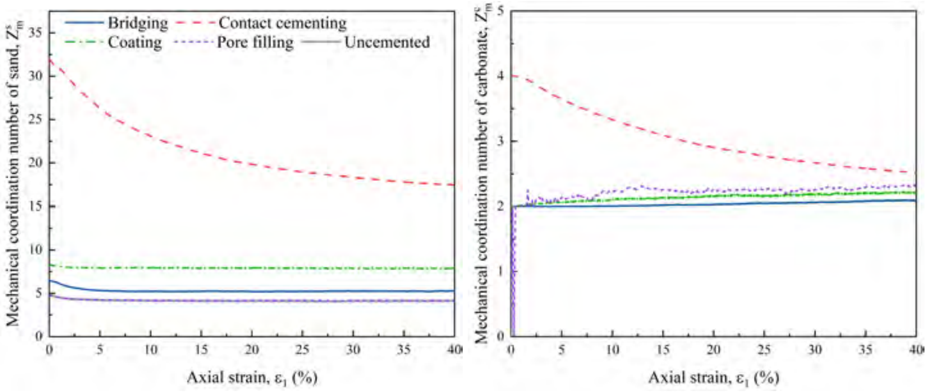

(a) (b)

Figure 3.15: Evolution of mechanical coordination numbers of the (a) sand and (b) carbonate phases for samples with 1% of carbonate content subjected to triaxial compression under 100 kPa of confinement.

As discussed above, interesting insights can be obtained from the coordination number and mechanical coordination number. However, these numbers have a limited capacity to explain the mechanical behaviour of bio-cemented soils upon shearing. In particular,

- The significant high values of $Z^s$ and $Z_m^s$ in the case of contact cementing hardly reflect the difference in mechanical response as compared to uncemented samples or bio-cemented samples displaying a different distribution pattern. Instead, samples with contact cementing show a lower peak strength than bridging samples (Figure 3.7a). This inconsistency results from the fact that $Z$ and $Z_m$ are derived based on the number of contacts of every single particle, while several carbonate particles strengthen together one sand-sand contact in the case of contact cementing (Figure 3.16). Therefore, an alternative approach for the definition of the coordination number for the contact cementing case is to treat this set of carbonates as one equivalent bond.
- Samples with grain coating show the second highest $Z^s$ and $Z_m^s$, while they do not exhibit obvious strength improvement. This suggests that it might be better to take into account only the contacts created by carbonate particles that bond sand grains.

To reveal this feature, a new effective coordination number $Z_e$ is introduced to describe the average number of effective bonds per sand grain. It is defined as:

$$Z_e = \frac{2\,(C_s + C_b)}{N_s} \tag{3.20}$$

where $N_s$ is the number of sand particles, $C_s$ is the total number of S-S contacts and $C_b$ is the number of effective bond in cemented samples. As illustrated in Figure 3.16, in the case of bridging, every carbonate initially connects two sand grains. Therefore, $C_b$ is equal to the number of carbonate particles that have maintained their original two S-C contacts. In the case of contact cementing, several carbonates form a cement chain and, together, strengthen one S-S contact. Therefore, in this case, $C_b$ is equal to the number of intact cement chains. Finally, in the case of coating and pore filling, $C_b$ is equal to zero as carbonate particles do not introduce connections between sand grains.

Figure 3.17 shows the evolution of effective coordination numbers for different types of samples, from which it can be seen that the bridging sample shows the highest $Z_e$ initially, followed by the contact cementing sample. This indicates that new effective bonds are introduced in the case of bridging and contact cementing, leading to the improvement in strength (Figure 3.7). Samples with a distribution pattern of carbonates in the forms of coating and pore filling have almost the same coordination number as the uncemented sample, corresponding to no additional effective bonds introduced from carbonate particles.

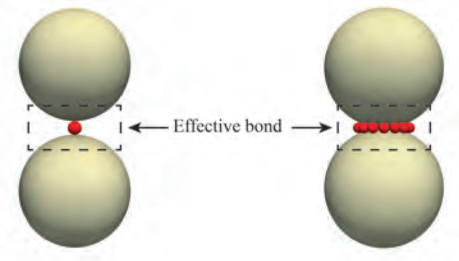

Figure 3.16: Definition of effective bonds in samples with bridging (left) and contact cementing (right) carbonate distribution patterns.

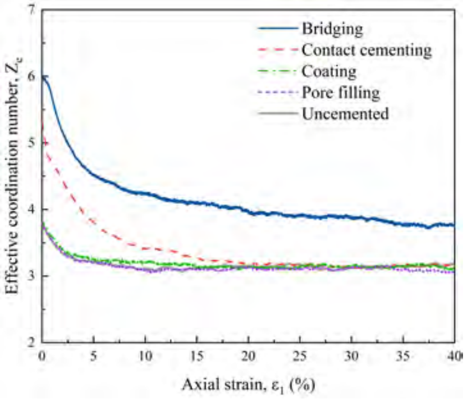

Figure 3.17: Evolution of the effective coordination number upon shearing under a confining pressure of 100 kPa (carbonate content is 1% for bio-cemented samples).

### BOND BREAKAGE BEHAVIOUR

The stress-strain responses of bridging and contact cementing samples are related to the evolution of the microstructure upon shearing and, in particular, the progressive breakage of bonds. The bond breakage ratio is defined as the ratio between the number of broken effective bonds and the number of initial bonds. Figure 3.18 shows the evolution of the bond breakage rate (the derivative of bond breakage ratio with respect to axial strain) normalised by its maximum value in the corresponding simulation. Figure 3.18a shows that, in the case of bridging, the maximum bond breakage rate occurs prior to the peak strength and coincides with the maximum tangent Young's modulus. It is followed by a sharp decrease. In that case, a single carbonate particle contributes to the contact between two sand grains. Accordingly, as soon as one of the initial S-C contacts is lost, the contribution to the strength improvement vanishes, leading to an overall softening. In the case of contact cementing (Figure 3.18b), the post-peak behaviour is associated with a gradual decrease of the normalised bond breakage rate, leading to a progressive decrease in the overall strength and a more ductile behaviour as compared to the case of bridging. Figure 3.19 shows the breakage progress of one cement chain monitored upon shearing. The breakage progress is described as the percentage of the number of carbonates which have lost any of their initial connections to sand grains over the number of carbonates which keep the original connections to sand grains in that cement chain. The figure shows that the connections between sand grains and carbonate particles in the cement chain are not lost at the same time but gradually at different strain levels.

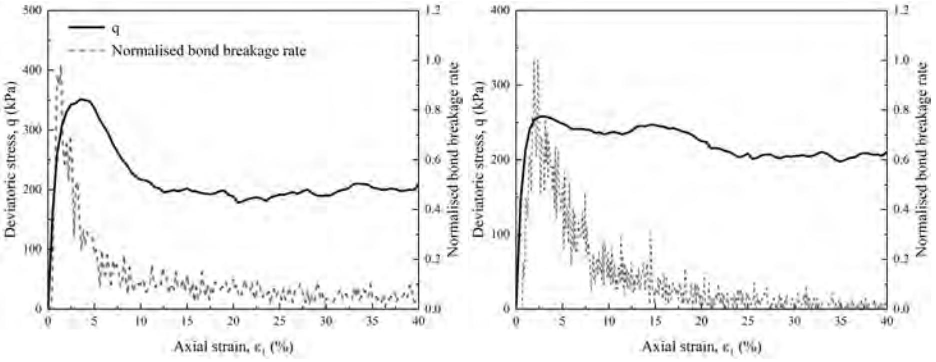

(a) (b)

Figure 3.18: Normalised bond breakage rate of (a) bridging and (b) contact cementing samples with 1% of carbonate content during the shearing under 100 kPa of confinement.

The bond breakage ratio at the ultimate state is plotted in Figure 3.20. The figure shows that, in the cases of both bridging and contact cementing, the ultimate bond breakage ratio increases with the confining pressure. In addition, most bonds are broken at the ultimate state in contact cementing cases, while the samples with a bridging pattern show a much lower bond breakage ratio as compared to contact cementing samples.

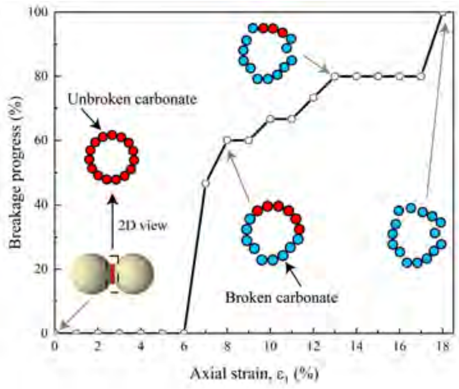

Figure 3.19: Breakage progress of one cement chain. Data extracted from the contact cementing sample with 1% carbonate content, sheared under 100kPa of confinement.

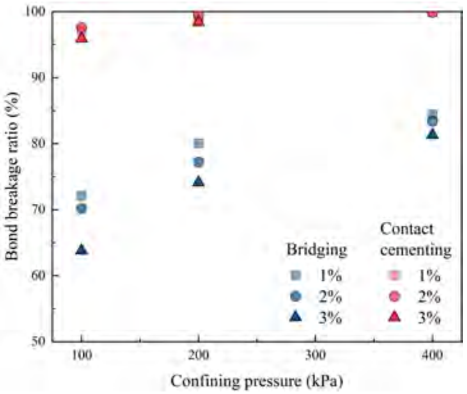

Figure 3.20: Evolution of the bond breakage ratio at $\varepsilon_1$ = 40% with the confining pressure.

### SPATIAL DISTRIBUTION OF BREAKAGE

Figure 3.21 presents the spatial distribution of breakage at an axial strain of 40% in the case of bridging and contact cementing under a confining pressure of 100 kPa. The black dots in Figure 3.21 represent the carbonates which have lost any of their initial S-C contacts. It can be seen that for both bridging and contact cementing, the breakage events distribute uniformly among the sample, independently of the carbonate content. This finding is in agreement with observations on the lightly cemented sample by Li *et al.* (2017). However, strain localisation in the form of shear bands has been observed in bio-cemented sands by Montoya & DeJong (2015); Lin *et al.* (2016); Cui *et al.* (2017); Nafisi *et al.* (2019). The reason why shear localisation is not observed in this chapter may be attributed to the rigid walls used for the boundaries, which hamper the development of shear bands (Yang *et al.*, 2019). Further DEM studies with soft membrane boundaries are necessary to assess the role of boundary conditions on the development of strain localisation.

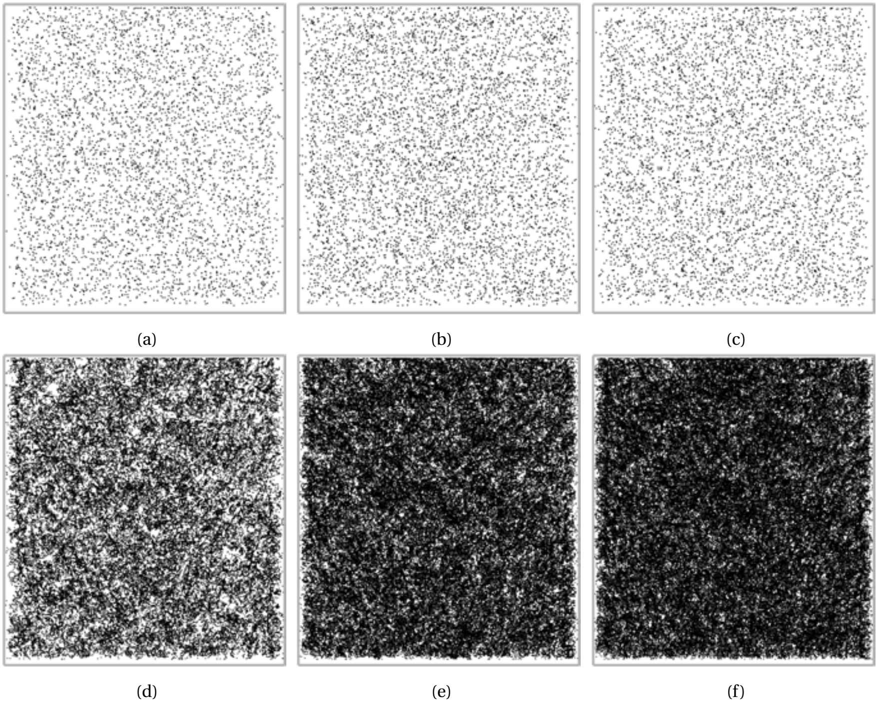

Figure 3.21: Spatial distribution of breakage at an axial strain of 40%. (a) 1%, (b) 2% and (c) 3% carbonate content for bridging type of samples, and (d) 1%, (e) 2% and (f) 3% carbonate content for contact cementing type of samples.

## 3.4. CONCLUSIONS

In this chapter, DEM is used to investigate the role of the carbonate distribution pattern on the mechanical performance of bio-cemented sands. Four types of distribution patterns are investigated, namely bridging, contact cementing, grain coating and pore filling. Idealised bio-cemented samples which contain only one of the four distribution patterns are modelled in DEM. In each of the samples, carbonate particles are explicitly simulated with particles placed in designated positions to replicate the corresponding distribution pattern. The results from a series of drained triaxial compression simulations carried out in this paper show that the distribution patterns of carbonate strongly affect the mechanical behaviour of bio-cemented sands. While bridging and contact cementing lead to the highest improvement in stiffness, strength and dilatancy, coating shows a trend of improvement in strength with increasing carbonate content, associated with an increase in dilatancy. Bio-cemented samples displaying a pore filling pattern show a similar behaviour as the uncemented sample. For the same carbonate content, cementation in the form of bridging leads to the largest strength improvement as well as the largest dilatancy enhancement, followed by the contact cementing pattern. The strength parameters of bio-cemented soil samples are derived assuming a linear Mohr–Coulomb criterion. The formation of carbonate crystals in the bridging pattern contributes to the shear resistance of bio-cemented soil by increasing both the friction angle and cohesion, while it mainly exhibits an increase in cohesion rather than friction angle for samples with a contact cementing pattern. An engineering implication from the findings of the present paper is that to gain strength improvement the most effectively, treatment should ideally be tailored to precipitate calcium carbonate in the bridging pattern. Therefore, further research on controlling the distribution pattern of the precipitated carbonate is needed.

# 4

# NUMERICAL INSIGHTS INTO THE POST-PEAK STRENGTH OF BIO-CEMENTED SANDS: A FOCUS ON GRAIN BRIDGING CEMENTATION

## 4.1. INTRODUCTION

Microbially induced carbonate precipitation (MICP) and enzyme induced carbonate precipitation (EICP) are promising methods for improving the mechanical performance of soils. Most experimental studies have shown that bio-cemented soils exhibit higher strength than uncemented soils at both peak and residual states (Figure 1.4) (Cui *et al.*, 2017; Nafisi *et al.*, 2020; Wu *et al.*, 2021). However, somewhat surprisingly, other studies have shown that bio-cemented soils can have a lower strength than uncemented soils at the post-peak state. Such a phenomenon has been observed, but not explained, in experiments reported by Gao *et al.* (2019), Terzis & Laloui (2019b), Nafisi *et al.* (2019) and Xiao *et al.* (2021b). The relevant data is summarised and plotted in Figure 4.1. Understanding the residual strength of bio-cemented soils, including this specific behaviour, is particularly important when bio-cemented soils are expected to be subjected to large strains, as this is the case in landslides and slope instability.

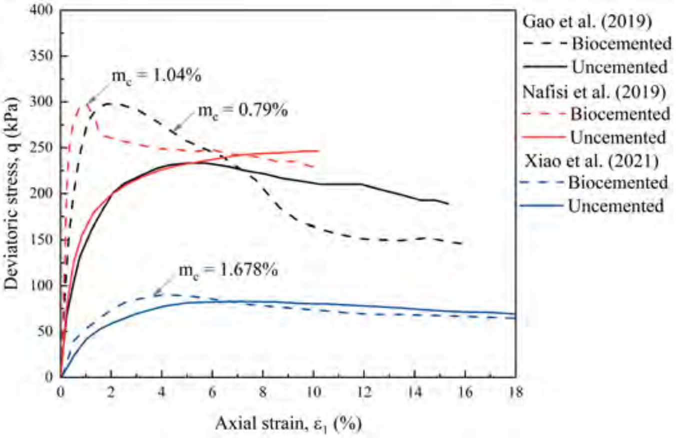

Figure 4.1: Experimental evidence illustrating the cases in which the post-peak strength of bio-cemented soil is lower than the uncemented soil. The data from Gao *et al.* (2019) and Nafisi *et al.* (2019) were obtained under 100 kPa of confinement, while the data from Xiao *et al.* (2021b) were obtained under 20 kPa of confinement. $m_c$ is the carbonate content by mass.

The low residual strength exhibited by some bio-cemented soils has not been captured in constitutive models (Gao & Zhao, 2012; Rahimi *et al.*, 2016; Gai & Sánchez, 2019) and DEM models for (bio-)cemented soils (Wang & Leung, 2008b; Jiang *et al.*, 2013; Shen *et al.*, 2016; Yang *et al.*, 2017). Specifically, these constitutive models assume that the critical state of (bio-)cemented soils either coincides with that of uncemented sands or is above. For DEM models of (bio-)cemented soils, the effects of cementation are usually simulated by introducing virtual bonds between soil grains instead of explicitly modelling cement agents. Such a simplification leads to the residual strength of cemented samples equivalent to, or above, that of the uncemented sample. The approach is not able to capture the post-breakage behaviour since the virtual bonds disappear after breakage. The 3D DEM study presented in Chapter 3 captured this behaviour. In Chapter 3, discrete element modelling was used to explicitly represent sand and carbonate particles, with a focus on the role of the carbonate distribution pattern. Four typical carbonate distribution patterns were modelled: grain bridging, contact cementing, coating and pore filling. It was found that carbonates distributed in the pattern of bridging led to a reduction in the residual strength as compared to that of uncemented soils, while other distribution patterns did not lead to a reduction in the residual strength. However, no further explanation was provided. Following Chapter 3, this chapter sheds light on the residual strength of bio-cemented sands with cementation in the form of grain bridging. It aims at understanding the factors that affect the residual strength of bio-cemented soils, and the reasons why grain bridging can lead to a lower residual strength as compared to uncemented soils.

This chapter is organised as follows. In Section 4.2, parametric studies are carried out on 3D DEM samples subjected to triaxial compression to investigate the effect of carbonate content, sand-carbonate cohesive strength and their relative Young's modulus on the macroscopic mechanical behaviour. Due to the challenges of visualising the results in three dimensions, 2D DEM simulations are carried out in Section 4.3. The 2D DEM model setup is presented first, followed by the macroscopic mechanical response of 2D DEM specimens subjected to biaxial compression. Microscopic observations during the biaxial compression tests are discussed in detail to explain the reasons why some bio-cemented soils can exhibit lower residual strength than uncemented soils. Finally, the main findings of this chapter are summarised in Section 4.4.

## 4.2. EFFECTS OF CEMENTATION CHARACTERISTICS ON THE MACROSCOPIC RESPONSE OF BIO-CEMENTED SAMPLES

In this section, a parametric study is carried out to investigate the effect of carbonate content, sand-carbonate cohesion, relative stiffness of carbonate and sand particles, and confining pressure on the residual strength of cemented samples with grain bridging. The 3D DEM sample preparation, inter-particle contact model and simulation procedure are similar to those presented in Chapter 3. The 3D DEM specimens are subjected to drained triaxial compression tests at different confining pressures. The parameters used are the same as those in Chapter 3, unless otherwise stated.

### 4.2.1. EFFECT OF CARBONATE CONTENT

Figure 4.2 shows the stress-strain response and volumetric behaviour of cemented samples with different carbonate contents subjected to drained triaxial compression at a confining stress of 100 kPa. For all carbonate contents considered, the response shows a reduction in residual strength compared to the uncemented sample. This suggests that, in the range considered, the residual strength is not sensitive to the carbonate content. In terms of volumetric behaviour, we note that the three cemented samples show a similar response at large strains: the volumetric strain decreases after having reached a maximum value.

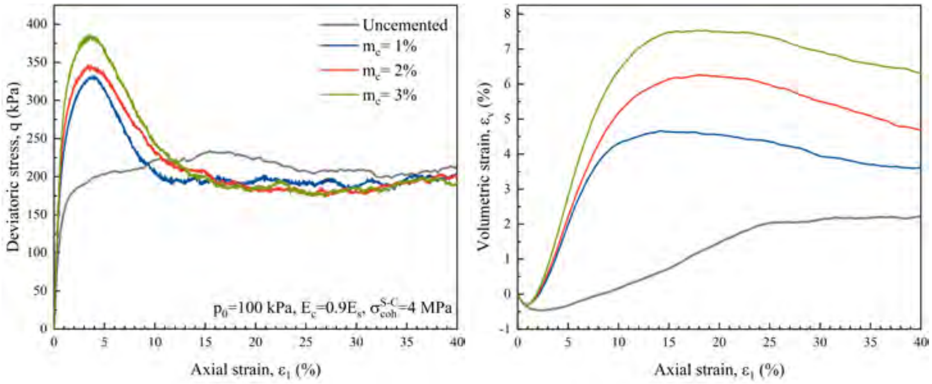

(a) (b)

Figure 4.2: Effect of the carbonate content on the (a) stress-strain and (b) volumetric responses of cemented samples.

### 4.2.2. EFFECT OF SAND-CARBONATE COHESION

As described in Chapter 3, the normal and shear resistances of between two particles of radius $R_1$ and $R_2$ in contact are given by:

$$F_n^{\max} = \sigma_{coh} \min\left(R_1, R_2\right)^2 \tag{4.1}$$

and

$$F_s^{\max} = \|\vec{F}_n\| \tan\varphi_c' + \sigma_{coh} \min\left(R_1, R_2\right)^2 \tag{4.2}$$

where $\sigma_{coh}$ is a cohesive strength parameter that controls the adhesion forces in the normal and tangential directions, and $\varphi_c'$ is the contact friction angle. $vecF_n$ is the contact normal force.

To justify the order of magnitude of sand-carbonate cohesion $\sigma_{coh}^{S-C}$ used in the DEM simulations, an axial tension test is modelled on a two-sand assembly cemented in the pattern of contact cementing. We consider different values of $\sigma_{coh}^{S-C}$ and compare the results of our simulation with the experimental results by Ren *et al.* (2021). Note that, although we focus on grain bridging in this chapter, we consider, for this exercise, contact cementing (in which all the precipitated carbonates are located at the grain contacts, as discussed in Zhang & Dieudonné (2023b)) as this distribution pattern is closer to the physical sample tested by Ren *et al.* (2021), as illustrated in Figure 4.3. The test results are presented in Figure 4.3. It can be seen that the case with $\sigma_{coh}^{S-C} = 4$ MPa best matches the experimental data, suggesting that $\sigma_{coh}^{S-C}$ of around 4 MPa is consistent with the physical properties of bio-cemented soils.

Figure 4.4 further shows the effect of sand-carbonate cohesion on the stress-strain and volumetric behaviour of cemented samples. We see that $\sigma_{coh}^{S-C}$ plays a crucial role in the residual strength of cemented samples. The residual strength of the cemented sample with a low $\sigma_{coh}^{S-C}$ value is lower than that of the uncemented sample. With increasing $\sigma_{coh}^{S-C}$, the residual strength of the cemented sample increases to the same level as the uncemented sample, and finally exceeds the residual strength of the uncemented sample.

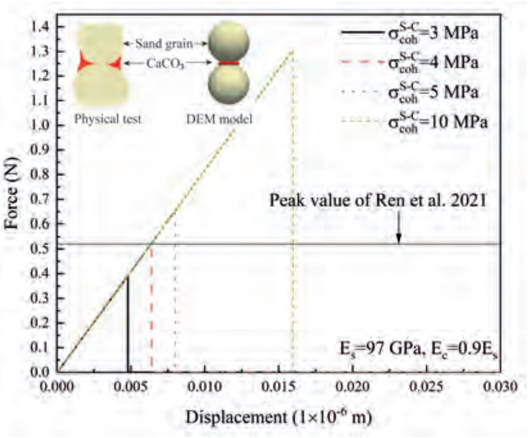

Figure 4.3: Tension test on two-sand assembly with all $CaCO_3$ precipitate at grain contact.

A case with $\sigma_{coh}^{S-C} = 0$ MPa, representing cohesionless carbonate particles, is also included in Figure 4.4. In this case, we also observe a reduction in the residual strength compared to the uncemented sample, indicating that grain bridging is one of the key factors that lead to such behaviour. It is worth noting that $\sigma_{coh}^{S-C}$ of 4 MPa lies in the range which exhibits lower residual strength than the uncemented sample referring to Figure 4.4. This suggests that it is possible for a bridging type of sample to exhibit a lower residual strength than the uncemented soil. Finally, we note that all cemented samples that exhibit a lower residual strength than the uncemented sample show a decrease in volumetric strain at large strains. With the increasing $\sigma_{coh}^{S-C}$, the decreasing trend of the volumetric strain in the post-peak phase gradually disappears.

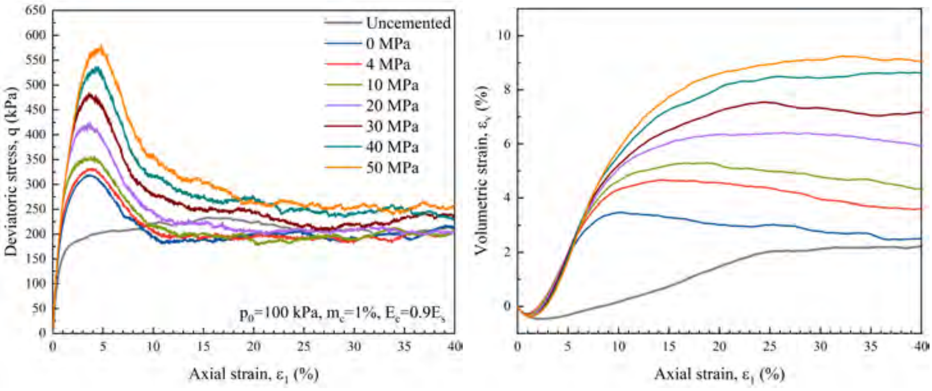

(a)

(b)

Figure 4.4: Effect of the sand-carbonate cohesion ($\sigma_{coh}^{S-C}$) on the (a) stress-strain and (b) volumetric behaviour of cemented samples with grain bridging.

### 4.2.3. EFFECT OF THE RELATIVE STIFFNESS OF CARBONATE AND SAND PARTICLES

Different polymorphs of calcium carbonate, including vaterite, aragonite, calcite and other meta-stable hydrated forms, can precipitate as a result of MICP. A review of the properties of these different polymorphs is presented in Chapter 5. The various polymorphs exhibit different elastic moduli $E_c$, ranging from 25 GPa to 91.28 GPa, leading to relative stiffness values of carbonate and sand particle $E_c/E_s$ between 0.3 to 1.2, assuming $E_s$ equal to the Young's modulus of quartz sand (77 GPa). Accordingly, we investigate in this section the effect of the relative stiffness of carbonate and sand particles on the response of bio-cemented soils.

Figure 4.5 shows the effect of the relative stiffness of carbonate and sand particles on the stress-strain and volumetric behaviour of cemented samples. It can be found that the ratio $E_c/E_s$ affects the residual strength of the cemented samples. Specifically, a lower $E_c/E_s$ leads to a minor difference in the residual strength between the cemented and uncemented samples. When $E_c$ is approaching $E_s$, the cemented sample shows a reduction in the residual strength. In terms of the volumetric behaviour, we see that the volumetric strain of the cemented samples, which exhibits a lower residual strength than the uncemented sample, decreases after reaching the maximum volumetric strain. By contrast, the case with $E_c/E_s = 0.1$ keeps a constant volumetric strain after reaching the maximum.

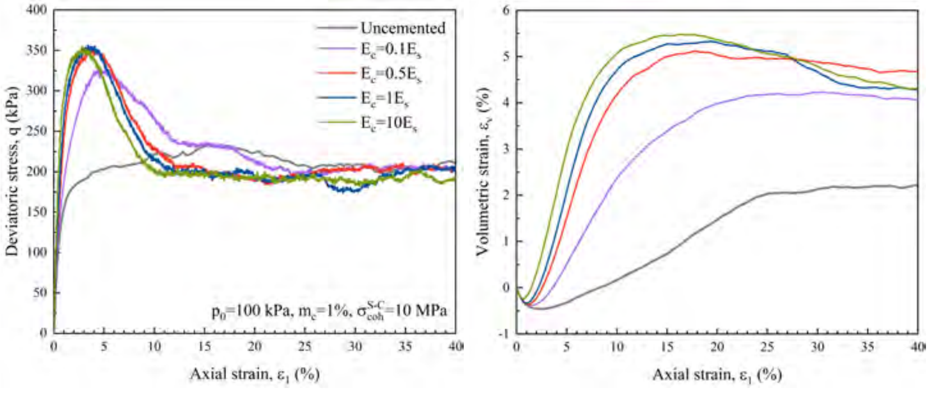

(a) (b)

Figure 4.5: Effect of the relative stiffness of carbonate and sand particles ($E_c/E_s$) on the (a) stress-strain and (b) volumetric behaviour of cemented samples with grain bridging. $E_s$ is fixed to 0.2 GPa.

Finally, our results show that when calcite precipitates as a result of MICP, the value of $E_c/E_s$ is approximately equal to 1, lying in the range which exhibits lower residual strength than the uncemented sample. This, again, suggests that it is possible for bio-cemented soils with grain bridging to exhibit a lower residual strength than uncemented soils.

### 4.2.4. EFFECT OF CONFINING PRESSURE

Figure 4.6 shows the effect of confining pressure on the stress-strain and volumetric behaviour of bridging type of samples. It can be seen that the cemented sample exhibits a lower residual strength than the uncemented sample under all the considered confining pressures. This finding suggests that the increasing confining pressure does not eliminate this phenomenon. For the volumetric behaviour, all the cemented samples presented herein show a decrease in volumetric strain after it reaches the maximum volumetric strain. Moreover, with the increasing confinement, the decreasing trend of volumetric strain in the post-peak phase gradually weakens.

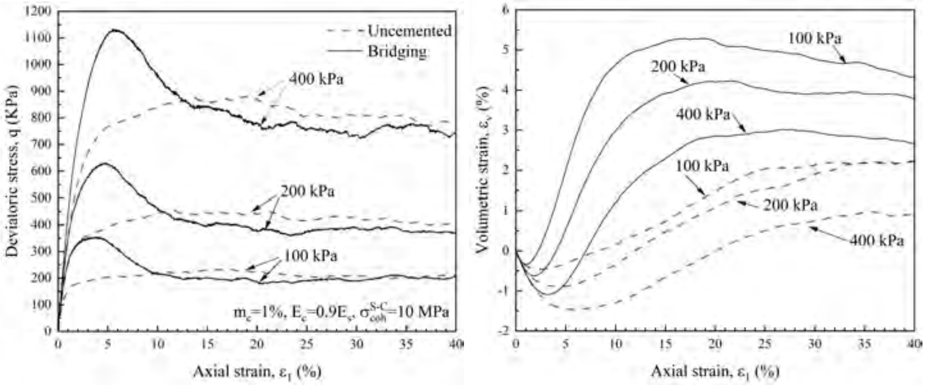

(a) (b)

Figure 4.6: Effect of confining pressure on the (a) stress-strain and (b) volumetric behaviour of cemented samples with grain bridging.

### 4.2.5. SHORT SUMMARY

The evolution of the residual strength of cemented samples with grain bridging with different characteristics is summarised in Figure 4.7. In this figure, the residual strength is defined as the deviatoric stress at 30% of axial strain. The residual strength of the uncemented sample is also included as the reference. It can be seen that the difference between the residual strength of a cemented sample and that of the uncemented sample depends on the relative stiffness of the carbonate and sand particles ($E_c/E_s$) and the sand-carbonate cohesive strength ($\sigma_{coh}^{S-C}$). On the other hand, the residual strength is insensitive to the carbonate content ($m_c$) and the confinement ($p_0$). Specifically, cemented samples without cohesion and with low sand-carbonate cohesion tend to show a lower residual strength than the uncemented sample. With the increase of sand-carbonate cohesion, the residual strength of the cemented sample increases to the same level as the uncemented sample, and finally exceeds the uncemented sample. As for the relative stiffness of carbonate and sand particles, a lower $E_c/E_s$ value leads to minor differences between the residual strength of cemented and uncemented samples. When $E_c$ approaches $E_s$, the cemented sample shows a reduction in the residual strength. This reduction in the residual strength is observed on cemented samples with different carbonate contents and subjected to different confining pressures.

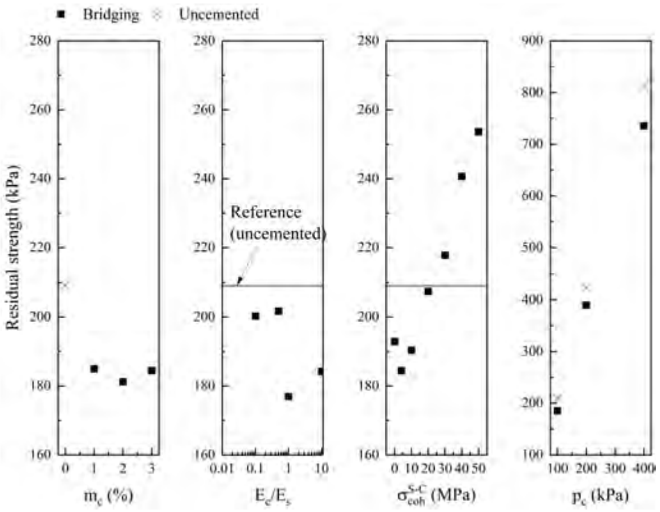

Figure 4.7: Summary of residual strength of bridging type of samples with different characteristics.

## 4.3. 2D DEM SIMULATION

The 3D DEM results indicate that the macroscopic mechanical behaviour of cemented samples with grain bridging depends on the relative Young's modulus of carbonate and sand ($E_c/E_s$) and the sand-carbonate cohesive strength ($\sigma_{coh}^{S-C}$). However, the reasons why these variables affect the mechanical response, especially the residual strength, remain unclear. In order to reveal the underlying mechanisms, 2D DEM simulations are carried out as it is easier to visualise the microscopic behaviour, such as strain localisation and force chain development, in two dimensions than in three dimensions.

### 4.3.1. 2D DEM MODEL SETUP

In a 1 m × 2 m domain formed by four rigid walls, 10000 spherical particles are randomly generated with all the particle centres located in a single layer. In terms of the size of the representative element volume (REV), Kuhn & Bagi (2009) carried out biaxial compression tests on 2D DEM assemblies that contain between 256 grains and 10816 grains. It was found that the oscillation in the stress-strain response decreased with an increasing number of particles. The difference in average stress-strain response between the cases with 4096 grains and with 10816 grains was quite consistent, and the local deformation could clearly be identified in both two cases. Therefore, samples with 10000 particles are adopted for 2D DEM simulations in this chapter. The two-dimensional conditions are simulated by placing the centres of all spheres on the same plane and blocking the translation and rotations in the out-of-plane direction. The radius expansion method is adopted for isotropic compression, during which the radii of the particles increase until the sample reaches a confining pressure (uniformly distributed force in 2D) $p_0$ of 4 kN/m. After that, the radius expansion is turned off to fix the size of the particles. The radii of sand grains are uniformly distributed with an average diameter ($d_{50}$) of 13.62 mm and a size ratio ($d_{\max}/d_{\min}$) of 2. Then, the inter-particle friction angle is adjusted to reach a target void ratio of 0.225. Note that the void ratio in 2D is defined as the area of voids to the area of solids in the plane in which the centres of particles lie. During that phase, the rigid walls are controlled by a servomechanism to maintain the confining pressure. After the generation of the host sand sample with target void ratio and confining pressure, $CaCO_3$ particles are introduced into the host sand sample. All the $CaCO_3$ particles are deployed at sand grain gaps to form grain bridging as demonstrated in Figure 4.8. The inter-particle contact law is the same as Zhang & Dieudonné (2023b). The parameters used in the 2D DEM model are listed in Table 4.1.

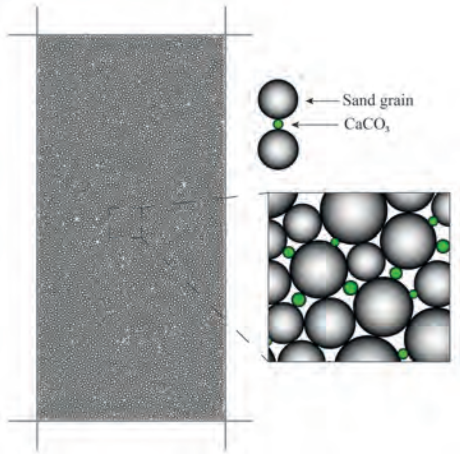

Figure 4.8: 2D DEM cemented sample with grain bridging.

Table 4.1: Properties of particles used in the 2D DEM simulations.

| Properties | Symbol | Unit | Sand | Carbonate |
|---|---|---|---|---|
| Density | $\rho$ | $kg/m^3$ | 2650 | 2710 |
| Young's modulus | $E$ | MPa | 200 | 180 |
| Shearing stiffness coefficient | $\nu$ | - | 0.3 | 0.3 |
| Friction angle | $\varphi'_c$ | ° | 16 | 16 |
| Rolling stiffness coefficient | $\alpha_r$ | - | 0.4 | 0.4 |
| Twisting stiffness coefficient | $\alpha_{tw}$ | - | 0.4 | 0.4 |
| Rolling resistance coefficient | $\eta_r$ | - | 0.4 | 0.4 |
| Twisting resistance coefficient | $\eta_{tw}$ | - | 0.4 | 0.4 |

### 4.3.2. 2D DEM MACROSCOPIC RESPONSE

The 2D DEM samples are subjected to biaxial compression tests. Figure 4.9 and Figure 4.10 show the effect of the sand-carbonate cohesion and the relative stiffness of carbonate and sand particles on the stress-strain and volumetric response of samples upon shearing. The 2D results are consistent with the 3D results presented in the previous section: the cemented samples with a relatively low $\sigma_{coh}^{S-C}$ value exhibit a lower residual strength than the uncemented sample and, with increasing $\sigma_{coh}^{S-C}$, the residual strength of cemented samples increases until exceeding the residual strength of the uncemented sample. Furthermore, all cemented samples first show contractive behaviour upon shearing, followed by an increase in volumetric strain. As shearing proceeds, the volumetric strain gradually increases. During that phase, the samples that exhibit a low residual strength tend to show a lower increase in volumetric strain than those that show a higher residual strength. The volumetric response in 2D is therefore different than that observed in 3D simulations (Figure 4.4 and Figure 4.5), where cemented samples exhibiting a lower residual strength than the uncemented sample showed a decrease in volumetric strain at large strains. This difference can be explained by the higher degrees of freedom of particles in 3D than in 2D.

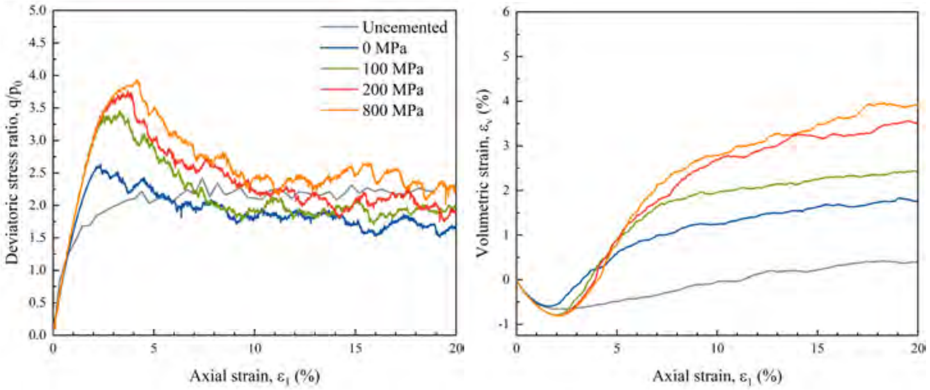

(a) (b)

Figure 4.9: Effect of the sand-carbonate cohesion on the (a) stress-strain and (b) volumetric behaviour of 2D cemented samples with grain bridging. A value of $E_c/E_s = 0.9$ is considered for the cemented samples.

## 4.3.3. 2D DEM MICROSCOPIC OBSERVATIONS

### KINEMATIC FIELDS

As observed in Section 4.3.2, the introduction of carbonates bridging sand grains leads to increased brittleness of the sample. In this section, the kinematic fields are analysed with the ambition to explain the macroscopic mechanical behaviour. Therefore, the kinematic fields of uncemented and cemented samples with different values of $\sigma_{coh}^{S-C}$ and $E_c/E_s$ are thoroughly analysed and compared. The analysis focuses on the incremental deviatoric strain, incremental volumetric strain and incremental grain rotation fields. The strain increment used to compute these fields is equal to 1% ($\Delta\varepsilon_1 = (\varepsilon_1 - 1\%) - (\varepsilon_1)$). Detailed information on the calculation of the incremental strain fields can be found in Catalano *et al.* (2014). For the incremental volumetric strain field, negative (positive) values, which are represented in blue (red), represent a contractive (dilative) behaviour.

The kinematic fields of 2D uncemented sample and cemented samples with $E_c/E_s = 0.9$ and $\sigma_{coh}^{S-C} = 0$ MPa, 100 MPa, 200 MPa and 800 MPa are presented in Figure 4.11 to 4.15, respectively. For the sake of comparison, the different incremental deviatoric strain fields

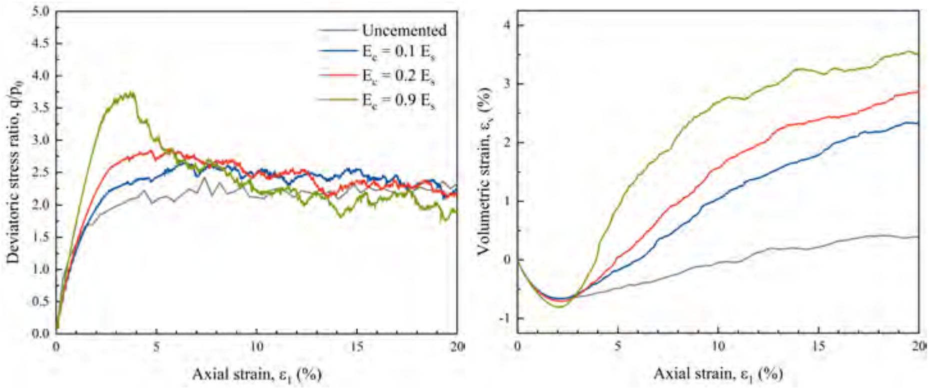

(a) (b)

Figure 4.10: Effect of the relative stiffness of carbonate and sand particles on the (a) stress-strain and (b) volumetric behaviour of 2D cemented samples with grain bridging. A value of $\sigma_{coh}^{S-C}$ = 200 MPa is considered for the cemented samples.

are gathered in Figure 4.16. Five interesting states are marked in the stress-strain curves and are selected to demonstrate the development of strain localisation. These states cover the pre-peak, peak, post-peak and residual states. The effect of the sand-carbonate contact cohesion can be investigated by comparing the cases with different values of $\sigma_{coh}^{S-C}$.

Figure 4.11 shows the kinematic fields of the uncemented sample. Diffuse deformation can be identified from the contours of the incremental deviatoric strain, incremental volumetric strain and grain rotation fields. This observation contrasts with the response of the cemented sample with $\sigma_{coh}^{S-C} = 0$ (Figure 4.12). In this case, while no strain localisation is observed at state 1, as shearing progresses to state 2 (peak-stress state), strain localises at some points. No clear shear band is visible yet. From 2.4% to 3.4% of axial strain (i.e. the beginning of the post-peak phase), these localised points initiated at state 2 further develop to form clear shear bands. Two well-developed shear bands, denoted B1 and B2, can be identified. In addition, two other shear bands (denoted B3 and B4) tend to form. At state 4, B1 and B2 stay active, while B3 and B4 evolve and join B1 and B2, forming together a closed shear band. At state 5, the formed shear bands remain and become stable.

By comparing the cemented sample with $\sigma_{coh}^{S-C} = 0$ and the uncemented sample, the effect of the introduced non-cohesive particles located in the bridging pattern can be analysed. We observe that the kinematic patterns are similar before the peak stress state, but show a difference after the peak (state 2). In particular, clear strain localisation in the form of shear bands occurs just after the peak stress state in the case of grain bridging cementation with $\sigma_{coh}^{S-C} = 0$. Moreover, the shear bands evolve and further develop in the post peak phase. The emergence and development of shear bands continuously weaken the sample, leading to a lower strength at the residual state compared to the uncemented sample (Figure 4.9a).

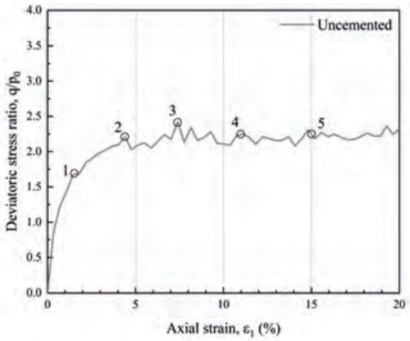

(a) Stress-strain curve

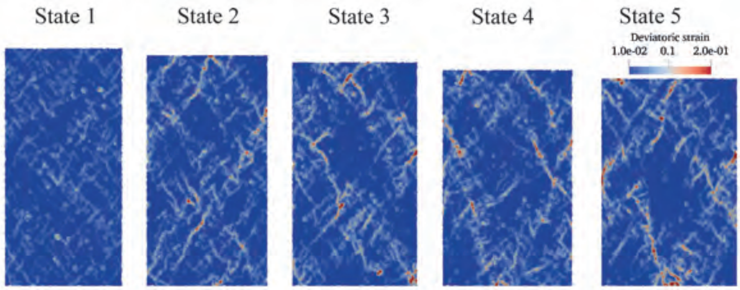

(b) Incremental deviatoric strain field

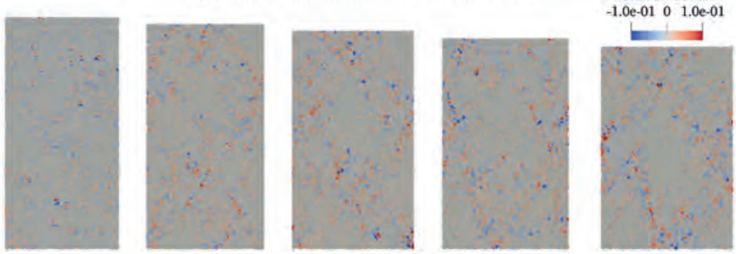

(c) Incremental volumetric strain field

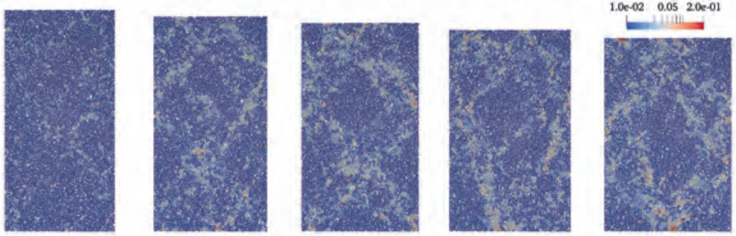

(d) Incremental grain rotation field

Figure 4.11: Kinematic fields of the uncemented sample upon biaxial compression.

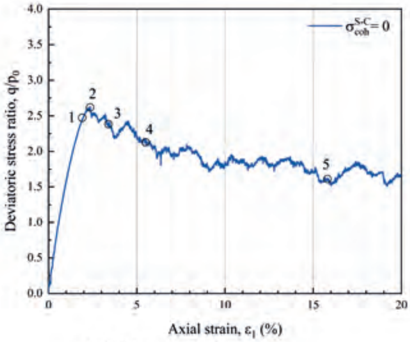

(a) Stress-strain curve

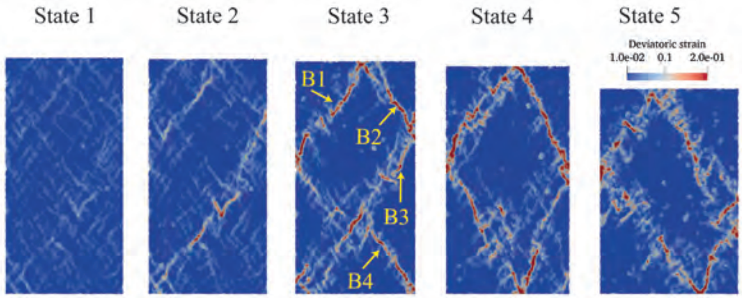

(b) Incremental deviatoric strain field

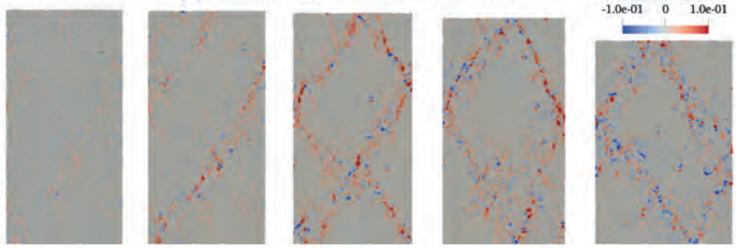

(c) Incremental volumetric strain field

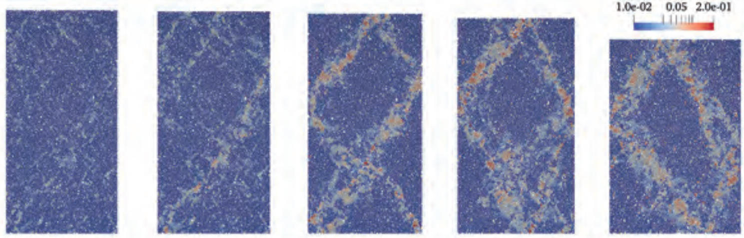

(d) Incremental grain rotation field

Figure 4.12: Kinematic fields of a cemented (grain bridging) sample with $\sigma_{coh}^{S-C} = 0$ MPa and $E_c/E_s = 0.9$ upon biaxial compression.

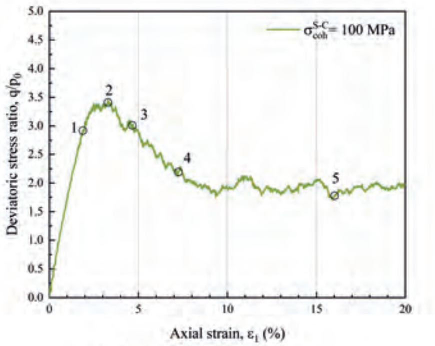

(a) Stress-strain curve

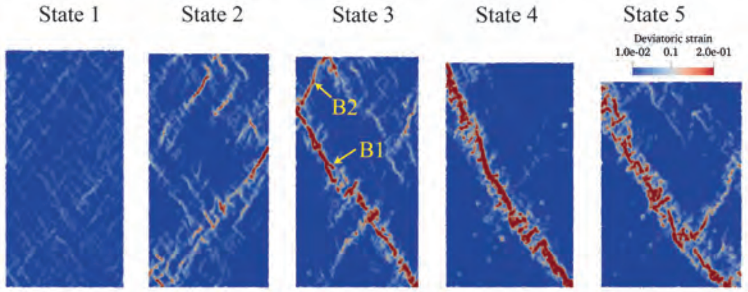

(b) Incremental deviatoric strain field

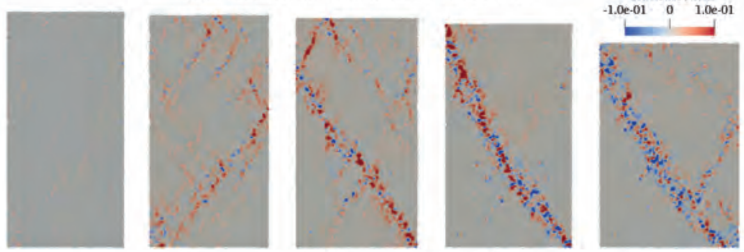

(c) Incremental volumetric strain field

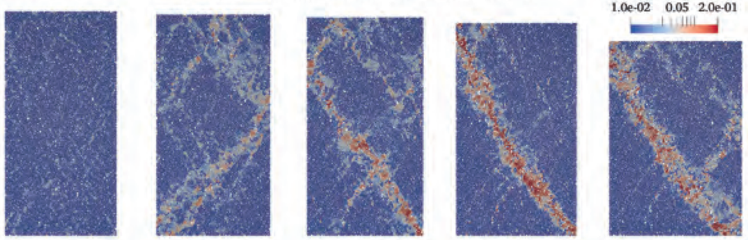

(d) Incremental grain rotation field

Figure 4.13: Kinematic fields of a cemented (grain bridging) sample with $\sigma_{coh}^{S-C}$ = 100 MPa and $E_c/E_s$ = 0.9 upon biaxial compression.

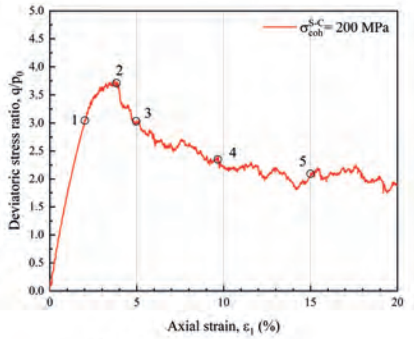

(a) Stress-strain curve

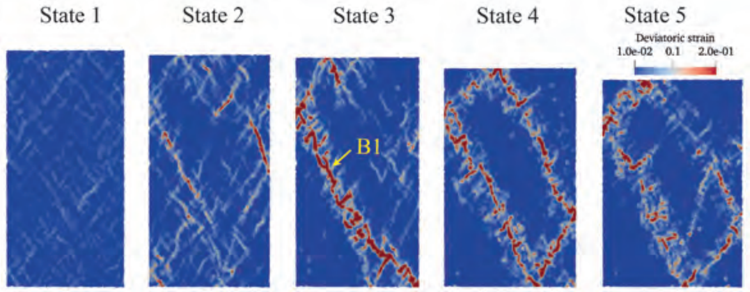

(b) Incremental deviatoric strain field

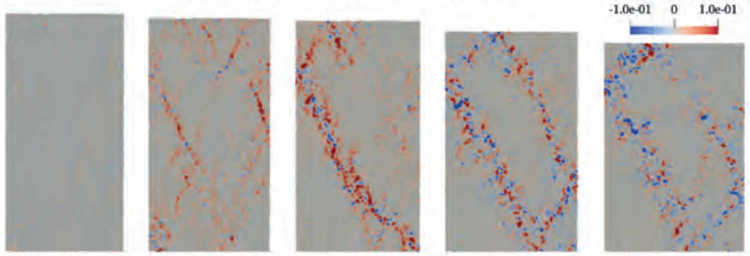

(c) Incremental volumetric strain field

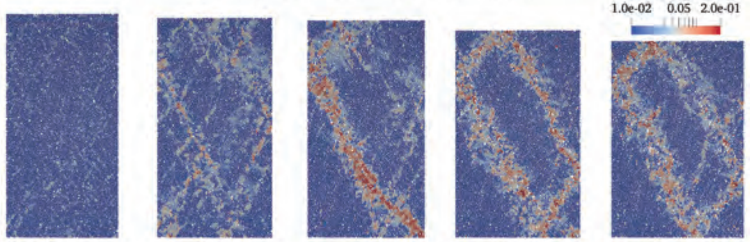

(d) Incremental grain rotation field

Figure 4.14: Kinematic fields of a cemented (grain bridging) sample with $\sigma_{coh}^{S-C}$ = 200 MPa and $E_c/E_s$ = 0.9 upon biaxial compression.

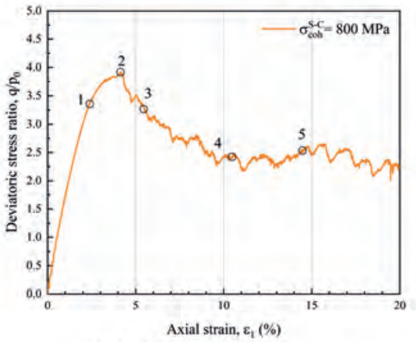

(a) Stress-strain curve

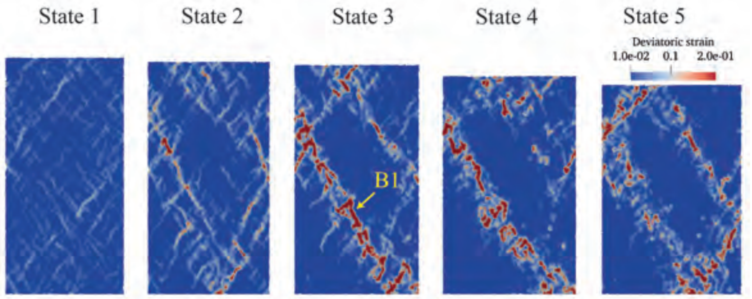

(b) Incremental deviatoric strain field

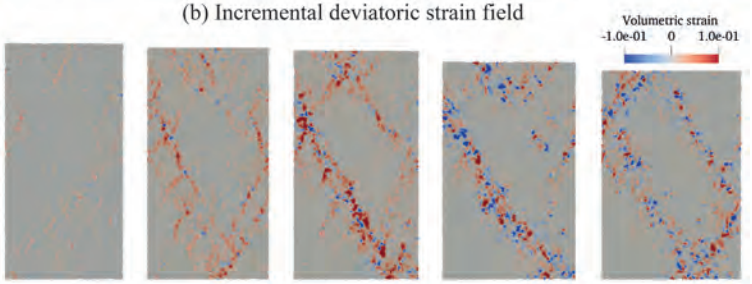

(c) Incremental volumetric strain field

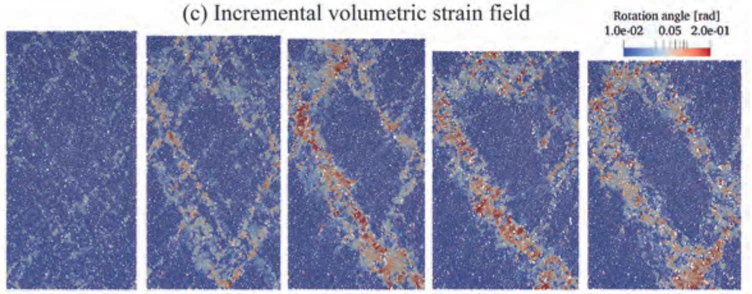

(d) Incremental grain rotation field

Figure 4.15: Kinematic fields of a cemented (grain bridging) sample with $\sigma_{coh}^{S-C}$ = 800 MPa and $E_c/E_s$ = 0.9 upon biaxial compression.

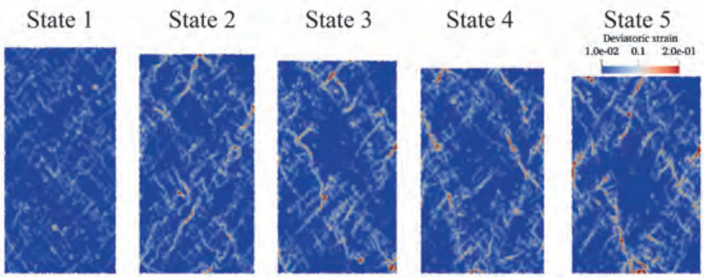

(a) Uncemented

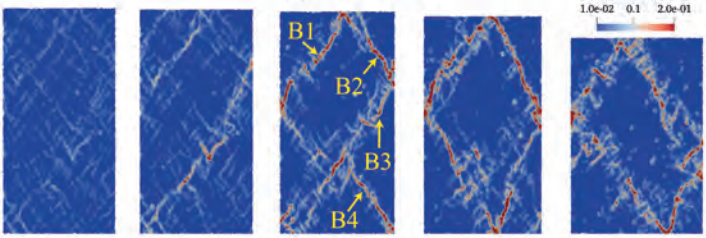

(b) 0 MPa

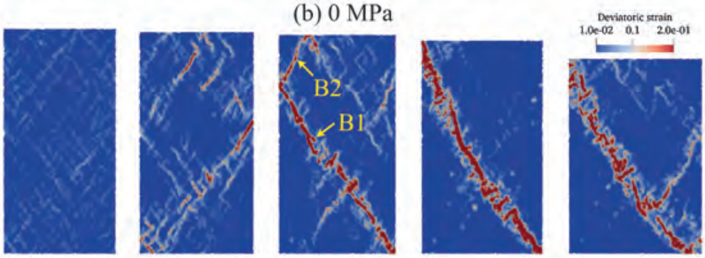

(c) 100 MPa

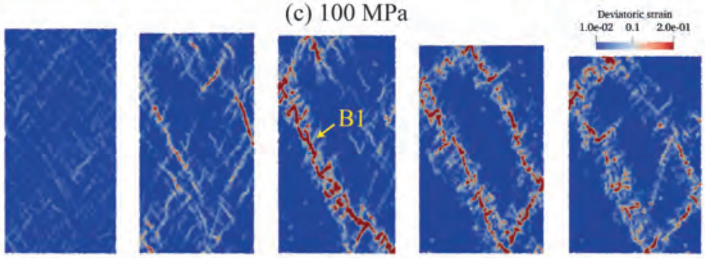

(d) 200 MPa

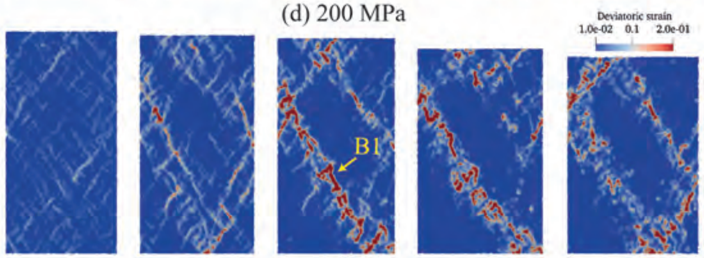

(e) 800 MPa

Figure 4.16: Comparison of the incremental deviatoric strain fields of uncemented and cemented (grain bridging) samples with various $\sigma_{coh}^{S-C}$. A value of $E_c/E_s = 0.9$ is considered for the cemented samples.

The localisation pattern of the cemented sample with $\sigma_{coh}^{S-C}$ = 100 MPa is similar to the case of $\sigma_{coh}^{S-C}$ = 0 at state 1 and state 2, as indicated in Figure 4.13. A well-developed shear band B1 can be observed at the post-peak state (state 3) in the case of $\sigma_{coh}^{S-C}$ = 100 MPa. Moreover, another shear band B2 initiates at state 3. When shearing proceeds to state 4, B2 vanishes and B1 further develops to become more pronounced. B1 remains active when the shearing approaches state 5. Comparing the cemented samples with $\sigma_{coh}^{S-C}$ = 0 and $\sigma_{coh}^{S-C}$ = 100 MPa, it can be seen that the presence of cohesion $\sigma_{coh}^{S-C}$ changes the kinematic pattern in the post-peak phase.

As $\sigma_{coh}^{S-C}$ increases to 200 MPa (Figure 4.14), the localisation pattern is comparable to the case of $\sigma_{coh}^{S-C}$ = 100 MPa at the pre-peak state, peak-stress state and the beginning of the post-peak state (state 3). The difference in the localisation pattern occurs in the late stage of the post-peak phase (state 4), in which a closed shear band can be observed instead of a single shear band as for the case of $\sigma_{coh}^{S-C}$ = 100 MPa. As $\sigma_{coh}^{S-C}$ further increases to 800 MPa (see Figure 4.15), B1 does not evolve to a closed shear band at state 4 as in the case of $\sigma_{coh}^{S-C}$ = 200 MPa. B1 becomes less active at state 4 and state 5.

Overall, the introduction of carbonate particles in the form of grain bridging, whether they are cohesive or not, modifies the kinematics of the sample and leads to the formation of shear bands. This finding is consistent with the experimental observation reported by Xiao *et al.* (2021b), in which repetitive mechanical tests were carried out on MICP-treated sands, and it was found that the treated samples showing lower residual strength tend to exhibit apparent shear bands. Comparing the cases of $\sigma_{coh}^{S-C}$ = 100 MPa, 200 MPa and 800 MPa (see Figure 4.16), it can be seen that a shear band is more clearly developed at the beginning of the post-peak state (state 3) for the case with a lower $\sigma_{coh}^{S-C}$. In addition, the formed shear band shows a more pronounced development for the case with a lower $\sigma_{coh}^{S-C}$. This suggests that the cemented samples with a lower $\sigma_{coh}^{S-C}$ suffer from a more severe strain localisation and hence more stress reduction. These findings explain the lower residual strength of the cemented sample with the decrease of $\sigma_{coh}^{S-C}$. The difference in the development of strain localisation can be explained by the difference in the bond breakage behaviour and the microstructure evolution, which are discussed in the following sections.

It is worth noting that the cemented sample with a high $\sigma_{coh}^{S-C}$ value (e.g. 800 MPa case) shows strain localisation but exhibits a higher residual strength than that of the uncemented sample. This is explained by the competition of two mechanisms. On the one hand, for the cemented samples with various $\sigma_{coh}^{S-C}$, the formation of shear band(s) in the post-peak phase weakens the sample, leading to the possibility of a lower residual strength than the uncemented sample. On the other hand, cohesive carbonates are introduced in the sample, and not all the bonds are broken in the post-peak phase. The unbroken bonds contribute to the increase of the residual strength of the sample, resulting in the possibility of a higher residual strength than the uncemented sample.

In conclusion, both mechanisms, namely, the formation of shear bands, which weakens the sample, and the remaining cohesive bonds, which enhance the sample strength, compete with each other and, together, dominate the overall residual strength. When $\sigma_{coh}^{S-C}$ is low, the weakening effect due to the formation of the shear band is dominant. As $\sigma_{coh}^{S-C}$ increases, the contribution to the residual strength becomes apparent, which leads to an increase in the residual strength with increasing $\sigma_{coh}^{S-C}$. For a high $\sigma_{coh}^{S-C}$, the contribution from the remaining bonds counteracts the weakening effect and hence results in a higher residual strength than that of the uncemented sample. In the following sections, the mechanical contribution of carbonates during the post-peak phase is elaborated from the point of view of bond breakage.

Figure 4.17 presents the kinematic patterns of the cemented sample with $E_c/E_s = 0.1$ and $\sigma_{coh}^{S-C} = 200$ MPa. The effect of the relative stiffness of the carbonate and sand particles can be assessed by comparing this case with the cemented sample of $E_c/E_s = 0.9$ and $\sigma_{coh}^{S-C} = 200$ MPa (Figure 4.14). It can be seen from Figure 4.17 that no mature shear band develops during the shearing. Accordingly, the deformation pattern can be characterised as diffuse. This kinematic pattern is similar to the uncemented sample, which also shows a diffuse pattern. By contrast, it is obviously different from the cemented sample with $E_c/E_s = 0.9$ and $\sigma_{coh}^{S-C} = 200$ MPa, in which clear shear bands are identified. This suggests that the cemented samples with a higher $E_c/E_s$ suffer from more severe strain localisation during the post-peak phase, and thus exhibit a lower residual strength than the one with a lower $E_c/E_s$.

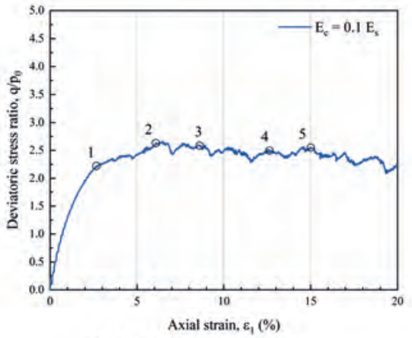

(a) Stress-strain curve

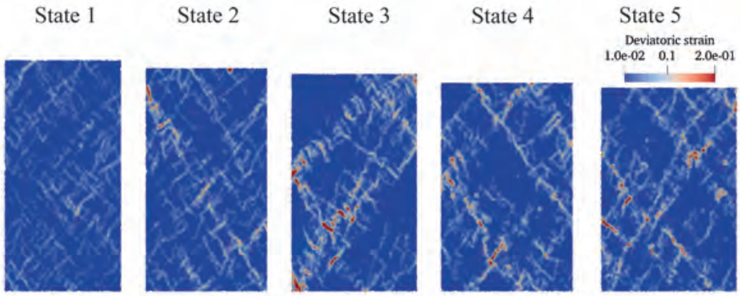

(b) Incremental deviatoric strain field

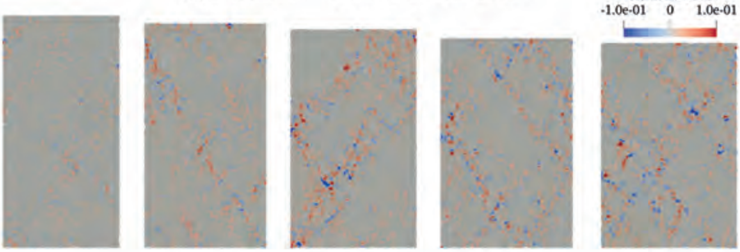

(c) Incremental volumetric strain field

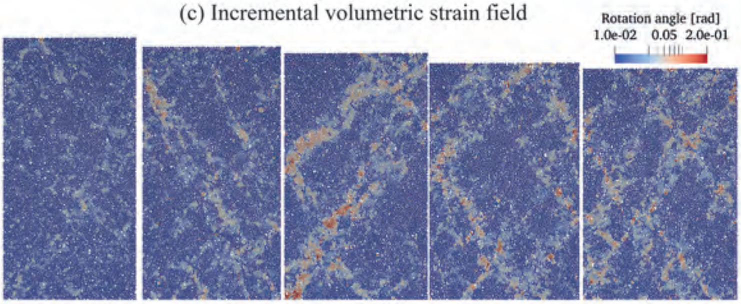

(d) Incremental grain rotation field

Figure 4.17: Kinematic fields of a cemented (grain bridging) sample with $\sigma_{coh}^{S-C} = 200$ MPa and $E_c/E_s = 0.1$.

### BOND BREAKAGE BEHAVIOUR

The evolution of bond breakage ratio for the cemented samples with different values of $\sigma_{coh}^{S-C}$ is compared in Figure 4.18 (solid lines). The bond breakage ratio is defined as the ratio of the number of broken $CaCO_3$ bonds to the number of initial $CaCO_3$ bonds. A similar trend of evolution of the bond breakage ratio can be observed in all three cases, in which the bond breakage ratio increases upon shearing. In addition, a higher $\sigma_{coh}^{S-C}$ leads to a lower bond breakage ratio, suggesting that more bonds are reserved when $\sigma_{coh}^{S-C}$ is high. The spatial distribution of breakage events correlates well with the incremental deviatoric strain field at the selected five states (Figure 4.19). The cases where $\sigma_{coh}^{S-C}$ = 100 MPa and 800 MPa are compared in Figure 4.19. It can be seen that for the case of $\sigma_{coh}^{S-C}$ = 100 MPa, breakage events (red dots) occur in most areas of the specimen. The areas which suffer from strain localisation show intensive breakage. This is more obvious in the case of $\sigma_{coh}^{S-C}$ = 800 MPa, in which the areas where breakage events occur are highly consistent with areas where strain localisation is present. These findings align with the fact that not all the bonds are broken in the post-peak phase and more bonds are retained with a higher $\sigma_{coh}^{S-C}$.

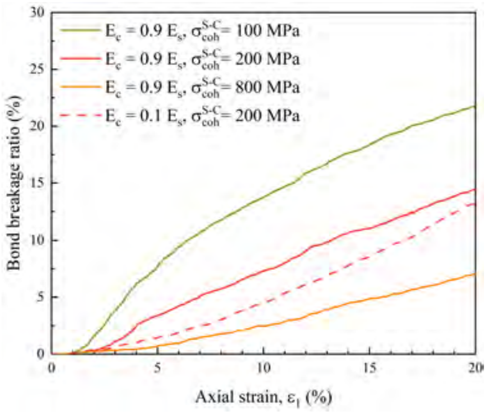

Figure 4.18: Evolution of bond breakage ratio of the bridging type of samples with various $\sigma_{coh}^{S-C}$.

Finally, the evolution of the bond breakage ratio of bridging type of samples with different $E_c/E_s$ is also compared in Figure 4.18 (red colour). It can be seen that the cemented sample with $E_c/E_s = 0.9$ shows a slightly higher bond breakage ratio than the one with $E_c/E_s = 0.1$. However, the spatial distribution of breakage events of the two cases is quite different, as presented in Figure 4.20. The breakage events are dispersed throughout the cemented sample with $E_c/E_s = 0.1$, corresponding to a diffuse deformation pattern. By contrast, the distribution of breakage events of the case with $E_c/E_s = 0.9$ is more concentrated, aligning with the distribution of strain localisation.

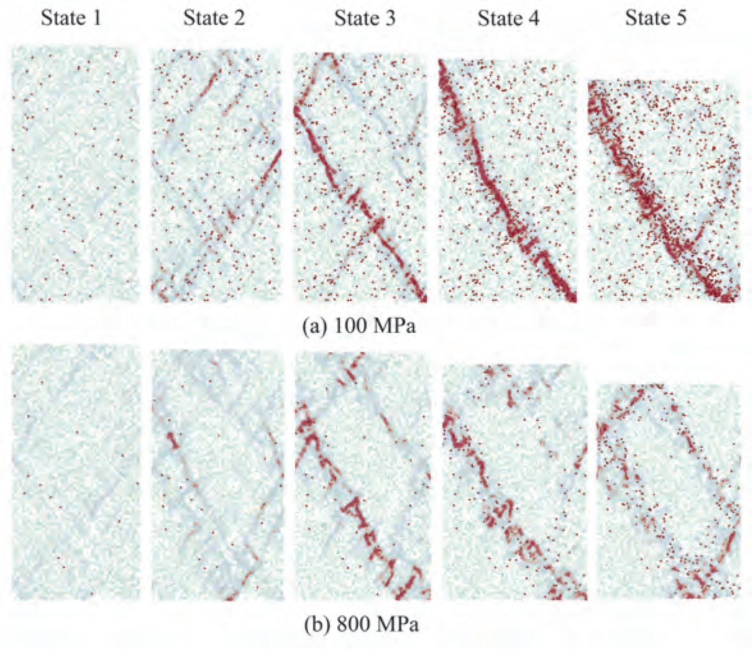

(a) 100 MPa

(b) 800 MPa

Figure 4.19: Spatial distribution of breakage events correlating with the incremental deviatoric strain field. Cases of $E_c/E_s = 0.9$, $\sigma^{S-C}_{coh}$ = (a) 100 MPa and (b) 800 MPa. Red dots represent the broken $CaCO_3$ bonds, and translucent green ones for unbroken $CaCO_3$ bonds. Note that the sizes of the dots are identical for better visualisation.

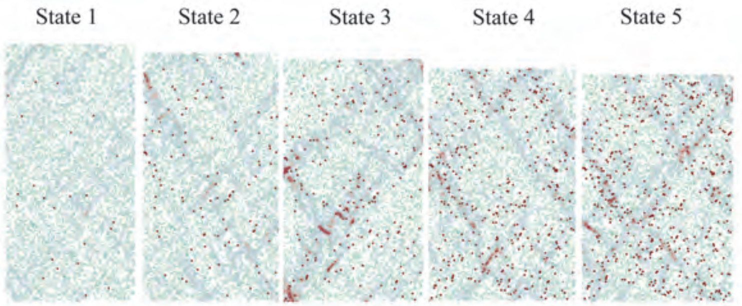

(a) $E_c = 0.1\ E_s$

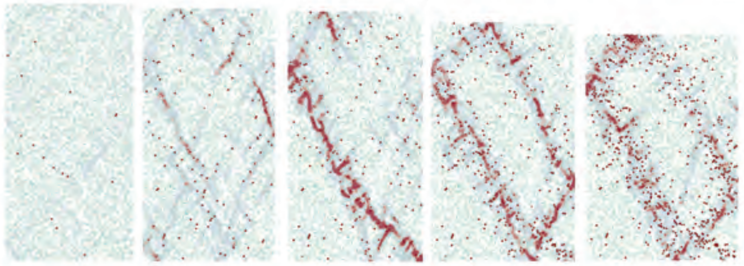

(b) $E_c = 0.9\ E_s$

Figure 4.20: Spatial distribution of breakage events correlating with the incremental deviatoric strain field. Cases of $\sigma_{coh}^{S-C}$ = 200 MPa, $E_c/E_s$ = (a) 0.1 and (b) 0.9. Red dots represent the broken $CaCO_3$ bonds and translucent green ones for unbroken $CaCO_3$ bonds. Note that the sizes of the dots are identical for better visualisation.

### GRAIN-SCALE INSTABILITY AND MICROSTRUCTURE EVOLUTION

We showed, in Section 4.3.3, that the introduction of carbonate particles bridging sand grains modifies the kinematics of the sample under load, and leads to the formation of shear bands. In this section, we explain how the introduction of carbonate particles can create a meta-stable structure leading to strain localisation.

In order to investigate how the introduction of cohesionless, or low-cohesion, carbonate particles bridging sand grains may affect the stability of the granular assembly, we first compare the stability of sand-sand and sand-carbonate contacts. To this end, we solve analytically the problem of grain sliding for both types of contacts, as shown in Figure 4.21. The grain-sliding test is designed to examine the impact of deflection on relative sliding. The problem assumes that the lower grain (either sand or carbonate) is fixed, while the upper sand grain is free of translation (note that only translation is considered here, and rolling is discussed later). A constant vertical force $\vec{F}$ is applied on the upper sand grain. The deflection $d$ is defined as the horizontal distance between the centres of the upper and lower grain grains. Note that a vertical displacement is introduced together with the applied deflection so that both grains are initially in contact. When both grains are vertically aligned, $d$ is equal to 0 (position represented by a dashed circle in Figure 4.21) and no sliding of the contact will occur upon loading. For a deflection $d > 0$, sliding occurs when the magnitude of the shear force $\|\vec{F}_s\|$ reaches the shear resistance $F_s^{\max}$. The higher the critical deflection that triggers sliding, the more stable the two-grain assembly.

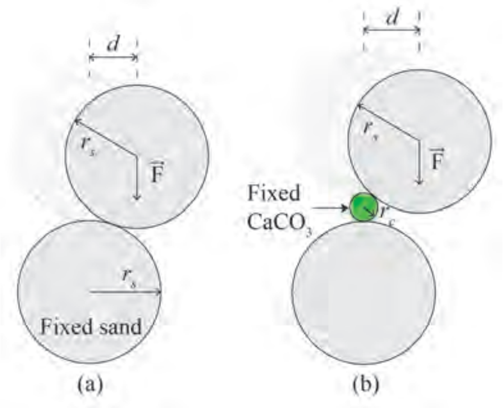

Figure 4.21: Analysis of the stability of two-particle assemblies: (a) sand-sand contact and (b) sand-carbonate contact. The radii $r_s$ of the upper and lower sand grains is the same and equal to the average radius of all sand particles in the 2D DEM sample (6.81 mm). The radius of the carbonate particle $r_c$ is equal to the average radius of all carbonate particles in the 2D DEM sample, namely 1.24 mm.

A force balance analysis of the upper sand grain of a two-particle assembly is presented in Figure 4.22. The applied vertical force $\vec{F}$ should be balanced by the reaction force from the grain in contact with the upper sand particle. The magnitudes of the normal and shear contact forces, $\vec{F}_n$ and $\vec{F}_s$, and of the reaction moment $\vec{M}$ are given by:

$$\|\vec{F}_n\| = \|\vec{F}\| \cos\theta \tag{4.3}$$

$$\|\vec{F}_s\| = \|\vec{F}\| \sin\theta \tag{4.4}$$

and

$$\|\vec{M}\| = \|\vec{F}\| r_s \sin\theta \tag{4.5}$$

where

$$\theta = \arcsin\left(\frac{d}{r_s + r}\right) \tag{4.6}$$

where $r$ is the radius of the grain in contact with the upper sand particle. The maximum shear force $F_s^{\max}$ and the maximum moment $M_r^{\max}$ are given by:

$$F_s^{\max} = \|\vec{F}_n\| \tan\varphi_c' + \sigma_{coh} \min(r_s, r)^2 \tag{4.7}$$

$$M_r^{\max} = \|\vec{F}_n\| \eta_r \tan\varphi_c' \tag{4.8}$$

The model parameters ($\varphi_c'$ and $\eta_r$) are given in Table 4.1.

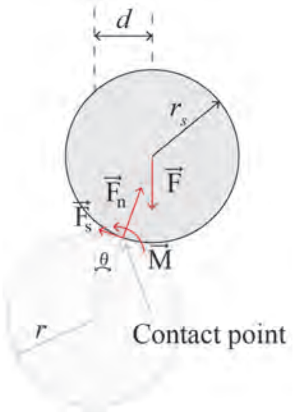

Figure 4.22: Force balance analysis on the upper sand grain of a two-particle assembly. $r$ is the radius of the grain in contact with the upper sand, such that $r = r_s$ in the case of a sand-sand contact and $r = r_c$ for a sand-carbonate contact.

Figure 4.23 presents the results of grain-sliding tests. In each test scenario, the evolution of shear force $\vec{F}_s$ and the maximum shear force $F_s^{\max}$ with the deflection $d$ are plotted. The grey area marks the region where there is no sliding ($\|\vec{F}_s\| < F_s^{\max}$). When $\|\vec{F}_s\| > F_s^{\max}$, sliding of the contact occurs. Figures 4.23(a-d) present the results for sand-sand and sand-carbonate contacts with various values of $\sigma_{coh}^{S-C}$ when a vertical force of 50 N is applied on the upper sand grain. Figure 4.23(e-f) presents the results for the same cases under a vertical force of 100 N. By comparing Figure 4.23(a) and Figure 4.23(b), or Figure 4.23(e) and Figure 4.23(f), it can be seen that, for a given vertical force, a larger deflection is required to trigger sliding of a sand-sand contact than a sand-carbonate contact. Indeed, the non-cohesive sand-carbonate contact can only tolerate a small deflection before sliding. In addition, as $\sigma_{coh}^{S-C}$ increases, the non-sliding zone of the sand-carbonate contact increases and can exceed the critical deflection of a sand-sand contact. These findings indicate that a sand-sand contact is able to withstand greater disturbance without sliding, while the introduction of non-cohesive carbonate, or carbonate with low cohesion, tends to form a meta-stable structure prone to sliding. This further supports that relative movements of the granular assembly are more likely to occur at sand-carbonate contacts than at sand-sand contacts. Finally, a higher $\sigma_{coh}^{S-C}$ can compensate for this instability and lead to a more stable structure.

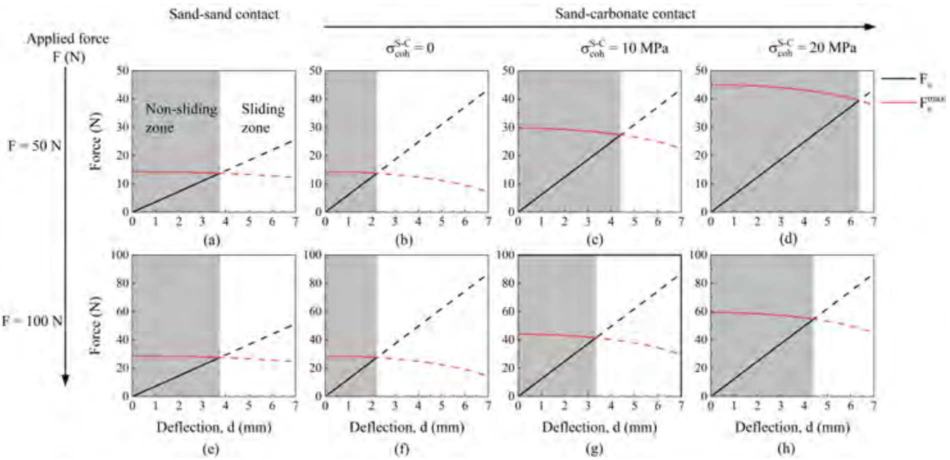

Figure 4.23: Comparison of the critical deflection triggering sliding for sand-sand and sand-carbonate contacts with various $\sigma_{coh}^{S-C}$.

Comparing Figure 4.23(c) and Figure 4.23(g), or Figure 4.23(d) and Figure 4.23(h), the sand-carbonate contact exhibits a larger non-sliding zone at a low applied force, for a given $\sigma_{coh}^{S-C}$. This finding explains the fact that a cemented sample with a low $E_c/E_s$ ratio tends to be more stable at the grain scale than a sample with a higher $E_c/E_s$ ratio, Indeed, the average sand-carbonate contact force in the former case is lower than that of the later case (Figure 4.24).

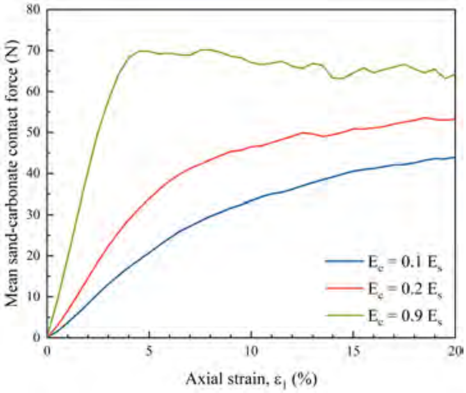

Figure 4.24: Evolution of the mean sand-carbonate contact force for cementation in the form of grain bridging, with various $E_c/E_s$ ratio values. $\sigma_{coh}^{S-C}$ = 200 MPa in the results presented herein.

Apart from grain sliding, relative rolling of particles in contact can occur. We consider the cases represented in Figure 4.21, in which the bottom grain (either sand or carbonate) is fixed, and the upper sand grain is free to roll. As soon as a deflection $d$ is applied, a moment is generated, which may drive relative rolling of the grains if the rolling moment $M_r$ reaches the maximum rolling moment $M_r^{\max}$. The larger the critical deflection that triggers rolling, the more stable the two-grain assembly against rolling. Figure 4.25 presents the results of grain-rolling tests. It should be noted that cohesion is not introduced in the rolling direction (see contact law described in Section 3.2.1), hence the response of sand-carbonate contact with various $\sigma_{coh}^{S-C}$ is the same as the case of $\sigma_{coh}^{S-C} = 0$. It can be seen from Figure 4.25 that the sand-carbonate contact exhibits a significantly smaller non-rolling area than sand-sand contact, indicating the instability of sand-carbonate contacts against rolling. This finding suggests that rolling is more prone to occur at sand-carbonate contacts than sand-sand contacts.

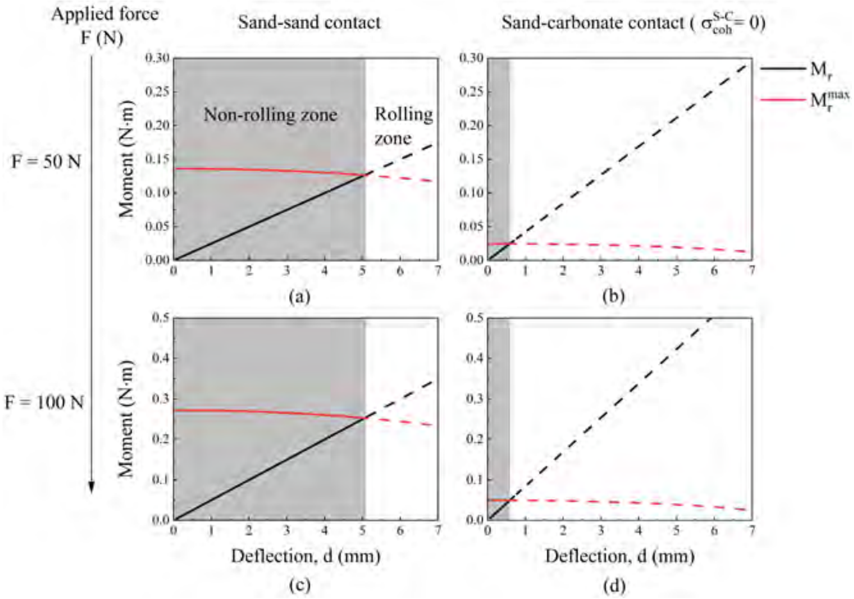

Figure 4.25: Comparison of critical deflection triggering rolling for sand-sand contact and sand-carbonate contact.

The difference in grain-scale stability further affects the arrangement of particles at the meso-scale (the scale considering a group of particles). To elaborate on how $\sigma_{coh}^{S-C}$ affects the particle arrangement at the mesoscale, a group of particles is monitored to demonstrate their evolution upon shearing. Figure 4.26 compares the micro-architecture evolution of the selected particles of cemented samples with $\sigma_{coh}^{S-C} = 100$ MPa and 800 MPa. It can be seen that, for $\sigma_{coh}^{S-C} = 100$ MPa, the arrangement of the particles remains the same until reaching an axial strain of 6%, while bond breakage occurs until then. The broken bonds create areas prone to slippage, as indicated by the dash lines in Figure 4.26(a). From 6% to 7% of axial strain, the left part of the particles moves along the slip lines with respect to the right part of the particles. From 7% to 10% of axial strain, the left sub-part further moves, creating a large local void. In contrast, there is no obvious relative movement of the right subpart. As shearing proceeds, more bonds break, and the left part of the particle assembly undergoes frequent rearrangement. On the other hand, for $\sigma_{coh}^{S-C} = 800$ MPa, it can be seen that fewer bonds break, and the microstructure remains almost the same during the whole process, as shown in Figure 4.26(b). By comparing both cases, it can be inferred that $\sigma_{coh}^{S-C}$ plays an important role in the particle rearrangement. A higher $\sigma_{coh}^{S-C}$ can limit particle rearrangement and contribute to forming a more stable micro-architecture and therefore a higher strength.

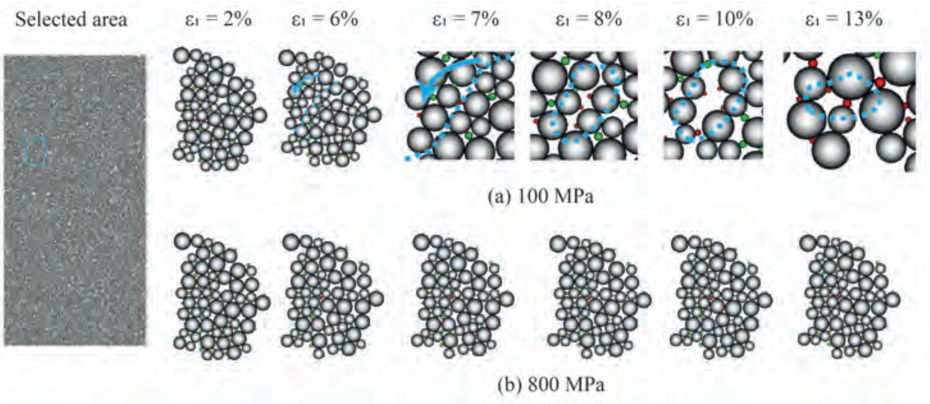

Figure 4.26: Microstructure evolution of samples with grain bridging, with $E_c/E_s = 0.9$ and $\sigma_{coh}^{S-C}$ = (a) 100 MPa and (b) 800 MPa. The grey particles represent sand grains, the green ones represent unbroken carbonate bonds, and the red ones represent broken carbonate bonds.

## 4.4. DISCUSSIONS AND CONCLUSIONS

In some reported experimental studies, bio-cemented soils, which are expected to exhibit strength improvement, surprisingly show a lower strength than uncemented soils at residual state. Such a phenomenon has not been analysed and is poorly understood. This chapter, for the first time to the best of the authors' knowledge, addresses the following question: can bio-cementation contribute negatively to soil strength? To answer this question, DEM simulations in both 3D and 2D are carried out to understand the factors that may lead to such behaviour and the underlying mechanisms.

It is found, from 3D DEM results, that bio-cemented sands with carbonates located at grain gaps (i.e. bridging pattern) can exhibit a lower residual strength than the corresponding host sand, depending on the cohesion strength of the precipitation-grain contact and the relative Young's modulus of the minerals. On the other hand, the results show to be independent from the carbonate content (in the range of 1% to 3%) and confining pressure. This phenomenon is reproduced in 2D DEM, and detailed observations from grain-scale instability, mesoscale structure evolution, global strain localisation and bond breakage are analysed. The results suggest that the introduction of carbonate particles bridging sand grains, whether they are cohesive or not, modifies the structure of the granular assembly and its stability, by affecting the sample kinematics. Non-cohesive carbonates and low-cohesive carbonates in the bridging pattern are more likely to lead to a meta-stable structure. This meta-stable structure is prone to the relative movement of particles, which in turn leads to the development of shear bands and, overall, a lower residual strength. Moreover, stronger cohesive carbonates can compensate for this instability and lead to a more stable microstructure, which contributes to the improvement of the global residual strength. Both mechanisms, namely the development of shear bands due to grain-scale instability and the cohesive bonds, compete with each other and together dominate the overall residual strength. When the sand-carbonate cohesive strength is low, the weakening effect due to the formation of the shear band is dominant. With increasing the cohesive strength, the contribution to residual strength manifests which leads to an increasing trend of residual strength.

# 5

# DEM INVESTIGATION OF THE SMALL-STRAIN STIFFNESS OF BIO-CEMENTED SANDS

---

Parts of this chapter appear in Zhang *et al.* (2024).

## 5.1. INTRODUCTION

Bio-mediated soil improvement methods have attracted significant attention in civil engineering in recent years (Mitchell & Santamarina, 2005; DeJong *et al.*, 2006; Whiffin *et al.*, 2007; Ivanov & Chu, 2008; Hamdan & Kavazanjian Jr, 2016; Terzis & Laloui, 2018; Xiao *et al.*, 2021c). Prominent techniques include microbially induced carbonate precipitation (MICP) and enzyme induced carbonate precipitation (EICP). These methods rely on geochemical reactions to drive the precipitation of calcium carbonate, which can act as cementing agent and bond soil grains. As a result, MICP and EICP are able to improve the mechanical properties of soils and can be applied for soil stabilisation (see van Paassen *et al.*, 2010; Xiao *et al.*, 2018; Darby *et al.*, 2019; Zhang *et al.*, 2020; Cui *et al.*, 2021; Zeng *et al.*, 2021; Ma *et al.*, 2022; Xiao *et al.*, 2022, among others).

Despite the promising perspectives of bio-mediated methods, critical challenges have impeded bio-mediated methods from being translated into practice at the industrial scale. A widely recognised challenge is the uncertainty of bio-mediated treatment (van Paassen *et al.*, 2010; Krishnan *et al.*, 2021; Montoya *et al.*, 2021; Xiao *et al.*, 2021b). Due to the intrinsic heterogeneous nature of the subsurface, obtaining a uniform treatment in the field has proven difficult, and the spatial distribution of the precipitated carbonate crystals is affected by significant uncertainty. Furthermore, laboratory studies have shown that the distribution pattern of carbonate crystals within the pore space of soils can vary significantly. These uncertainties are found to lead to large variations in the mechanical performance of bio-cemented soils, as discussed in Chapter 3, again hindering the practical implementation of bio-mediated methods. Therefore, it is important to increase confidence in the effectiveness and mechanical efficiency of bio-treatment methods.

To ascertain the improvement of bio-mediated treatment, different measurements, including mechanical tests (e.g. uniaxial or triaxial tests), acid washing and micro-computed tomography, can be used to quantify the mechanical improvement and mass content of the precipitated carbonate. However, these measurements are destructive and costly. Moreover, the measured quantities only provide information on the local mechanical efficiency and effectiveness of the treatment. Therefore, non-destructive characterisation methods that are easy to implement on-site at a large scale are much preferred.

Seismic monitoring is often an effective tool in geotechnical engineering (Rinaldi & Santamarina, 2008; Weil *et al.*, 2012; Zeng *et al.*, 2022). It can provide real-time and non-destructive monitoring of the wave signal of the subsurface. Seismic measurements rely on detecting and recording wave signals resulting from an artificial source and travelling through the subsurface. The wave velocity (e.g. shear wave velocity) can be derived from the collected data. The derived wave velocity is often used for process monitoring throughout biotreatment (DeJong *et al.*, 2006; van Paassen *et al.*, 2010; Riveros & Sadrekarimi, 2020; Nafisi *et al.*, 2020). However, the information behind the shear wave velocity remains to be understood. Specifically, what factors affect the measured shear wave velocity and how to interpret the measured shear wave velocity of bio-treated soil are still to be investigated.

This chapter contributes to the interpretation of the obtained shear wave velocity in laboratory tests, which supports shear wave measurement to assess the mechanical efficiency and effectiveness of bio-mediated treatment. Fundamental insights on the effect of bio-cementation on the shear wave velocity of bio-cemented soils are provided in an indirect way, i.e. by examining the small-strain stiffness ($G_0$) of bio-cemented soils instead of directly measuring the shear wave velocity ($V_s$).

## 5.2. FACTORS AFFECTING $G_0$ OF BIO-CEMENTED SOIL

Potential factors that may affect the small-strain stiffness of bio-cemented soil could be the properties of the host soil and the characteristics and amount of the precipitated crystals. From the point of view of soil (specifically, uncemented soil), the effects of properties of soils on $G_0$ have been extensively studied, including void ratio, confining pressure, particle size distribution (e.g. mean particle size $D_{50}$ and coefficient of uniformity which is defined as $\frac{D_{60}}{D_{10}}$). It is found that $G_0$ increases with decreasing void ratio and increasing confining pressure, and $G_0$ decreases as $C_u$ increases while $G_0$ is independent of $D_{50}$ (Iwasaki & Tatsuoka, 1977; Wichtmann *et al.*, 2009; Yang & Gu, 2013; Gu *et al.*, 2017, among others). Despite the fact that $G_0$ of soils with various properties have been widely studied, how various properties of soils affect the contribution of bio-cementation to $G_0$ remains to be explored. From the point of view of bio-cementation, the effects of the precipitated crystals with different characteristics on $G_0$ are not well studied. The characteristics of crystals include crystal polymorph and distribution pattern. Specifically, calcium carbonate can precipitate in the form of different polymorphs (i.e. vaterite, aragonite or calcite) and metastable hydrated forms during MICP treatment (Clarà Saracho *et al.*, 2020). In addition, the precipitated crystals can exhibit different distribution patterns in the pore space of the host soil (DeJong *et al.*, 2010; Lin *et al.*, 2016; Mujah *et al.*, 2017; Wang *et al.*, 2022; Zhang & Dieudonné, 2023b). As conceptualised (see Zhang & Dieudonné (2023b) for the detailed conceptualisation from scanning electron microscopy (SEM) images) in Figure 5.1, typical distribution patterns could be: bridging, which refers to carbonates located at the gap between sand grains and connects sand grains; contact cementing, representing those carbonate crystals that are located at contacts between sand particles; coating, referring to carbonates coating the sand grains; and pore filling, which represents carbonates filling in the void space and not bonding to sand grains. Previous studies (Zhang & Dieudonné, 2023a,b) showed that different distribution patterns of crystals lead to significantly different impacts on the mechanical properties of bio-cemented sand. Therefore, to precisely describe the mechanical behaviour of bio-cemented soils, it is critical to identify not only the total amount of the precipitated crystals but also the proportions of crystals of each distribution pattern. Understanding how seismic measurements provide information on the characteristics of crystal distribution patterns is thus of importance.

In order to reveal the mechanisms underlying the effect that particle size distribution, crystal content and property and distribution pattern have on the small-strain stiffness of bio-cemented sands, particle-scale modelling is essential. Therefore, the discrete element method (DEM) is used in this chapter to model bio-cemented sands. To account for various microscopic characteristics, the precipitated crystals are explicitly modelled at pre-defined locations. The DEM samples are subjected to static probing (drained triaxial test at small strain) to assess the small-strain stiffness (Magnanimo *et al.*, 2008; Gu *et al.*, 2013; Perez *et al.*, 2016; Gu & Yang, 2018; Gong *et al.*, 2019; Shi *et al.*, 2020; Nie *et al.*, 2022; Reddy *et al.*, 2022). Static probing is effective as reported by Cheng *et al.* (2020), who found that the wave velocity derived from static probing is the same as the long-wavelength

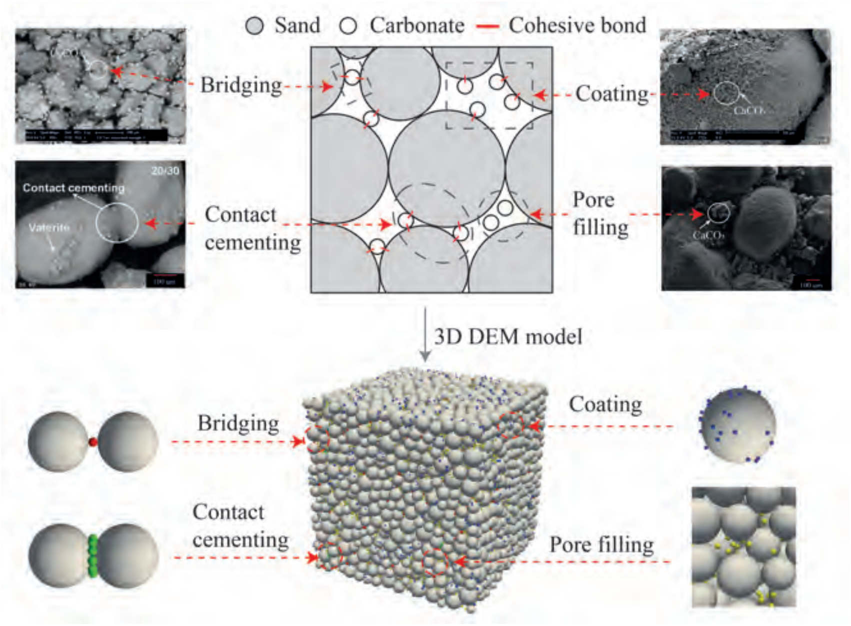

Figure 5.1: Scanning electron microscopy (SEM) image, conceptualisation and DEM model example of bio-cemented soils with various distribution patterns of precipitated carbonates. SEM image illustrating bridging is from van Paassen (2009); SEM image for contact cementing from Lin *et al.* (2016); SEM image for coating from Cheng *et al.* (2016) and the one for pore filling is from Wu *et al.* (2021).

wave velocity derived from dynamic probing (simulating propagation of elastic wave).

The content of this chapter is organised as follows: Section 5.3 describes the DEM methodology in detail. Section 5.4 and 5.5 present the simulation results of the small-strain stiffness of bio-cemented soils with different characteristics and the underlying mechanisms which are obtained from microscopic observations. Section 5.7 investigates the correlation between the small-strain stiffness and peak strength of bio-cemented samples. Section 5.8 summarises the main conclusions of this chapter and discusses practical implementations for supporting shear wave velocity measurements to assess the mechanical efficiency and effectiveness of bio-mediated treatment.

## 5.3. METHODOLOGY

### 5.3.1. DEM SAMPLE PREPARATION

DEM simulations are performed using the open-source platform YADE (Šmilauer *et al.*, 2021). Bio-cemented samples are modelled in two steps: an uncemented sample is generated as the host sand, after which smaller spheres representing carbonate crystals are introduced. In order to prepare the uncemented sample, a set of spherical particles is generated inside a cubic space confined by three pairs of rigid and frictionless walls. The reference particle size distribution (PSD) shown in Figure 5.2 is used throughout this chapter unless otherwise stated (in Section 5.4.4). It has a coefficient of uniformity $C_u$ =

1.4 and $D_{max}/D_{min} = 3.31$. The particles are not in contact with each other initially. The host sand sample is compacted by controlling the three pairs of walls to move towards the centre of the cube. The compaction process is terminated once the confining pressure reaches 100 kPa. At that moment, the inter-particle friction angle is adjusted to reach a target void ratio $e$ while keeping the confining pressure equal to 100 kPa. Unless otherwise stated, the target void ratio is 0.695. After the generation of the uncemented sample, carbonate particles are introduced into the host sand at designed locations to obtain cemented samples with specific distribution patterns and carbonate contents, as illustrated in Figure 5.1. Cemented samples with a single carbonate distribution pattern, namely bridging, contact cementing, coating or pore filling, as well as cemented samples with mixed distribution patterns, are generated and subjected to static probing.

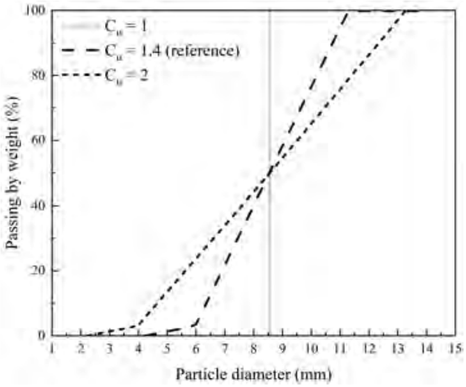

Figure 5.2: Particle size distributions of the uncemented (host) sand.

### 5.3.2. CONTACT MODEL

The contact model used in this chapter is based on the classical linear elastic-plastic law from Cundall & Strack (1979), with the introduction of cohesion. It is briefly introduced below. Details of this contact model can be found in Šmilauer *et al.* (2021).

For two spheres of radii $R_1$ and $R_2$ in contact, the normal force $\vec{F}_n$ and incremental shear force $\Delta\vec{F}_s$ are calculated as:

$$\vec{F}_n = k_n u_n \vec{n} \tag{5.1}$$

and

$$\Delta\vec{F}_s = -k_s \Delta\vec{u}_s \tag{5.2}$$

where $u_n$ is the relative normal displacement of the two spheres, $\vec{n}$ is the normal contact vector and $\Delta\vec{u}_s$ is the incremental tangential displacement. $k_n$ and $k_s$ are the contact normal stiffness and tangential stiffness respectively, which are given by:

$$k_n = \frac{2E_1R_1E_2R_2}{E_1R_1 + E_2R_2} \tag{5.3}$$

and

$$k_s = \nu k_n \tag{5.4}$$

where $E_i$ $(i = 1,2)$ is the modulus of elasticity of sphere $i$, and $\nu$ is the shear stiffness coefficient. The normal and shear resistances are equal to:

$$F_n^{max} = \sigma_{coh} \min(R_1, R_2)^2 \tag{5.5}$$

and

$$F_s^{max} = \|\vec{F}_n\| \tan\varphi_c + \sigma_{coh} \min(R_1, R_2)^2 \tag{5.6}$$

where $\sigma_{coh}$ is a cohesive strength parameter which controls the adhesion forces in the normal and tangential directions. $\varphi_c$ is the contact friction angle. In this chapter, cohesion is only introduced at sand-carbonate contacts. The parameters of the sand and carbonate particles are indicated in Table 5.1.

Table 5.1: Properties of particles used in the static probing tests.

| Parameter | Symbol | Unit | Sand | Carbonate |
|---|---|---|---|---|
| Density | $\rho$ | kg/m$^3$ | 2650 | 2710 |
| Young's modulus | $E_s$, $E_c$ | GPa | 1 | 1 |
| Shear stiffness coefficient | $\nu$ | - | 0.3 | 0.3 |
| Friction angle | $\varphi_c$ | ° | 30 | 30 |
| Cohesive strength | $\sigma_{coh}$ | GPa | 10 | |

### 5.3.3. STATIC PROBING TEST

#### CALCULATION OF THE SHEAR MODULUS

After the generation of the granular assemblies, a stress relaxation process is applied before the sample is subjected to static probing. The stress relaxation process is applied until the unbalanced force ratio (defined as the ratio between the mean static unbalanced force and the mean contact force) is reduced below $1 \times 10^{-8}$, which ensures a quasi-static state (Gu *et al.*, 2017; Gong *et al.*, 2019; Cheng *et al.*, 2020; Shi *et al.*, 2020). After the stress relaxation process, the probing test is conducted to calculate the shear modulus $G$. In the probing test, small strain increments are applied in the axial direction while the lateral confining stress is maintained constant. $G$ is calculated as:

$$G = \frac{\Delta q}{3\Delta\varepsilon_q} \tag{5.7}$$

where $\Delta q$ is the increment of deviatoric stress and $\Delta\varepsilon_q = \Delta\varepsilon_1 - (\Delta\varepsilon_1 + \Delta\varepsilon_2 + \Delta\varepsilon_3)/3$ is the incremental deviatoric strain, with $\Delta\varepsilon_1$ the incremental axial strain, and $\Delta\varepsilon_2$ and $\Delta\varepsilon_3$, the two lateral strain increments.

#### DETERMINATION OF THE ELASTIC REGIME

The maximum strain level ensuring that the DEM samples remain within the elastic regime must be identified prior to determining the small-strain shear modulus. Therefore, static probing tests are run at different strain levels, and the corresponding shear modulus $G$ is calculated for each strain level. Figure 5.3 presents the evolution of the calculated

$G$ with the strain level. The figure shows that the shear modulus remains approximately constant around $\varepsilon_q = 1\times10^{-6}$, before dropping with a further increase in $\varepsilon_q$. Consequently, $\varepsilon_q = 1\times10^{-6}$ is selected as the reference state for calculating the small-strain shear stiffness $G_0$. This reference value of $\varepsilon_q$ is also proved to be valid in the cases of cemented samples (Figure 5.5).

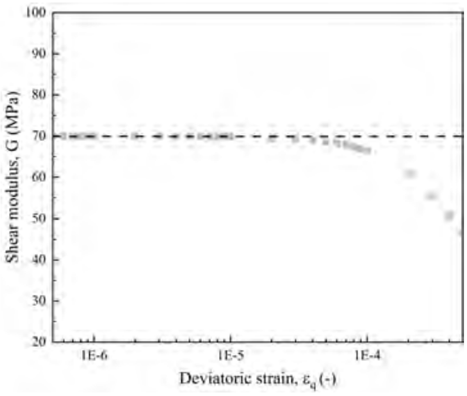

Figure 5.3: Evolution of the shear modulus of the host sand with deviatoric strain.

### 5.3.4. DETERMINATION OF THE REV SIZE

The size of the representative elementary volume (REV) should be determined to ensure the representativeness of the results. Five sample sizes with respectively 750, 1000, 2000, 3500 and 5000 sand particles, following the same particle size distribution, are considered. Six samples are generated randomly for each sample size.

Figure 5.4 shows that, for samples with less than 3500 particles, the sample size affects the average value of the small-strain stiffness, as well as the dispersion of the results. Smaller samples exhibit, on average, a higher small-strain shear modulus than larger samples, and the dispersion of the results is greater for small samples. Consequently, a sample containing 3500 sand particles is selected as the REV and used for the subsequent simulations.

## 5.4. CEMENTED SAMPLES WITH A SINGLE CARBONATE DISTRIBUTION PATTERN

Bio-cemented samples with a single carbonate distribution pattern, i.e. bridging, contact cementing, coating or pore filling, are subjected to static probing under 100 kPa confining pressure. The parameters of the sand and carbonate particles used in this chapter are presented in Table 5.1, unless otherwise stated. The cohesive strength parameter $\sigma_{coh}$ is set to 10 GPa for sand-carbonate contacts, which is high enough to ensure that no bond breakage occurs within the elastic regime. The carbonate content is 1% for the cemented samples unless otherwise stated in Section 5.4.3. Throughout this chapter, the carbonate content is defined as the dry mass of carbonate over the mass of the sand.

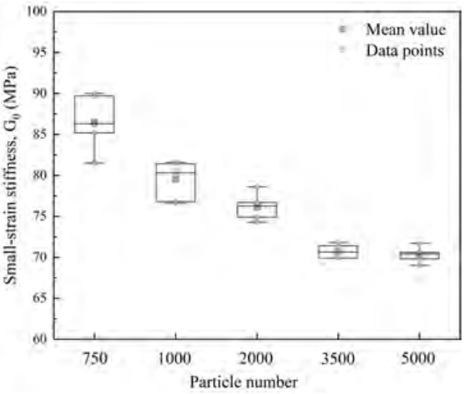

Figure 5.4: Small-strain stiffness of samples with various particle numbers.

### 5.4.1. CARBONATE DISTRIBUTION PATTERN

Figure 5.5 presents the evolution of the shear modulus of cemented samples with different carbonate distribution patterns as a function of the deviatoric strain. For all cemented samples presented in Figure 5.5, the shear modulus stays at a plateau around $\varepsilon_q = 1 \times 10^{-6}$. This suggests that the small-strain stiffness $G_0$ of cemented samples can also be determined at a deviatoric strain $\varepsilon_q = 1 \times 10^{-6}$. For cemented samples with other carbonate contents, a similar evolution of $G$ with $\varepsilon_q$ is observed. Consequently, $\varepsilon_q = 1 \times 10^{-6}$ is also selected as the state for calculating $G_0$ of cemented samples.

Figure 5.5 further shows that the carbonate distribution pattern plays a critical role on $G_0$ of bio-cemented soils. For cemented samples with 1% carbonate content, carbonate particles in the forms of bridging and contact cementing lead to obvious improvement in $G_0$. By contrast, carbonate particles distributed in the form of coating and pore filling show negligible differences compared to the uncemented sample.

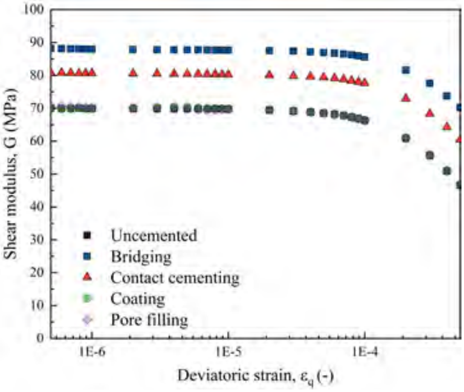

Figure 5.5: Evolution of the shear modulus with deviatoric strain for bio-cemented samples with different carbonate distribution patterns.

### 5.4.2. YOUNG'S MODULUS OF CARBONATE PARTICLES

Calcium carbonate ($CaCO_3$) has three polymorphs: vaterite (hexagonal), aragonite (orthorhombic) and calcite (trigonal). During the treatment process of MICP or EICP, calcium carbonate can precipitate in any of the three polymorphs depending on the pH environment, temperature and the urea-$CaCl_2$ solution concentrations, among others (Clarà Saracho *et al.*, 2020). In addition, metastable hydrated forms, including monohydrocalcite ($CaCO_3 \cdot H_2O$), ikaite ($CaCO_3 \cdot {}_6H_2O$), calcium carbonate hemihydrate ($CaCO_3 \cdot 1/2H_2O$), and amorphous calcium carbonate (ACC) can also exist (Tlili *et al.*, 2002; Zou *et al.*, 2019; Saracho *et al.*, 2021). Their estimated Young's modulus varies in a large range, from 25 GPa to 91.28 GPa (see Table 5.2). By contrast, the Young's modulus of quartz sand is around 97 GPa (Peng & Redfern, 2013).

Table 5.2: Literature review on the estimated Young's modulus of various carbonates and metastable hydrated carbonates. Note that several of the polymorphs are structurally anisotropic, and their elastic property exhibits a directional dependence. The range of the estimated Young's modulus for a given species partially reflects this anisotropy.

| | Young's modulus (GPa) | Source |
|---|---|---|
| Calcite | 77.6 to 96.8 | Chahi *et al.* (2020); Ekprasert *et al.* (2020) |
| Vaterite | 67.2 to 70 | Ekprasert *et al.* (2020) |
| Aragonite | 43 to 75 | Zhang *et al.* (2016) |
| $CaCO_3 \cdot H_2O$ | 65.9 to 71.7 | Chahi *et al.* (2020); Zhou *et al.* (2020) |
| $CaCO_3 \cdot 6H_2O$ | 41.9 to 66 | Chahi *et al.* (2020); Zhou *et al.* (2020) |
| $CaCO_3 \cdot 1/2H_2O$ | 91.3 | Zhou *et al.* (2020) |
| ACC | 25 to 30 | Lee *et al.* (2016) |

To investigate the effect of the elastic properties of the precipitated crystals on the small-strain stiffness of bio-cemented soil, static probing tests are carried out on bio-cemented samples with various ratios of sand and carbonate elastic moduli, $E_s/E_c$. Figure 5.6 illustrates the variation of $G_0$ with $E_s/E_c$, where $E_s/E_c$ ranges from 0.1 to 10 by fixing $E_s$ at 1 GPa while varying $E_c$. The carbonate content is 1% for all the cemented samples herein. The small-strain shear stiffness of the uncemented sample is also included for reference. It can be found from Figure 5.6 that:

1. For all values of $E_s/E_c$, there is always an improvement in $G_0$ in the case of bridging and contact cementing compared to the uncemented sample, even if $E_c$ is lower than $E_s$. This suggests that all crystals, as long as they are in the pattern of bridging or contact cementing, have a positive effect on $G_0$.

2. The benefit of cementation in the bridging and contact cementing pattern decreases with increasing $E_s/E_c$.

3. Crystals in the form of coating and pore filling do not lead to any increase in $G_0$, independently of $E_s/E_c$.

The reason why a lower $E_c$ value leads to a smaller improvement in $G_0$ in the case of bridging and contact cementing is linked to the contact stiffness. According to Eq. 5.3

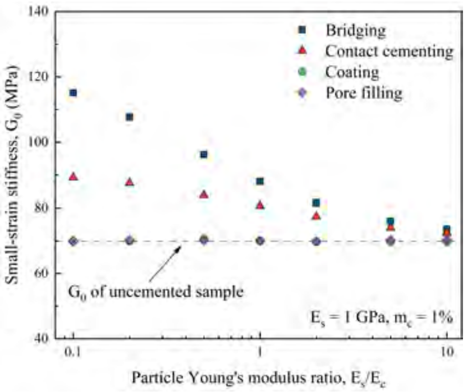

Figure 5.6: Effect of sand-carbonate Young's modulus ratio ($E_s/E_c$) on the small-strain stiffness ($G_0$) of bio-cemented samples.

and 5.4, the stiffness of a sand-crystal contact increases with increasing $E_c$, for a given $E_s$ value. This feature at the contact level is reflected in the macroscopic response of the sample, and the small-strain stiffness $G_0$ for both bridging and contact cementing decreases as $E_s/E_c$ increases.

For a given $E_s/E_c$ ratio, differences in the number of effective bonds explain that bridging cementation leads to higher improvement in $G_0$ than contact cementing, while coating and pore filling exhibit no improvement. Effective bonds refer to crystals which build connections between sand grains. Specifically, bridging holds more effective bonds than contact cementing at 1% of carbonate content, while there are no effective bonds built in the cases of coating and pore filling. This can be supported by the effective coordination number ($Z_e$) proposed by Zhang & Dieudonné (2023b). The effective coordination number describes the average number of effective bonds per sand grain, in which only the contacts that contribute to the overall connections among sand grains are considered. It is defined as:

$$Z_e = \frac{2\left(C_s + C_b\right)}{N_s} \tag{5.8}$$

where $N_s$ is the number of sand particles, $C_s$ is the total number of sand-sand (S-S) contacts and $C_b$ is the number of effective bonds in cemented samples. In the case of bridging, every carbonate connects two sand grains initially. Therefore, $C_b$ is equal to the number of carbonate particles. In the case of contact cementing, several carbonates together strengthen one S-S contact. Therefore, in this case, $C_b$ is equal to the number of S-S contacts which has been cemented. Finally, in the case of coating and pore filling, $C_b$ is equal to zero as carbonate particles do not introduce connections between sand grains. In this way, the different functions of cement particles which are explicitly modelled in cemented soils can be well described, and a detailed discussion on $Z_e$ compared to traditional coordination number and mechanical coordination number can be found in Zhang & Dieudonné (2023b) and Appendix A.

For cemented samples with $m_c$ = 1%, bridging generates the largest $Z_e$ which is 6.99, while the effective coordination number is equal to 5.03 for contact cementing, suggesting a higher improvement in $G_0$ in the case of bridging. The $Z_e$ of samples exhibiting coating and pore filling is 4.3, similar to that of the uncemented sample, corresponding to an absence of improvement in $G_0$ in these two cases.

### 5.4.3. CARBONATE CONTENT

Figure 5.7a presents the evolution of the small-strain shear modulus with increasing carbonate content. Figure 5.7a shows that, for carbonate contents of up to 3%, the small-strain stiffness of the material is not affected by carbonate crystals coating the sand particles or filling the pore space. On the other hand, the bridging and contact cementing type of samples exhibit an obvious improvement in $G_0$ even with a small carbonate content. In addition, the magnitude of improvement in $G_0$ increases with $m_c$ for both bridging and contact cementing, which can be attributed to the increase of the number of effective bonds (as described by $Z_e$) with $m_c$, as shown in Figure 5.7b.

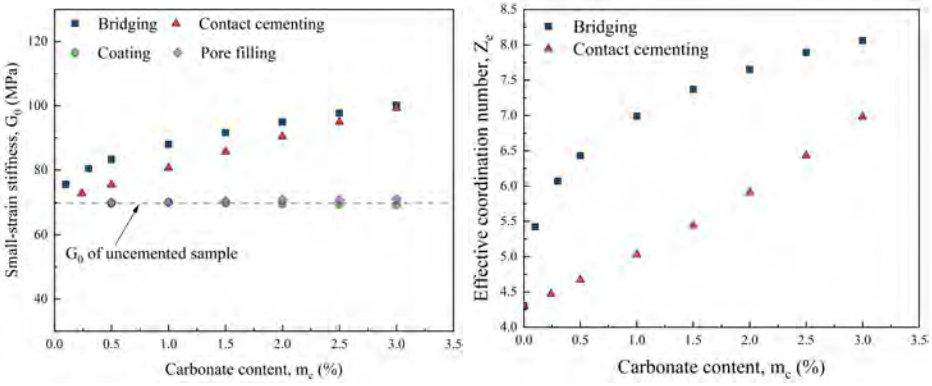

(a) (b)

Figure 5.7: Effect of carbonate content $m_c$ on (a) the small-strain stiffness $G_0$ and (b) the effective coordination number $Z_e$.

It should be noted that bridging always leads to a higher $Z_e$ than contact cementing given the same $m_c$. However, the improvement in $G_0$ resulting from bridging does not always outperform that of contact cementing. For instance, at $m_c = 3\%$, bridging and contact cementing show almost the same improvement in $G_0$, even though bridging generates more effective bonds than contact cementing. This suggests that the overall improvement in $G_0$ is not only related to the number of effective bonds. In fact, it is also related to the ability to improve stiffness from a single effective bond.

To evaluate the contribution of a single effective bond in the form of bridging and contact cementing to the contact stiffness, an axial loading test is carried out on two sand grains cemented with one effective bond in the form of contact cementing and bridging. The case of two sand grains without cementation is also tested as the reference. The axial loading tests and the associated force–displacement relationship are shown in Figure 5.8. It can be seen that the overall stiffness of contact cementing is $8.47\times10^6$ N/m, which reflects the stiffness of the sand–sand contact (which is $4.3\times10^6$ N/m) and the stiffness due to cementation. Accordingly, the net contribution of an effective bond in the contact cementing pattern to stiffness is 4.17×$10^6$ N/m, which is higher than the contribution of one effective bond in the bridging pattern (5.65×$10^5$ N/m).

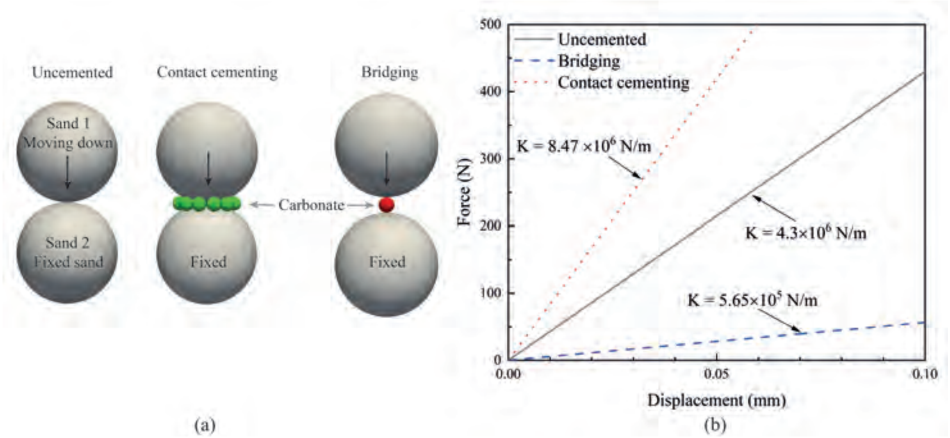

Figure 5.8: Force–displacement response of axial loading tests on two sand grains without cementation and with cementation in the patterns of bridging and contact cementing.

Since one effective bond in the pattern of contact cementing can lead to a higher improvement in stiffness than one in the bridging pattern, at a low carbonate content, it is the number of effective bonds that dominates the improvement in overall stiffness. At this stage, bridging outperforms contact cementing because it shows higher $Z_e$. On the other hand, as the number of effective bonds increases with the increase of carbonate content, $G_0$ increases in both bridging and contact cementing cases, but contact cementing benefits more from the increase of $Z_e$. Therefore, at a high carbonate content, the small-strain stiffness of bridging is almost the same as that of contact cementing even though bridging exhibits higher $Z_e$.

### 5.4.4. HOST SAND PARTICLE SIZE DISTRIBUTION

The three particle size distributions of the host sand sample shown in Figure 5.2 are considered. All particle size distributions have the same mean particle size $D_{50}$ of 8.6 mm, but different coefficients of uniformity $C_u$, namely $C_u = 1$ (monodisperse size distribution), $C_u = 1.4$ and $C_u = 2$. The numerical results show that host sand samples with different $C_u$ values exhibit different $G_0$, namely 89.1 MPa for $C_u = 1$, 69.9 MPa for $C_u = 1.4$ and 27.4 MPa for $C_u = 2$. This is consistent with the results from Iwasaki & Tatsuoka (1977), Wichtmann *et al.* (2009) and Gu *et al.* (2017), which concluded that the small-strain stiffness of sands is not influenced by the mean particle size. It decreases as the coefficient of uniformity of the soil increases. Since host sand samples with different PSDs exhibit different $G_0$ values, a stiffness enhancement factor (SEF) is introduced to describe the magnitude of improvement of $G_0$ on top of the corresponding host sand sample. It is defined as:

$$SEF = \frac{G_0^{cemented} - G_0^{uncemented}}{G_0^{uncemented}} \tag{5.9}$$

The stiffness enhancement factors of cemented samples are compared in Figure 5.9. Only bridging and contact cementing type of cemented samples ($m_c$ = 1%) are included in Figure 5.9, as coating and pore filling type of samples exhibit almost the same $G_0$ as that of corresponding host sand sample. It can be seen from Figure 5.9 that, for a given PSD uniformity, the improvement in $G_0$ increases with the carbonate content for both cases of bridging and contact cementing. In addition, for the same carbonate content, the improvement in $G_0$ increases with $C_u$ in both bridging and contact cementing. The improvement in $G_0$ of bridging exceeds that of contact cementing in cases of $C_u$ = 1 and $C_u$ = 1.4, while this phenomenon is reversed when $C_u$ = 2. This finding suggests that the carbonate distribution pattern which can boost the most small-strain stiffness depends on the PSD uniformity of the soil to be treated.

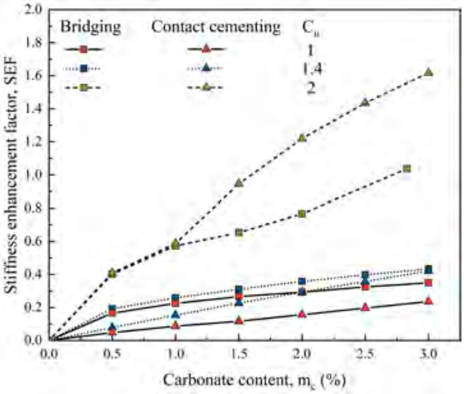

Figure 5.9: Small-strain stiffness enhancement factor (SEF) of cemented samples with different distribution patterns and carbonate contents ($m_c$) generated from host samples with various PSD uniformity ($C_u$).

The reason why the performance of contact cementing is more strongly influenced by the uniformity of the particle size distribution than bridging cases can be attributed to some characteristics of the host sand samples. Two characteristics are considered, namely the number of sand-sand (S-S) contacts (as carbonates are deployed at S-S contacts in contact cementing cases), and the gap size distribution (since carbonates are located at grain gaps for bridging pattern), as illustrated in Figure 5.1. Host samples with the same initial void ratio, particle number and confining pressure show different average numbers of S-S contacts given different PSD uniformity. The change in $C_u$ leads to an obvious change in the number of sand-sand contacts, which can be supported by the coordination number of S-S contacts $Z_{SS}$ (defined as the average number of S-S contacts per sand grain). As shown in Figure 5.10, $Z_{SS}$ is 5.07 for host sand with $C_u$ = 1, 4.3 for host sand with $C_u$ = 1.4 and 2.19 for host sand with $C_u$ = 2, presenting an obvious decreasing trend. This suggests that the number of sand-sand contacts is largely affected by the PSD uniformity and, therefore, the deployment of carbonates in contact cementing pattern. On the other hand, changes in $C_u$ do not result in an obvious difference in the gap size distribution in the range of $C_u$ under consideration, as shown in Figure 5.11. This suggests that the deployment of carbonates in the bridging pattern is not sensitive to the change of $C_u$.

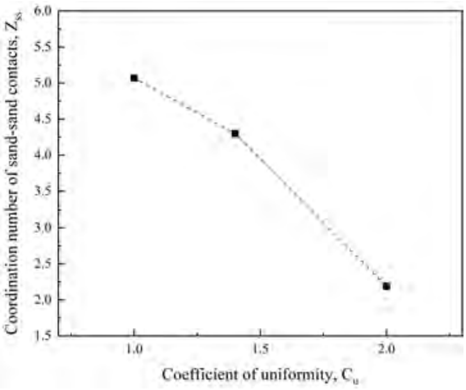

Figure 5.10: Effect of coefficient of uniformity ($C_u$) on the coordination number of sand-sand contacts ($Z_{SS}$).

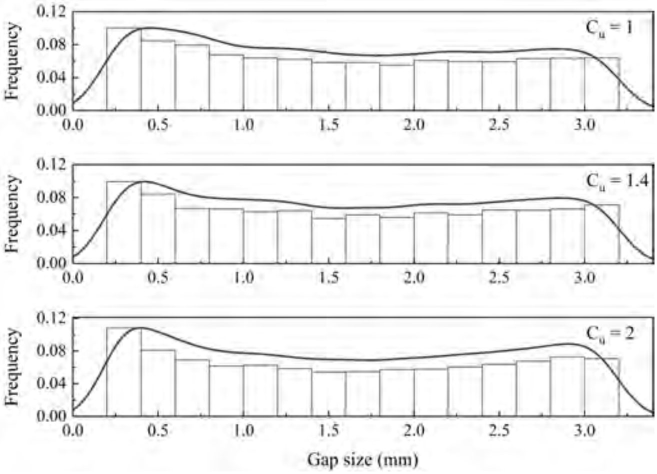

Figure 5.11: Effect of coefficient of uniformity ($C_u$) on the gap size distribution of host sand samples. Bin size is 0.2 mm.

### 5.4.5. HOST SAND VOID RATIO

Figure 5.12a presents the stiffness enhancement factors of cemented samples with $m_c$ = 1% prepared from host sand samples with various void ratios. Only bridging and contact cementing types of samples with a carbonate content of 1% are included in Figure 5.12a. It can be seen that:

1. The stiffness enhancement factor increases with increasing void ratio in both bridging and contact cementing cases. The reason can be attributed to the fact that the host sample holds fewer S–S contacts with an increasing void ratio (i.e. a decreasing trend in $Z_s$ shown in Figure 5.12b). The ratio of the number of effective bonds to the number of S–S contacts increases, as shown in Figure 5.12b, suggesting that the effective bonds are taking the dominating role with the increasing void ratio.

2. Bridging always shows a larger improvement in $G_0$ compared to that of the corresponding contact cementing sample, regardless of the void ratio of the host sand sample. This can be attributed to the fact that, when $m_c$ = 1% (and the number of effective bonds dominates the improvement in stiffness), there are more effective bonds (i.e. higher $Z_e$) in bridging samples compared to contact cementing ones, as presented in Figure 5.12b.

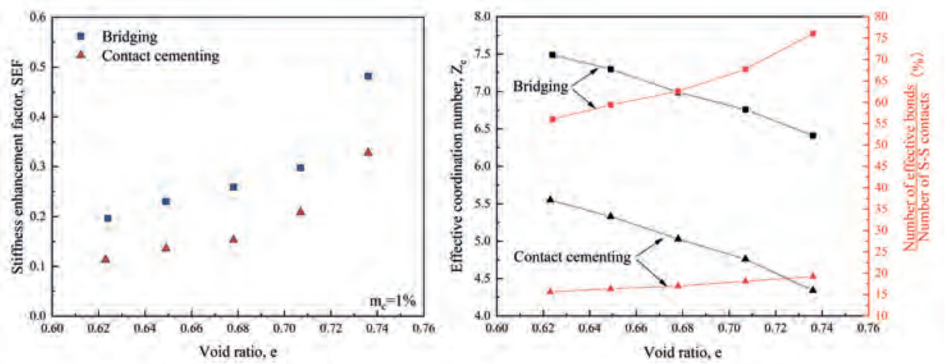

(a)

(b)

Figure 5.12: Effect of initial void ratio of host sand on (a) small-strain stiffness enhancement factor (SEF), (b) $Z_e$ and the ratio of number of effective bonds/ number of S-S contacts.

## 5.5. CEMENTED SAMPLES WITH MIXED CARBONATE DISTRIBUTION PATTERNS

In reality, bio-cemented samples usually exhibit mixed distribution patterns. As discussed in the previous sections, not all precipitated carbonates can contribute to increasing the small-strain stiffness. Carbonates precipitated in the pattern of coating and pore filling hardly contribute to the improvement in $G_0$, and are thus regarded as non-effective precipitation. On the other hand, carbonates distributed in the form of bridging and contact cementing lead to improvement, but with different levels for a given carbonate content. In this section, cemented samples with mixed distribution patterns are generated based on the host sand sample with $C_u = 1.4$ and an initial void ratio of 0.695. The samples are subjected to a static probing test at 100 kPa of confinement. As carbonates precipitated in the pattern of coating and pore filling are non-effective precipitation, three components are considered in mixed distribution patterns: bridging, contact cementing and non-effective precipitation. Note that non-effective precipitation is represented by carbonate in the coating pattern to account for the carbonate mass in that part. Fifteen cemented samples are generated. Each sample has a carbonate content of 2% and has different ratios of the three distribution patterns, as demonstrated by a ternary plot shown in Figure 5.13. In particular, S1-B0C0N1, S11-B1C0N0 and S15-B0C1N0 represent cemented samples with a single carbonate distribution pattern, namely pure coating, bridging and contact cementing, respectively. Sample S5-B1C1N2 contains 2% of carbonate particles, where the mass ratio of carbonates in the pattern of bridging, contact cementing and non-effective (coating) is 1 : 1 : 2.

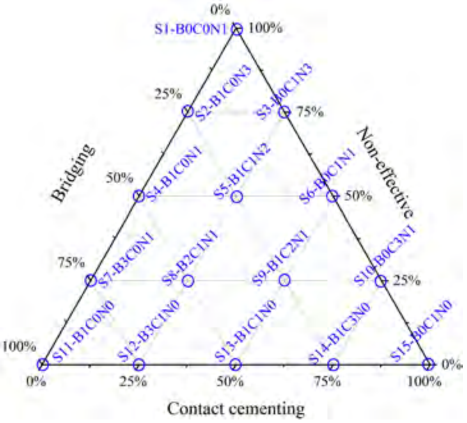

Figure 5.13: Ternary plot illustrating bio-cemented samples with mixed distribution patterns. Sampling points are marked by circles. The name of each sample indicates its ID and mass ratio of carbonates in the pattern of bridging (B) : contact cementing (C) : non-effective (N).

Figure 5.14 presents the stiffness enhancement factor in the same ternary plot as Figure 5.13. It can be seen that, for a given carbonate content of 2%, bio-cemented samples can exhibit different levels of improvement in small-strain stiffness, depending on the relative proportions of carbonates in each distribution pattern. The results show that bio-cemented samples with mixed precipitation in the form of bridging and contact cementing patterns tend to show greater improvement in small-strain stiffness than samples with a unique distribution pattern. In particular, S14-B1C3N0 shows the highest stiffness enhancement factor among all the samples. This results from the balance between the number of bonds (maximised for pure bridging) and the stiffness of individual bonds (highest for contact cementing).

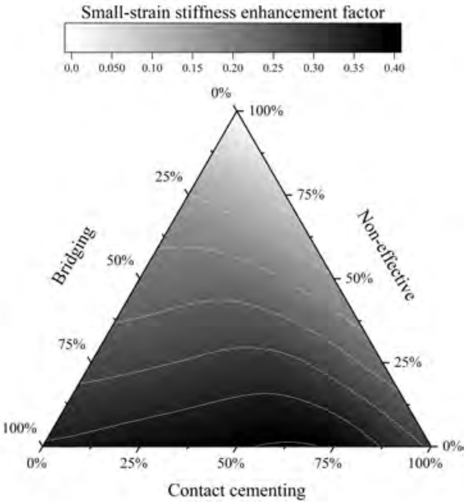

Figure 5.14: Contour of the small-strain stiffness enhancement factor for bio-cemented soils with mixed $CaCO_3$ distribution patterns.

## 5.6. LINKS BETWEEN SMALL-STRAIN STIFFNESS, COORDINATION NUMBER AND VOID RATIO

The small-strain stiffness of granular materials depends on the packing state, which can be characterised by the void ratio $e$ as a macroscopic quantity, and the coordination number $Z$ from a micromechanical perspective. Empirical relationships were established to link the small-strain stiffness $G_0$ to the global void ratio (Hardin & Richart Jr, 1963; Wichtmann *et al.*, 2009; Oztoprak & Bolton, 2013; Senetakis & Madhusudhan, 2015). For example, Hardin & Richart Jr (1963) proposed the empirical relationship:

$$G_0 = AF(e)\sigma'^n \tag{5.10}$$

where $A$ and $n$ are fitting parameters, and $\sigma'$ is the effective confining stress. $F(e)$ is a function of void ratio. Besides empirical relationships, theoretical models, including the effective medium theory (EMT), have been developed to derive $G_0$ from micromechanical features of the granular packing. Chang *et al.* (1991) correlated $G_0$ to $Z/(1+e)$, where $Z$ is the coordination number. Otsubo *et al.* (2022) and Liu *et al.* (2022) found that $G_0$ (or the shear velocity $V_s$) shows a clearer correlation to $Z_m/(1+e_m)$ than $Z/(1+e)$ for bimodal soil mixtures, where $Z_m$ is the mechanical coordination number (Thornton, 2000) and $e_m$ is a proposed mechanical void ratio (see Otsubo *et al.* (2022) for the definition).

The above-mentioned relationships between the small-strain stiffness, the coordination number and the void ratio were proposed for sands and sands containing non-cohesive fines (Gu & Yang, 2013; Otsubo, 2016; Gong *et al.*, 2019; Liu *et al.*, 2022, among others). In this section, attempts are made to link the small-strain stiffness $G_0$ to the coordination number and void ratio of DEM cemented samples (i.e. sands containing cohesive fines). Data from cemented samples (only bridging and contact cementing) with various carbonate contents are used. Figure 5.15(a) presents the relationship between the small-strain stiffness and the void ratio of each sample. It can be seen that $G_0$ decreases with increasing void ratio following a clear linear trend. This is consistent with results from Wichtmann *et al.* (2009); Liu *et al.* (2021, 2022). Figure 5.15(b) presents the coordination number against the void ratio, from which a less clear correlation can be identified. Following German (2014) who found a linear correlation between the coordination number $Z$ and the ratio $1/(1+e)$, attempts are also made to correlate $Z$ with $1/(1+e)$ of DEM cemented samples. A poor linear correlation ($R^2 = 0.449$) is found (the results are not presented).

Following Chang *et al.* (1991), Otsubo *et al.* (2022) and Liu *et al.* (2022), who linked $G_0$ to $Z/(1+e)$ or $Z_m/(1+e_m)$, attempts are made to correlate $G_0$ to $Z/(1+e)$, $Z_m/(1+e_m)$ and $Z_e/(1+e)$ of DEM cemented samples. Figure 5.16 presents the evolution of the small-strain stiffness as a function of $Z/(1+e)$, $Z_m/(1+e_m)$ and $Z_e/(1+e)$, respectively. While a relatively good linear correlation is a priori found between $G_0$ and $Z/(1+e)$, we notice that the evolution of the small-strain stiffness with the ratio $Z/(1+e)$ is relatively different for cemented samples with grain bridging and contact cementing. A similar conclusion can be drawn from Figure 5.16(b), presenting the evolution of the small-strain stiffness with $Z_m/(1+e_m)$. On the other hand, Figure 5.16(c) shows that, while showing a larger dispersion, the small-strain stiffness of cemented samples with grain bridging and contact cementing shows a similar evolution with $Z_e/(1+e)$. In that case, the lower $R^2$ is essentially associated with a wider range of value of $Z_e/(1+e)$ than $Z/(1+e)$. These results support the use of the effective coordination number proposed in Chapter 3 (Zhang & Dieudonné, 2023b) to derive the small-strain stiffness of bio-cemented soils from microstructural features. Further investigation and validation is however necessary.

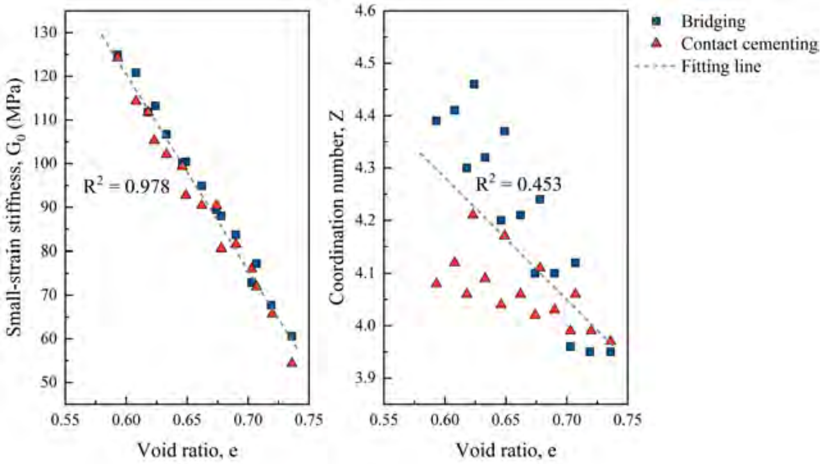

(a) (b)

Figure 5.15: Correlation between the small-strain stiffness $G_0$ and (a) void ratio $e$ and (b) coordination number $Z$.

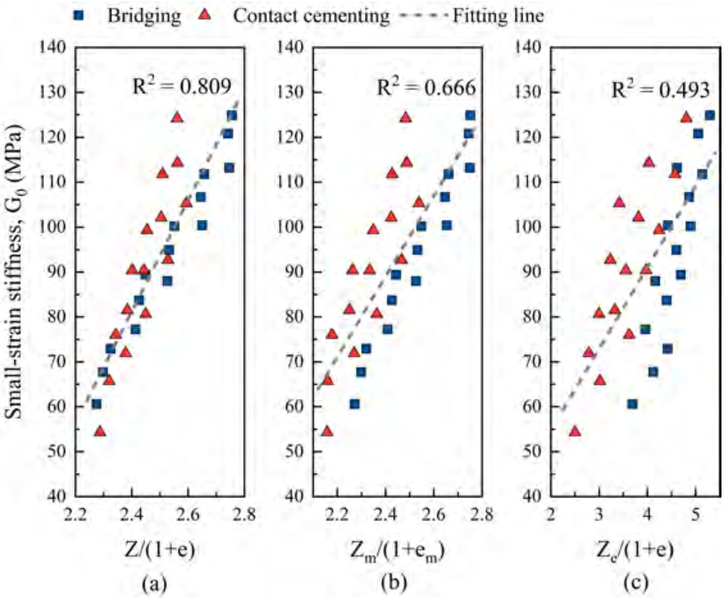

Figure 5.16: Correlation between the small-strain stiffness ($G_0$) and (a) $Z/(1+e)$, (b) $Z_m/(1+e_m)$, (c) $Z_e/(1+e)$.

## 5.7. CORRELATION BETWEEN $G_0$ AND PEAK STRENGTH

To investigate the relationship between the small-strain stiffness and peak strength, 18 cemented samples with different carbonate contents and coefficients of uniformity are selected from samples used in Section 5.4.4 and subjected to drained triaxial compression tests under 100 kPa of confining pressure in DEM. A detailed description of drained triaxial compression simulation can be found in Zhang & Dieudonné (2023b). The contact friction angle $\varphi_c$ used in the triaxial compression simulations is equal to 30°, which is the same as that used for the static probing tests. The cohesive strength parameter $\sigma_{coh}$ for sand-carbonate contacts is set as 10 MPa initially. The peak strength obtained from the triaxial compression tests is plotted against the small-strain stiffness in Figure 5.17. It can be seen that, for cemented samples with bridging and contact cementing, the small-strain stiffness shows a linear relationship with the peak strength for all values of $C_u$ presented in Figure 5.17. This suggests that the small-strain stiffness is a good indicator of soil strength, supporting the approach of using geophysical measurements to monitor and map the strength of treated soils.

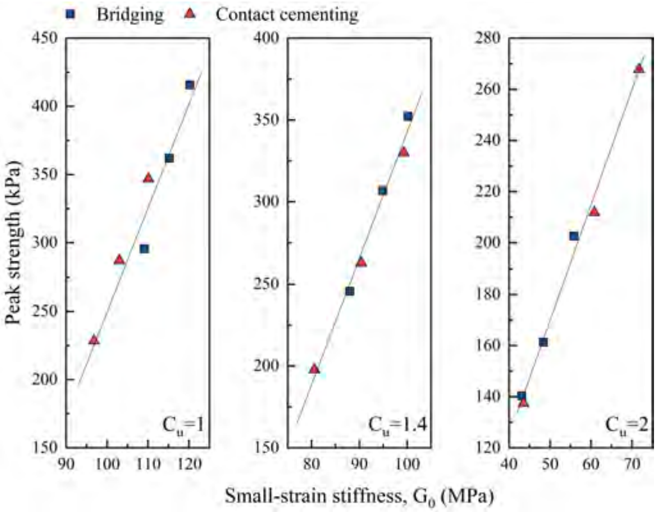

Figure 5.17: Correlation between small-strain stiffness ($G_0$) and peak strength.

## 5.8. DISCUSSION AND CONCLUSIONS

The significant uncertainty associated with bio-mediated treatment poses a central challenge, limiting the practical implementation of such methods. Enhancing confidence in treatment outcomes can be achieved through non-destructive means, such as employing seismic measurement techniques, both in laboratory and field settings. The shear wave velocity can be derived from seismic measurements and used as a key indicator of the treatment effect. This chapter contributes to the fundamental understanding of how bio-cementation affects the small-strain stiffness, hence the shear wave velocity, of bio-cemented sands. Thereby, it aims to support seismic measurement as a means to assess the mechanical efficiency and effectiveness of bio-mediated treatment.

The results of this chapter indicate that the characteristics of bio-cementation affect the improvement in small-strain stiffness $G_0$. The main findings are summarised as follows:

1. The carbonate distribution pattern plays an important role in the effectiveness of bio-cementation. Specifically, coating and pore filling type hardly change $G_0$, hence are regarded as non-effective precipitation from a mechanical point of view. By contrast, bridging and contact cementing emerge as precipitation patterns that lead to significant improvement in $G_0$. Beneficial treatment is associated with effective connections of sand grains (which can be described by the effective coordination number). This finding indicates that seismic methods are useful to assess the performance of the treatment, as compared to carbonate content measurements, which do not provide insight into the microscopic distribution of the minerals.

2. Calcium carbonate crystals precipitated in the form of bridging and contact cementing can lead to an increase in $G_0$, regardless of the relative value of their Young's

modulus with respect to that of the sand grains. On the other hand, crystals with different Young's moduli exhibit different efficiencies in improvement in $G_0$: those with a higher Young's modulus lead to higher improvement in $G_0$. From this perspective, the mechanism that dominates the mechanical efficiency of bio-cementation is the contact stiffness of particle-to-particle contacts. This supports that the measured shear wave velocity or small-strain stiffness can reflect the mechanical efficiency of bio-cementation.

3. The properties of the host sand, specifically the void ratio and coefficient of uniformity of the particle size distribution, affect the improvement in $G_0$ of bio-cemented soils. With varying void ratios and coefficients of uniformity, the number of sand-sand contacts, which provide sites for contact cementing, as well as the gap size distribution, which provides sites for grain bridging, change but with different magnitudes. This leads to different mechanical responses to contact cementing and bridging cementation. In this case, two mechanisms determine together the overall mechanical efficiency of bio-cementation: the number of effective bonds and the ability of a single bond to stiffness improvement.

Overall, the small-strain stiffness of bio-cemented soil is not only related to the characteristics of the precipitated crystals (e.g. polymorph and distribution pattern) but also varies with the host soil. On the one hand, different characteristics of the precipitated crystals contribute differently to the improvement in the small-strain stiffness of bio-cemented soils. On the other hand, different soils respond differently given the same amount and characteristic of the precipitated crystals. This finding extends what has been found in Zhang & Dieudonné (2023b), which reported that the bridging pattern is the optimal distribution pattern as it leads to the most strength improvement. In fact, there is no optimal distribution pattern of carbonate that is universally applicable to all types of soils. Moreover, the small-strain stiffness shows a linear relationship with the peak strength. These findings support that seismic measurement can be used to probe the overall performance of bio-mediated treatment.

# 6

# CONCLUSIONS AND RECOMMENDATIONS

## 6.1. CONCLUSIONS

Microbially induced carbonate precipitation (MICP) and enzyme induced carbonate precipitation (EICP) represent potential alternatives to invasive, carbon-intensive soil stabilisation techniques. While sands treated through bio-cementation methods typically show enhanced strength and stiffness, the magnitude of improvement often varies. The inconsistent mechanical performance of bio-cemented sands hinders the practical application of MICP and EICP, as this variability is not well understood. This PhD thesis contributes to a better understanding of the mechanical behaviour of bio-cemented sands, with a particular focus on elucidating the role of the microstructure on the mechanical performance of the treated material.

In order to characterise the microscopic features of bio-cemented sands, a comprehensive analysis of scanning electron microscope (SEM) images was carried out, with a particular emphasis on the distribution pattern of the precipitated $CaCO_3$ crystals. Four typical $CaCO_3$ distribution patterns were identified and conceptualised: contact cementing, bridging, coating and pore filling. Utilising the discrete element method (DEM), which offers insight into the evolution of particle displacements, rotations and interactions that are usually inaccessible experimentally, DEM was adopted in this thesis to explicitly model bio-cemented sands with various $CaCO_3$ distribution patterns. A toolbox, called Cementor, was developed based on the open-source DEM platform YADE (Šmilauer *et al.*, 2021) to model bio-cemented samples with various characteristics, including different $CaCO_3$ distribution patterns (i.e. either a single type or combinations of the aforementioned distribution patterns) and $CaCO_3$ contents (up to 3% by mass). The numerical samples were then used to evaluate the effects of $CaCO_3$ distribution pattern and $CaCO_3$ content on the mechanical response of bio-cemented sands. The main conclusions of this thesis are summarised in the following sections.

### 6.1.1. MECHANICAL RESPONSE OF BIO-CEMENTED SOILS UNDER TRIAXIAL COMPRESSION

In order to understand how the various $CaCO_3$ distribution patterns affect the mechanical behaviour of bio-cemented sands, numerical samples with a single type of $CaCO_3$ distribution pattern were subjected to drained triaxial compression tests under various confining pressures (Chapter 3). The constitutive behaviour of the DEM samples (both the uncemented sample and the bio-cemented samples) was compared with experimental data for model validation. It was found that the DEM models qualitatively captured the macroscopic responses observed in experiments. Specifically, the evolution of the stress-strain relationship and the volumetric response of the DEM model for the uncemented sample were in agreement with the experimental results in general. In addition, DEM models captured the changes in constitutive behaviour due to the bio-cementation, such as the increase in stiffness, stress and dilatancy, as well as strain hardening and strain softening behaviours, which were also consistent with those observed experimentally. The major findings are:

1. The $CaCO_3$ distribution pattern was found to play an important role in the mechanical response of bio-cemented sands. Specifically, $CaCO_3$ in the forms of bridging and contact cementing can lead to an important increase in strength and stiffness.

On the other hand, carbonates coating grains and filling pores have insignificant to no impact on the material behaviour at contents below 3%.

2. Bio-cemented samples with bridging and contact cementing distribution patterns present different stress-strain behaviours. For the same $CaCO_3$ content, the cemented sample with grain bridging exhibits a larger increase in peak strength than other samples, followed by a sharp decrease after the peak point. By contrast, the sample with contact cementing shows a lower improvement in peak strength than bridging, and the strength decreases gradually after its peak value. This difference is associated with different bond breakage evolutions. In the case of bridging, the maximum bond breakage rate occurs prior to the peak strength and is followed by a sharp decrease. On the other hand, the post-peak behaviour is associated with a gradual decrease of the bond breakage rate in the case of contact cementing, leading to a progressive decrease in the overall strength and a more ductile behaviour as compared to grain bridging.

3. An effective coordination number was proposed, which differentiates the effective and non-effective sand-carbonate contacts. Therefore, it can well describe the contribution of $CaCO_3$ crystals to the overall mechanical improvements considering $CaCO_3$ distribution pattern.

It should be noted that the triaxial compression tests were carried out on numerically bio-cemented samples with carbonate contents ranging from 1% to 3% by mass. In this range of carbonate contents, $CaCO_3$ in the form of grain coating and pore filling exhibit negligible mechanical improvements. However, for higher carbonate contents, the mechanical behaviour of bio-cemented soils with coating and pore filling remains to be revealed. As discussed in Chapter 3, the peak strength of cemented samples with grain coating tends to increase with the carbonate content, although in a limited range. This indicates that an increase in the carbonate content may affect the mechanical behaviour of cemented samples with grain coating. In addition, bio-cemented soil samples with pore filling can be regarded as a binary mixture (sand grains and non-cohesive fines), resembling gap-graded soils (coarse grains and fines). It was found that the mechanical behaviour of binary mixtures and gap-graded soils much depends on the fine content (Dai *et al.*, 2015; Shire *et al.*, 2016; Sufian *et al.*, 2021; Otsubo *et al.*, 2022; Yilmaz *et al.*, 2023, among others), which suggests that the mechanical behaviour of bio-cemented soils with pore filling may evolve with the amount of carbonate content as well. Consequently, the above findings which derived from samples with carbonate content ranging from 1% to 3% may not be applicable for cases with a higher carbonate content.

### 6.1.2. RESIDUAL STRENGTH OF BIO-CEMENTED SOILS

While bio-cemented soils are expected to exhibit strength improvement, some experimental studies have reported a decrease in residual strength. This phenomenon has not been explained nor captured by numerical studies, and is not included in constitutive models. In Chapter 3, grain bridging was found to have a lower residual strength than uncemented samples. Therefore, following Chapter 3, the residual strength of samples with bridging cementation was systematically investigated in Chapter 4 in order to identify the factors that affect the residual strength of cemented soils and explain the reasons why grain bridging can lead to a lower residual strength than uncemented soils.

Results of 3D DEM simulations showed that bio-cemented sand samples with a bridging pattern may exhibit a lower residual strength than the corresponding host sand, depending on the cohesion strength of the sand-carbonate contacts and the relative Young's moduli of the carbonate and sand grains. On the other hand, the carbonate content (in the range of 1% to 3%) and the confining pressure did not affect the difference in residual strengths between cemented and uncemented samples. Specifically, when the cohesion between sand and carbonate particles is null or low, samples with a grain bridging pattern tend to show a lower residual strength than the corresponding uncemented sample. With the increase of sand-carbonate cohesion, the residual strength increases to the same level as the uncemented sample and eventually exceeds it. On the other hand, a low $E_c/E_s$ ratio leads to a minor difference in the residual strength between samples with bridging cementation and uncemented samples. When $E_c$ approaches $E_s$, samples with a bridging pattern show a reduction in the residual strength. This reduction in the residual strength was observed on samples with different carbonate contents and subjected to different confining pressures.

The underlying mechanisms were further investigated through 2D DEM simulations. The results indicated that the introduction of carbonate particles following a bridging pattern, whether they are cohesive or not, modifies the structure of the granular assembly and its stability, thereby affecting the development of strain localisation. Non-cohesive carbonates and low-cohesive carbonates are more likely to lead to a meta-stable structure. This meta-stable structure is prone to relative movement of particles, which in turn leads to the development of shear bands and, overall, a lower residual strength. A stronger cohesive carbonate can compensate for this instability and lead to a more stable microstructure, which contributes to the improvement of the global residual strength. The two mechanisms, namely, the development of shear bands due to grain-scale instability and cohesive bonding, compete with each other and together control the overall residual strength. When the sand-carbonate cohesive strength is low, the weakening effect due to the formation of shear bands is dominant. With the increase of cohesive strength, the contribution from cohesive bonds to residual strength takes the role, which leads to an increase in residual strength.

### 6.1.3. SMALL-STRAIN SHEAR STIFFNESS OF BIO-CEMENTED SOILS

The variation in the microstructure of bio-cemented soils, e.g. $CaCO_3$ distribution pattern, leads to uncertainty of mechanical improvements gained from bio-mediated treatment. It is crucial to develop a probing method to gain certainty on the treatment. The seismic measurement is an essential tool in the geotechnical field. It can provide real-time and non-destructive monitoring of the wave signal of the subsurface, from which the seismic wave velocity can be derived. In this sense, the small-strain stiffness of bio-cemented samples with different micro-scale characteristics was investigated in Chapter 5. The findings can support the analysis of the seismic wave velocity propagating in bio-cemented soils. The major findings are:

1. The small-strain stiffness of bio-cemented sand is largely affected by the $CaCO_3$ distribution pattern. Specifically, $CaCO_3$ in coating and pore filling patterns hardly

contributes to improvement in small-strain stiffness. By contrast, grain bridging and contact cementing lead to obvious improvements in small-strain stiffness.

2. Various $CaCO_3$ polymorphs (vaterite, aragonite and calcite) and meta-stable hydrated forms (e.g. $CaCO_3 \cdot H_2O$, $CaCO_3 \cdot 6H_2O$, etc.) can be found in bio-cemented soils. These crystals exhibit different elastic properties. Numerical results show that all crystals contribute to improvements in small-strain stiffness, regardless of the Young's modulus of the carbonate grains. The higher the Young's modulus of the crystal, the larger the improvements in small-strain stiffness.

3. The effect of bio-cementation depends on the properties of the host sand, among which are the void ratio and coefficient of uniformity of the particle size distribution. With varying void ratio and coefficient of uniformity of the host sand, the number of sand-sand contacts, which provide sites for contact cementing, as well as the gap size distribution, which provides sites for grain bridging, change with different magnitudes, leading to different mechanical responses of samples with contact cementing and grain bridging.

## 6.2. RECOMMENDATIONS FOR FUTURE RESEARCH

This thesis focused on understanding the mechanical behaviour of bio-cemented soils from microscopic observations. The role of the carbonate distribution pattern was emphasised and found to be critical. The findings of this thesis give valuable information for the design and optimisation of an MICP and EICP treatment (see Fig. 1.2). In particular, it is important to privilege the precipitation of carbonates in the patterns of bridging and contact cementing. However, there are also limitations in the presented thesis, which can be improved in future research. They are summarised as follows.

1. Modelling realistic particle shape. The shape of both the sand grains and crystals in the presented DEM samples was simplified as spherical in this thesis. On the one hand, modelling realistic particle shapes enables the reproduction of complex $CaCO_3$ distribution patterns. For instance, $CaCO_3$ connects multiple grains at the same time. This was not covered in this thesis due to the simplified geometry of the grains. On the other hand, various shapes of the precipitated crystals have been observed in MICP and EICP treatments, including rhombohedral-shaped crystals, cubic plate-like crystals and spherical crystals (van Paassen, 2009; Dadda *et al.*, 2017; Mujah *et al.*, 2019; Nafisi *et al.*, 2019; Wang *et al.*, 2019, among others). Different shapes may affect differently on the mechanical response of bio-cemented soils and hence it is better to consider the shape effect. The grain shape can be simulated in DEM using approaches such as clumps (Shi *et al.*, 2020; Dai *et al.*, 2022), Level set DEM (LS-DEM) (Kawamoto *et al.*, 2016, 2018), among others.

2. The DEM parameters used for grain contacts, such as the friction angle, the cohesive strength and the contact area of sand-carbonate contacts with different carbonate morphologies, in the context of bio-cementation are not yet fully available from experiments. Therefore, it is recommended in future work to carry out grain-scale micromechanical tests to provide references for DEM parameters and bridge the gap between DEM simulations and physical studies.

3. A rigid wall boundary condition was used in the triaxial compression simulations. This condition may hinder the formation of shear bands and hence affect the mechanical response. Modelling the soft membrane boundary instead of using the rigid wall boundary can better capture the potential shear bands and facilitate the validation of the DEM model against experimental results (Cheung & O'Sullivan, 2008; Qu *et al.*, 2019).

4. As discussed in Section 6.1, the mechanical behaviour of bio-cemented soils with a higher carbonate content may show a difference compared to that of a bio-cemented soil with a carbonate content below 3%. Therefore, it is worth investigating the mechanical behaviour of bio-cemented soils in a larger range of carbonate content.

Although DEM provides detailed insights into the fundamentals of the mechanical behaviour of bio-cemented soils, it is computationally costly, limiting the application of DEM to large-scale engineering problems. In this sense, the finite element method (FEM) can be used to solve the boundary value problems of engineering applications. This generally requires the definition of constitutive relations. This thesis shows that a constitutive model for bio-cemented soils should consider the microscopic features of bio-cemented soils, including the different mechanical contributions of carbonates precipitated in various patterns (Li *et al.*, 2021). Alternatively, the constitutive relation can be derived directly from DEM simulations, following the FEM-DEM approach (Guo & Zhao, 2014; Nguyen *et al.*, 2014; Shahin *et al.*, 2016; Couture, 2020). This method retains the capability of solving large-scale boundary value problems from FEM and incorporates abundant micro-scale information at the same time by using DEM. Using this method to study engineering problems of bio-cemented soils is also recommended.

# A

# AN EFFECTIVE COORDINATION NUMBER DESCRIBING MICROSTRUCTURES OF BIO-CEMENTED SANDS

## A.1. INTRODUCTION

To highlight the performance of the proposed effective coordination number for describing the mechanical properties of bio-cemented soils. Following Chapter 3, attempts are made in this appendix to use the coordination number and mechanical coordination number to describe the mechanical properties (specifically, stiffness) of bio-cemented samples. Limitations of the two coordination numbers for describing mechanical properties are discussed in detail. Finally, the effective coordination number is used, and its performance in describing the mechanical properties of bio-cemented samples is evaluated.

Fig. A.1 summarizes the stiffness ($E_{50}$) of the DEM samples with various carbonate distribution patterns and contents ($m_c$). It can be seen from Fig. A.1 that bridging and contact cementing type of cemented samples exhibit obvious increases in stiffness, and the improvement is proportional to the carbonate content. In contrast, the stiffnesses of coating and pore filling types of samples are at the same level as that of the uncemented sample, showing a negligible difference.

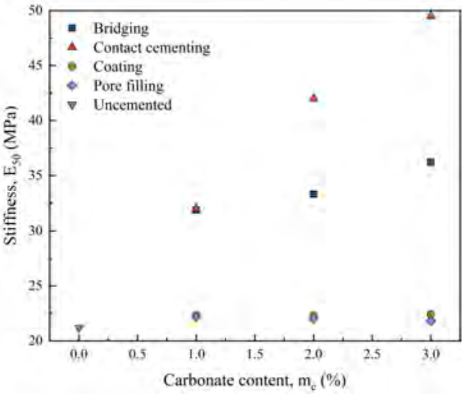

Figure A.1: Correlation of stiffness ($E_{50}$) to carbonate content ($m_c$).

Stiffness is a mechanical parameter describing the elastic property of a granular packing. It is related to the initial structure of the granular packing. In the following sections, attempts have been made to describe the stiffness of the DEM samples by using different types of coordination numbers.

## A.2. COORDINATION NUMBER AND MECHANICAL COORDINATION NUMBER

### A.2.1. COORDINATION NUMBER

Fig. A.2 presents the correlation of initial coordination number (Z) and initial phase-dependent coordination number ($Z^s$, $Z^c$) to stiffness.

1. It can be seen from Fig. A.2a that the increase of Z does not lead to an increase in stiffness. For instance, in the case of bridging, it exhibits obvious improvement in

stiffness, while Z of bridging cases are the same as that of the uncemented sample. In addition, coating and pore filling cases show a reduction in Z compared to the uncemented sample (because carbonates in these two cases do not contribute much to the number of inter-particle contacts but to the number of total particles), while their stiffnesses are roughly consistent with the stiffness of the uncemented sample. This indicates that Z can not reflect the different mechanical improvements from carbonates in different distribution patterns.

2. From Fig. A.2b it can be found that $Z^s$ basically captures the stiffness improvement from the introduction of carbonates in bridging and contact cementing case, as stiffness increases with initial $Z^s$ in bridging and contact cementing type of samples. However, $Z^s$ fails in explaining the behaviour of coating type of samples, as initial $Z^s$ of coating cases varies in a large range, but the stiffness remains almost the same.

3. Fig. A.2c presents stiffness against initial $Z^c$. Indeed, the initial $Z^c$ of bridging, contact cementing, coating and pore filling is equal to 2, 4, 1 and 0, respectively, independent of carbonate content. This is because each carbonate grain initially connects to two sand grains in the bridging case, two sand grains and their two neighbouring carbonate particles, one sand grain in the coating case and zero contact in the pore filling case.

Overall, these findings suggest that the coordination number Z can not describe the mechanical properties of a cemented sample well.

### A.2.2. MECHANICAL COORDINATION NUMBER

Fig. A.3a presents the stiffness against initial $Z_m$. Compared to Z as shown in Fig. A.2a, $Z_m$ keeps almost the same as Z in the cases of bridging and contact cementing. This is due to the low number of particles without contacts or with only one contact in these two types of cemented samples. For pore filling pattern, $Z_m$ shows a better correlation to stiffness than Z, as all carbonates in this type of distribution have no contact initially, and they are counted as $N_0$. Therefore, the initial $Z_m$ of the pore filling type of sample is the same as that of the uncemented sample. By contrast, $Z_m$ of coating samples is much larger than Z of coating cases. This is because each carbonate particle in the coating pattern has only one contact. Hence, the introduction of carbonates in the coating pattern dramatically increases $N_1$ (the number of particles with one contact only), leading to an increase in $Z_m$. The coating type of sample exhibits a larger $Z_m$ than cemented samples with other carbonate distribution patterns. However, it shows a negligible increase in stiffness. This finding suggests that $Z_m$ can not describe the different mechanical improvements from carbonates in different distribution patterns. The same limitation can also be found in $Z_m^s$ and $Z_m^c$, as shown in Fig. A.3b and c respectively.

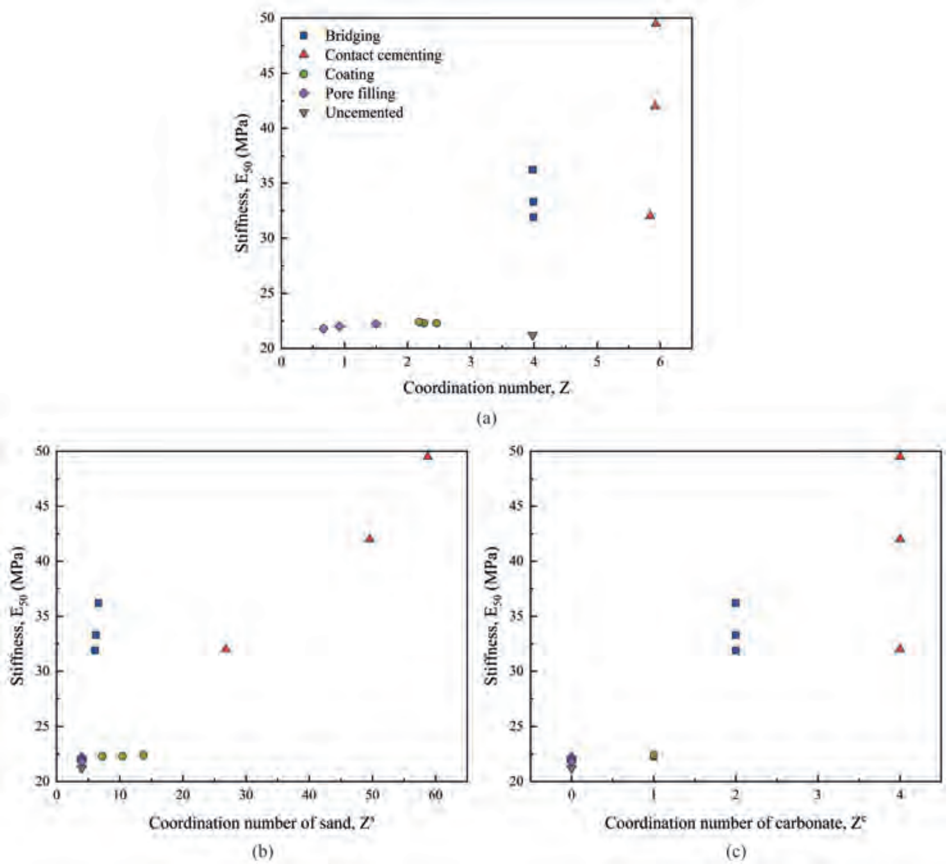

(a)

(b)

(c)

Figure A.2: Correlation of stiffness to initial coordination number for uncemented sample and cemented samples with different distribution patterns and carbonate contents.

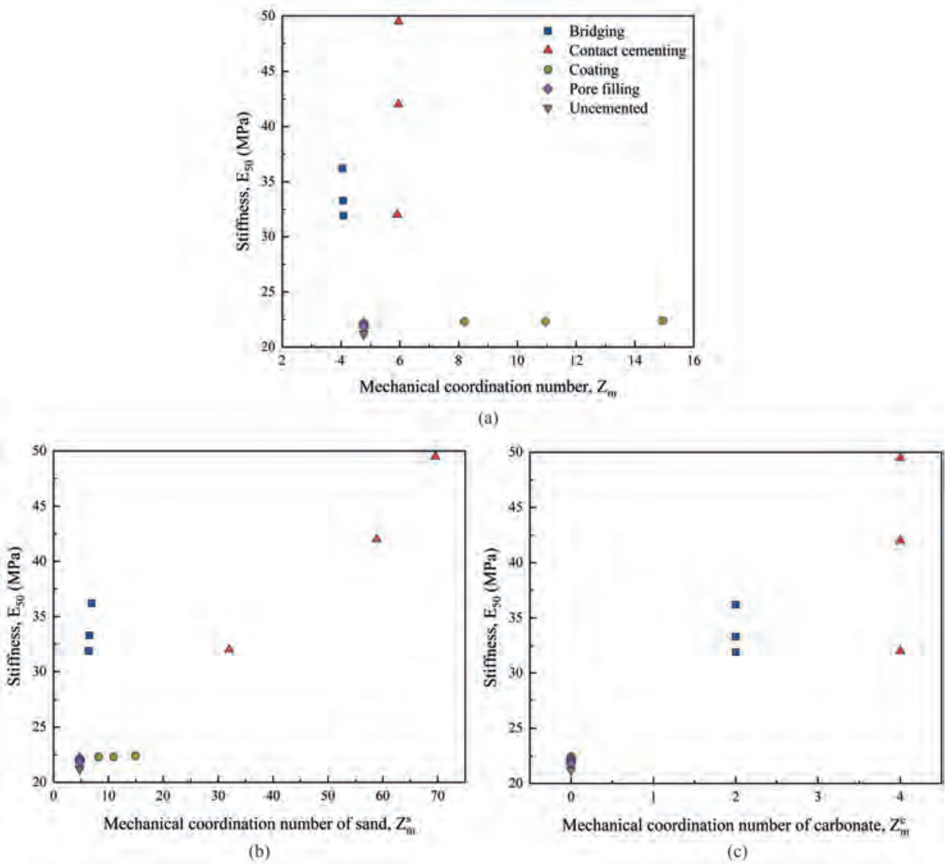

Figure A.3: Correlation of stiffness to initial mechanical coordination number for uncemented sample and cemented samples with different distribution patterns and carbonate contents.

## A.3. EFFECTIVE COORDINATION NUMBER

It can be seen from the above analysis that coordination number and mechanical coordination number have limited capacity to explain the mechanical improvements from the introduced carbonate particles, considering different distribution patterns. Indeed, there is an inconsistency between the change of various coordination numbers and the change in stiffness caused by the introduction of carbonate particles. As addressed in section 3.3.2, this inconsistency comes from the fact that these various coordination numbers (Z, $Z_m$, etc.) are derived based on the number of contacts of every single particle, whereas carbonates with different distribution patterns provide different numbers of contacts. Moreover, carbonates in different distribution patterns have different effects on mechanical improvement, depending on whether they build connections between sand grains and the way they build the connection. For instance, carbonates in the coating pattern lead to an increase in total contact number, but they do not build connections between sand grains and hence hardly result in mechanical improvements. These carbonates are usually characterised as non-effective precipitation from the mechanical point of view. By contrast, carbonates in bridging and contact cementing patterns introduce connections among sand grains and are characterised as effective precipitation.

Fig. A.4 shows the correlation of stiffness to the initial effective coordination number. The effective coordination number of the coating and pore filling type of samples is the same as that of the uncemented sample, and they exhibit approximately equal stiffness, indicating that the effective coordination number can capture the characteristics of those carbonates which do not contribute to mechanical improvement. For samples in bridging and contact cementing type of distribution, $Z_e$ shows a roughly linear relationship with the stiffness, suggesting that the effective coordination number can well describe the mechanical improvements due to the introduction of carbonates.

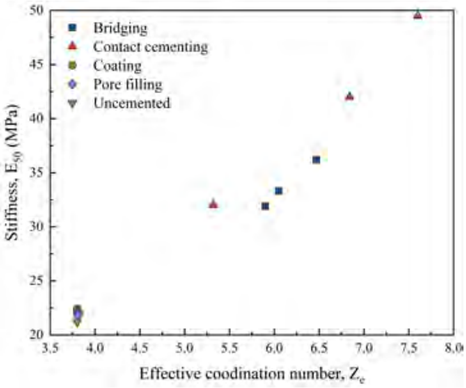

Figure A.4: Correlation of stiffness to initial effective coordination number $Z_e$ for uncemented sample and cemented samples with different distribution patterns and carbonate contents.

## A.4. SUMMARY

Bio-cemented soils exhibit various microstructures, depending on the spatial distribution of the precipitated calcium carbonate crystals with respect to the host granular skeleton. To quantitatively characterise the microstructure accounting for the various carbonate distribution patterns of bio-cemented samples, the widely used microscopic variables, i.e. coordination number and mechanical coordination number, are first adopted to correlate the micro-scale structure to the macro-mechanical response of granular materials. However, limitations are found when using these variables to explain the mechanical improvements from the introduced carbonate particles considering different distribution patterns. For instance, the coordination number $\mathrm{Z}$ and mechanical coordination number $\mathrm{Z_m}$ can not describe the stiffness increase in bridging and contact cementing type of cemented samples, as $\mathrm{Z}$ and $\mathrm{Z_m}$ remain almost constant at different carbonate contents for bridging and contact cementing cases, while the stiffness increases. For coating and pore filling types of cemented samples, their stiffnesses are roughly the same as the uncemented sample. However, they either show an obvious decrease in $\mathrm{Z}$ or increase in $\mathrm{Z_m}$ (coating type of samples). Overall, an inconsistency between the change of various coordination numbers and the change of stiffness can be found. This indicates the importance of considering different mechanical contributions of carbonates in different distribution patterns. Therefore, a new effective coordination number is adopted to account for the various mechanical contributions of different carbonate distribution patterns. The results show that, compared to the coordination number and mechanical coordination number, the effective coordination number can better describe the mechanical performance of bio-cemented soil with various carbonate distribution patterns.

# REFERENCES

Aboul Hosn, R., Sibille, L., Benahmed, N. & Chareyre, B. (2017). Discrete numerical modeling of loose soil with spherical particles and interparticle rolling friction. *Granular Matter* **19**, No. 1, 1–12.

Ahenkorah, I., Rahman, M., Karim, M. & Teasdale, P. (2020). A comparison of mechanical responses for microbial-and enzyme-induced cemented sand. *Géotechnique Letters* **10**, No. 4, 559–567.

Al Qabany, A. & Soga, K. (2013). Effect of chemical treatment used in MICP on engineering properties of cemented soils. *Géotechnique* **63**, No. 4, 331–339.

Al Qabany, A., Soga, K. & Santamarina, C. (2012). Factors affecting efficiency of microbially induced calcite precipitation. *Journal of Geotechnical and Geoenvironmental Engineering* **138**, No. 8, 992–1001.

Almajed, A., Tirkolaei, H. K., Kavazanjian, E. & Hamdan, N. (2019). Enzyme induced biocementated sand with high strength at low carbonate content. *Scientific Reports* **9**, No. 1, 1135.

Bourrier, F., Kneib, F., Chareyre, B. & Fourcaud, T. (2013). Discrete modeling of granular soils reinforcement by plant roots. *Ecological Engineering* **61**, No. 1, 646–657.

Brugada, J., Cheng, Y., Soga, K. & Santamarina, J. (2010). Discrete element modelling of geomechanical behaviour of methane hydrate soils with pore-filling hydrate distribution. *Granular Matter* **12**, No. 5, 517–525.

Catalano, E., Chareyre, B. & Barthélemy, E. (2014). Pore-scale modeling of fluid-particles interaction and emerging poromechanical effects. *International Journal for Numerical and Analytical Methods in Geomechanics* **38**, No. 1, 51–71.

Chahi, G., Bradai, D. & Belabbas, I. (2020). Structural and elastic properties of caco3 hydrated phases: A dispersion-corrected density functional theory study. *Journal of Physics and Chemistry of Solids* **138**, 109295.

Chang, C. S., Misra, A. & Sundaram, S. S. (1991). Properties of granular packings under low amplitude cyclic loading. *Soil Dynamics and Earthquake Engineering* **10**, No. 4, 201–211.

Chen, X., Guo, H. & Cheng, X. (2017). Heavy metal immobilisation and particle cementation of tailings by biomineralisation. *Environmental Geotechnics* **5**, No. 2, 107–113.

Cheng, H., Luding, S., Saitoh, K. & Magnanimo, V. (2020). Elastic wave propagation in dry granular media: effects of probing characteristics and stress history. *International Journal of Solids and Structures* **187**, 85–99.

Cheng, L., Cord-Ruwisch, R. & Shahin, M. A. (2013). Cementation of sand soil by microbially induced calcite precipitation at various degrees of saturation. *Canadian Geotechnical Journal* **50**, No. 1, 81–90.

Cheng, L., Shahin, M. A. & Chu, J. (2019). Soil bio-cementation using a new one-phase low-pH injection method. *Acta Geotechnica* **14**, No. 3, 615–626.

Cheng, L., Shahin, M. A. & Mujah, D. (2016). Influence of key environmental conditions on microbially induced cementation for soil stabilization. *Journal of Geotechnical and Geoenvironmental Engineering* **143**, No. 1, 04016083.

Cheung, G. & O'Sullivan, C. (2008). Effective simulation of flexible lateral boundaries in two-and three-dimensional DEM simulations. *Particuology* **6**, No. 6, 483–500.

Chu, J., Ivanov, V., Naeimi, M., Stabnikov, V. & Liu, H.-L. (2014). Optimization of calcium-based bioclogging and biocementation of sand. *Acta Geotechnica* **9**, No. 2, 277–285.

Clarà Saracho, A., Haigh, S. K. & Ehsan Jorat, M. (2021). Flume study on the effects of microbial induced calcium carbonate precipitation (MICP) on the erosional behaviour of fine sand. *Géotechnique* **71**, No. 12, 1135–1149.

Clarà Saracho, A., Haigh, S. K., Hata, T., Soga, K., Farsang, S., Redfern, S. A. & Marek, E. (2020). Characterisation of caco3 phases during strain-specific ureolytic precipitation. *Scientific Reports* **10**, No. 1, 1–12.

Couture, C.-B. (2020). *Mechanical characterization of porous sandstones in true triaxial conditions: diffuse and localized deformation, effect of anisotropy*. Ph.D. thesis, Université Grenoble Alpes.

Cui, M.-J., Lai, H.-J., Hoang, T. & Chu, J. (2021). One-phase-low-pH enzyme induced carbonate precipitation (EICP) method for soil improvement. *Acta Geotechnica* **16**, 481–489.

Cui, M.-J., Zheng, J.-J., Zhang, R.-J., Lai, H.-J. & Zhang, J. (2017). Influence of cementation level on the strength behaviour of bio-cemented sand. *Acta Geotechnica* **12**, No. 5, 971–986.

Cundall, P. A. & Strack, O. D. (1979). A discrete numerical model for granular assemblies. *Géotechnique* **29**, No. 1, 47–65.

Da Cruz, F., Emam, S., Prochnow, M., Roux, J.-N. & Chevoir, F. (2005). Rheophysics of dense granular materials: Discrete simulation of plane shear flows. *Physical Review E* **72**, No. 2, 021309.

Dadda, A., Geindreau, C., Emeriault, F., Du Roscoat, S. R., Garandet, A., Sapin, L. & Filet, A. E. (2017). Characterization of microstructural and physical properties changes in biocemented sand using 3D X-ray microtomography. *Acta Geotechnica* **12**, No. 5, 955–970.

Dai, B., Yang, J. & Luo, X. (2015). A numerical analysis of the shear behavior of granular soil with fines. *Particuology* **21**, 160–172.

Dai, B.-B., Li, T.-Q., Deng, L.-J., Yang, J. & Yuan, W.-H. (2022). Fabric effect on the angle of repose in granular materials. *Powder Technology* **400**, 117256.

Darby, K. M., Hernandez, G. L., DeJong, J. T., Boulanger, R. W., Gomez, M. G. & Wilson, D. W. (2019). Centrifuge model testing of liquefaction mitigation via microbially induced calcite precipitation. *Journal of Geotechnical and Geoenvironmental Engineering* **145**, No. 10, 04019084.

de Frias Lopez, R., Silfwerbrand, J., Jelagin, D. & Birgisson, B. (2016). Force transmission and soil fabric of binary granular mixtures. *Géotechnique* **66**, No. 7, 578–583.

DeJong, J., Soga, K., Kavazanjian, E., Burns, S., van Paassen, L. A., Al Qabany, A., Aydilek, A., Bang, S., Burbank, M., Caslake, L. F. *et al.* (2013). Biogeochemical processes and geotechnical applications: progress, opportunities and challenges. *Géotechnique* **63**, No. 4, 287–301.

DeJong, J. T., Fritzges, M. B. & Nüsslein, K. (2006). Microbially induced cementation to control sand response to undrained shear. *Journal of Geotechnical and Geoenvironmental Engineering* **132**, No. 11, 1381–1392.

DeJong, J. T., Mortensen, B. M., Martinez, B. C. & Nelson, D. C. (2010). Bio-mediated soil improvement. *Ecological Engineering* **36**, No. 2, 197–210.

Dhami, N. K., Reddy, M. S. & Mukherjee, A. (2013). Biomineralization of calcium carbonate polymorphs by the bacterial strains isolated from calcareous sites. *Journal of Microbiology and Biotechnology* **23**, No. 5, 707–714.

Ding, Y., Qian, A., Lu, H., Li, Y. & Zhang, Y. (2022). DEM investigation of the effect of hydrate morphology on the mechanical properties of hydrate-bearing sands. *Computers and Geotechnics* **143**, 104603.

Drugan, W. J. & Willis, J. R. (1996). A micromechanics-based nonlocal constitutive equation and estimates of representative volume element size for elastic composites. *Journal of the Mechanics and Physics of Solids* **44**, No. 4, 497–524.

Ekprasert, J., Fongkaew, I., Chainakun, P., Kamngam, R. & Boonsuan, W. (2020). Investigating mechanical properties and biocement application of caco3 precipitated by a newly-isolated Lysinibacillus sp. WH using artificial neural networks. *Scientific Reports* **10**, No. 1, 1–13.

Evans, T., Khoubani, A. & Montoya, B. (2014). Simulating mechanical response in biocemented sands. In *Computer Methods and Recent Advances in Geomechanics: Proceedings of the 14th International Conference of International Association for Computer Methods and Recent Advances in Geomechanics*, Taylor & Francis Books Ltd, pp. 1569–1574.

Feng, K. & Montoya, B. (2015). Influence of confinement and cementation level on the behavior of microbial-induced calcite precipitated sands under monotonic drained loading. *Journal of Geotechnical and Geoenvironmental Engineering* **142**, No. 1, 04015057.

Feng, K., Montoya, B. & Evans, T. (2017). Discrete element method simulations of biocemented sands. *Computers and Geotechnics* **85**, 139–150.

Gai, X. & Sánchez, M. (2019). An elastoplastic mechanical constitutive model for microbially mediated cemented soils. *Acta Geotechnica* **14**, No. 3, 709–726.

Gao, Y., Hang, L., He, J. & Chu, J. (2019). Mechanical behaviour of biocemented sands at various treatment levels and relative densities. *Acta Geotechnica* **14**, No. 3, 697–707.

Gao, Z. & Zhao, J. (2012). Constitutive modeling of artificially cemented sand by considering fabric anisotropy. *Computers and Geotechnics* **41**, 57–69.

German, R. M. (2014). Coordination number changes during powder densification. *Powder Technology* **253**, 368–376.

Gong, J., Wang, X., Li, L. & Nie, Z. (2019). DEM study of the effect of fines content on the small-strain stiffness of gap-graded soils. *Computers and Geotechnics* **112**, 35–40.

Gu, X., Lu, L. & Qian, J. (2017). Discrete element modeling of the effect of particle size distribution on the small strain stiffness of granular soils. *Particuology* **32**, 21–29.

Gu, X. & Yang, J. (2013). A discrete element analysis of elastic properties of granular materials. *Granular Matter* **15**, No. 2, 139–147.

Gu, X., Yang, J. & Huang, M. (2013). DEM simulations of the small strain stiffness of granular soils: effect of stress ratio. *Granular Matter* **15**, No. 3, 287–298.

Gu, X. & Yang, S. (2018). Why the OCR may reduce the small strain shear stiffness of granular materials? *Acta Geotechnica* **13**, No. 6, 1467–1472.

Guo, N. & Zhao, J. (2013). The signature of shear-induced anisotropy in granular media. *Computers and Geotechnics* **47**, 1–15.

Guo, N. & Zhao, J. (2014). A coupled FEM/DEM approach for hierarchical multiscale modelling of granular media. *International Journal for Numerical Methods in Engineering* **99**, No. 11, 789–818.

Guo, N. & Zhao, J. (2016). 3D multiscale modeling of strain localization in granular media. *Computers and Geotechnics* **80**, 360–372.

Hamdan, N. & Kavazanjian Jr, E. (2016). Enzyme-induced carbonate mineral precipitation for fugitive dust control. *Géotechnique* **66**, No. 7, 546–555.

Han, Z., Cheng, X. & Ma, Q. (2016). An experimental study on dynamic response for MICP strengthening liquefiable sands. *Earthquake Engineering and Engineering Vibration* **15**, No. 4, 673–679.

Hardin, B. O. & Richart Jr, F. (1963). Elastic wave velocities in granular soils. *Journal of the Soil Mechanics and Foundations Division* **89**, No. 1, 33–65.

He, J., Chu, J., Gao, Y. & Liu, H. (2019). Research advances and challenges in biogeotechnologies. *Geotechnical Research* **6**, No. 2, 144–155.

Hoang, T., Alleman, J., Cetin, B., Ikuma, K. & Choi, S.-G. (2018). Sand and silty-sand soil stabilization using bacterial enzyme–induced calcite precipitation (BEICP). *Canadian Geotechnical Journal* **56**, No. 6, 808–822.

Ivanov, V. & Chu, J. (2008). Applications of microorganisms to geotechnical engineering for bioclogging and biocementation of soil in situ. *Reviews in Environmental Science and Bio/Technology* **7**, No. 2, 139–153.

Iwasaki, T. & Tatsuoka, F. (1977). Effects of grain size and grading on dynamic shear moduli of sands. *Soils and Foundations* **17**, No. 3, 19–35.

Jiang, M., Liu, F. & Zhou, Y. (2014). A bond failure criterion for DEM simulations of cemented geomaterials considering variable bond thickness. *International Journal for Numerical and Analytical Methods in Geomechanics* **38**, No. 18, 1871–1897.

Jiang, M., Zhang, A. & Li, T. (2019). Distinct element analysis of the microstructure evolution in granular soils under cyclic loading. *Granular Matter* **21**, No. 2, 1–16.

Jiang, M., Zhang, W., Sun, Y. & Utili, S. (2013). An investigation on loose cemented granular materials via DEM analyses. *Granular Matter* **15**, No. 1, 65–84.

Jiang, N.-J. & Soga, K. (2017). The applicability of microbially induced calcite precipitation (MICP) for internal erosion control in gravel–sand mixtures. *Géotechnique* **67**, No. 1, 42–55.

Jonkers, H. M., Thijssen, A., Muyzer, G., Copuroglu, O. & Schlangen, E. (2010). Application of bacteria as self-healing agent for the development of sustainable concrete. *Ecological Engineering* **36**, No. 2, 230–235.

Kawamoto, R., Andò, E., Viggiani, G. & Andrade, J. E. (2016). Level set discrete element method for three-dimensional computations with triaxial case study. *Journal of the Mechanics and Physics of Solids* **91**, 1–13.

Kawamoto, R., Andò, E., Viggiani, G. & Andrade, J. E. (2018). All you need is shape: Predicting shear banding in sand with LS-DEM. *Journal of the Mechanics and Physics of Solids* **111**, 375–392.

Khoubani, A. (2018). *A new bonding model for the particulate simulation of bio-cemented sand (with a side excursion on percolation in granular mixtures)*. Ph.D. thesis, Oregon State University.

Konstantinou, C., Biscontin, G., Jiang, N.-J. & Soga, K. (2021). Application of microbially induced carbonate precipitation to form bio-cemented artificial sandstone. *Journal of Rock Mechanics and Geotechnical Engineering* **13**, No. 3, 579–592.

Krishnan, V., Khodadadi Tirkolaei, H., Martin, K., Hamdan, N., van Paassen, L. A. & Kavazanjian Jr, E. (2021). Variability in the Unconfined Compressive Strength of EICP-Treated “Standard” Sand. *Journal of Geotechnical and Geoenvironmental Engineering* **147**, No. 4, 06021001.

Kuhn, M. R. & Bagi, K. (2009). Specimen size effect in discrete element simulations of granular assemblies. *Journal of Engineering Mechanics* **135**, No. 6, 485–492.

Kumar, A., Song, H.-W., Mishra, S., Zhang, W., Zhang, Y.-L., Zhang, Q.-R. & Yu, Z.-G. (2023). Application of microbial-induced carbonate precipitation (MICP) techniques to remove heavy metal in the natural environment: A critical review. *Chemosphere* , 137894.

Lee, M., Gomez, M. G., San Pablo, A. C., Kolbus, C. M., Graddy, C. M., DeJong, J. T. & Nelson, D. C. (2019). Investigating ammonium by-product removal for ureolytic bio-cementation using meter-scale experiments. *Scientific Reports* **9**, No. 1, 1–15.

Lee, S.-W., Kim, Y.-J., Lee, Y.-H., Guim, H. & Han, S. M. (2016). Behavior and characteristics of amorphous calcium carbonate and calcite using CaCO3 film synthesis. *Materials & Design* **112**, 367–373.

Li, L., Zhang, A. & Dieudonné, A.-C. (2021). Constitutive modelling of bio-cemented soils: effect of cement spatial distribution. *ALERT Geomaterials* , 68.

Li, M., Cheng, X. & Guo, H. (2013). Heavy metal removal by biomineralization of urease producing bacteria isolated from soil. *International Biodeterioration & Biodegradation* **76**, 81–85.

Li, M., Cheng, X., Guo, H. & Yang, Z. (2016). Biomineralization of carbonate by terrabacter tumescens for heavy metal removal and biogrouting applications. *Journal of Environmental Engineering* **142**, No. 9, C4015005.

Li, Z., Wang, Y., Ma, C. & Mok, C. (2017). Experimental characterization and 3D DEM simulation of bond breakages in artificially cemented sands with different bond strengths when subjected to triaxial shearing. *Acta Geotechnica* **12**, No. 5, 987–1002.

Lin, H., Suleiman, M. T., Brown, D. G. & Kavazanjian Jr, E. (2016). Mechanical behavior of sands treated by microbially induced carbonate precipitation. *Journal of Geotechnical and Geoenvironmental Engineering* **142**, No. 2, 04015066.

Liu, B., Zhu, C., Tang, C.-S., Xie, Y.-H., Yin, L.-Y., Cheng, Q. & Shi, B. (2020). Bio-remediation of desiccation cracking in clayey soils through microbially induced calcite precipitation (MICP). *Engineering Geology* **264**, 105389.

Liu, D., Morimoto, T., Carraro, J. A. H. & O'Sullivan, C. (2022). A semi-empirical re-evaluation of the influence of state on elastic stiffness in granular materials. *Granular Matter* **24**, No. 2, 56.

Liu, L., Liu, H., Stuedlein, A. W., Evans, T. M. & Xiao, Y. (2019). Strength, stiffness, and microstructure characteristics of biocemented calcareous sand. *Canadian Geotechnical Journal* **56**, No. 10, 1502–1513.

Liu, X., Zou, D., Liu, J. & Zheng, B. (2021). Predicting the small strain shear modulus of coarse-grained soils. *Soil Dynamics and Earthquake Engineering* **141**, 106468.

Liu, Y., Ali, A., Su, J.-F., Li, K., Hu, R.-Z. & Wang, Z. (2023). Microbial-induced calcium carbonate precipitation: influencing factors, nucleation pathways, and application in waste water remediation. *Science of The Total Environment* **860**, 160439.

Ma, G., Xiao, Y., Fan, W., Chu, J. & Liu, H. (2022). Mechanical properties of biocement formed by microbially induced carbonate precipitation. *Acta Geotechnica* , 1–15.

Magnanimo, V., La Ragione, L., Jenkins, J. T., Wang, P. & Makse, H. A. (2008). Characterizing the shear and bulk moduli of an idealized granular material. *EPL (Europhysics Letters)* **81**, No. 3, 34006.

Mahawish, A., Bouazza, A. & Gates, W. P. (2018). Improvement of coarse sand engineering properties by microbially induced calcite precipitation. *Geomicrobiology Journal* **35**, No. 10, 887–897.

Mitchell, J. K. & Santamarina, J. C. (2005). Biological considerations in geotechnical engineering. *Journal of Geotechnical and Geoenvironmental Engineering* **131**, No. 10, 1222–1233.

Montoya, B. & Dejong, J. (2013). Healing of biologically induced cemented sands. *Géotechnique Letters* **3**, No. 3, 147–151.

Montoya, B. & DeJong, J. (2015). Stress-strain behavior of sands cemented by microbially induced calcite precipitation. *Journal of Geotechnical and Geoenvironmental Engineering* **141**, No. 6, 04015019.

Montoya, B. & Feng, K. (2015). Deformation of microbial induced calcite bonded sands: a micro-scale investigation. In *Deformation Characteristics of Geomaterials*, IOS Press, pp. 978–985.

Montoya, B. M., Do, J. & Gabr, M. A. (2021). Distribution and properties of microbially induced carbonate precipitation in underwater sand bed. *Journal of Geotechnical and Geoenvironmental Engineering* **147**, No. 10, 04021098.

Mujah, D., Cheng, L. & Shahin, M. A. (2019). Microstructural and geomechanical study on biocemented sand for optimization of MICP process. *Journal of Materials in Civil Engineering* **31**, No. 4, 04019025.

Mujah, D., Shahin, M. A. & Cheng, L. (2017). State-of-the-art review of biocementation by microbially induced calcite precipitation (MICP) for soil stabilization. *Geomicrobiology Journal* **34**, No. 6, 524–537.

Nafisi, A., Liu, Q. & Montoya, B. M. (2021). Effect of stress path on the shear response of bio-cemented sands. *Acta Geotechnica* , 1–13.

Nafisi, A., Montoya, B. M. & Evans, T. M. (2020). Shear strength envelopes of biocemented sands with varying particle size and cementation level. *Journal of Geotechnical and Geoenvironmental Engineering* **146**, No. 3, 04020002.

Nafisi, A., Safavizadeh, S. & Montoya, B. M. (2019). Influence of microbe and enzyme-induced treatments on cemented sand shear response. *Journal of Geotechnical and Geoenvironmental Engineering* **145**, No. 9, 06019008.

Nguyen, T. K., Combe, G., Caillerie, D. & Desrues, J. (2014). FEM× DEM modelling of cohesive granular materials: numerical homogenisation and multi-scale simulations. *Acta Geophysica* **62**, 1109–1126.

Nie, J.-Y., Shi, X.-S., Cui, Y.-F. & Yang, Z.-Y. (2022). Numerical evaluation of particle shape effect on small strain properties of granular soils. *Engineering Geology* **303**, 106652.

Okwadha, G. D. & Li, J. (2010). Optimum conditions for microbial carbonate precipitation. *Chemosphere* **81**, No. 9, 1143–1148.

O'Sullivan, C. (2011). *Particulate discrete element modelling: a geomechanics perspective*. CRC Press.

Otsubo, M. (2016). *Particle scale analysis of soil stiffness and elastic wave propagation*. Ph.D. thesis, Imperial College London London, UK.

Otsubo, M., Kuwano, R., O'Sullivan, C. & Shire, T. (2022). Using geophysical data to quantify stress transmission in gap-graded granular materials. *Géotechnique* **72**, No. 7, 565–582.

Oztoprak, S. & Bolton, M. (2013). Stiffness of sands through a laboratory test database. *Géotechnique* **63**, No. 1, 54–70.

Peng, Z. & Redfern, S. A. (2013). Mechanical properties of quartz at the $\alpha$-$\beta$ phase transition: Implications for tectonic and seismic anomalies. *Geochemistry, Geophysics, Geosystems* **14**, No. 1, 18–28.

Perez, J. L., Kwok, C. & Senetakis, K. (2016). Effect of rubber size on the behaviour of sand-rubber mixtures: A numerical investigation. *Computers and Geotechnics* **80**, 199–214.

Phillips, A. J., Gerlach, R., Lauchnor, E., Mitchell, A. C., Cunningham, A. B. & Spangler, L. (2013). Engineered applications of ureolytic biomineralization: a review. *Biofouling* **29**, No. 6, 715–733.

Qu, T., Feng, Y., Wang, Y. & Wang, M. (2019). Discrete element modelling of flexible membrane boundaries for triaxial tests. *Computers and Geotechnics* **115**, 103154.

Rahimi, M., Chan, D. & Nouri, A. (2016). Bounding surface constitutive model for cemented sand under monotonic loading. *International Journal of Geomechanics* **16**, No. 2, 04015049.

Rakhimzhanova, A. K., Thornton, C., Minh, N. H., Fok, S. C. & Zhao, Y. (2019). Numerical simulations of triaxial compression tests of cemented sandstone. *Computers and Geotechnics* **113**, 103068.

Reddy, N. S., He, H. & Senetakis, K. (2022). DEM analysis of small and small-to-medium strain shear modulus of sands. *Computers and Geotechnics* **141**, 104518.

Ren, J., He, H. & Senetakis, K. (2021). A micromechanical-based investigation on the frictional behaviour of artificially bonded analogue sedimentary rock with calcium carbonate. *Pure and Applied Geophysics* **178**, No. 11, 4461–4486.

Rinaldi, V. & Santamarina, J. (2008). Cemented soils: small strain stiffness. *Deformational Characteristics of Geomaterials* **1**, No. 1, 267–273.

Riveros, G. A. & Sadrekarimi, A. (2020). Effect of microbially induced cementation on the instability and critical state behaviours of fraser river sand. *Canadian Geotechnical Journal* **57**, No. 12, 1870–1880.

Rothenburg, L. & Kruyt, N. P. (2004). Critical state and evolution of coordination number in simulated granular materials. *International Journal of Solids and Structures* **41**, No. 21, 5763–5774.

Salifu, E., MacLachlan, E., Iyer, K. R., Knapp, C. W. & Tarantino, A. (2016). Application of microbially induced calcite precipitation in erosion mitigation and stabilisation of sandy soil foreshore slopes: A preliminary investigation. *Engineering Geology* **201**, 96–105.

Saracho, A. C., Lucherini, L., Hirsch, M., Peter, H. M., Terzis, D., Amstad, E. & Laloui, L. (2021). Controlling the calcium carbonate microstructure of engineered living building materials. *Journal of Materials Chemistry A* **9**, No. 43, 24438–24451.

Senetakis, K. & Madhusudhan, B. (2015). Dynamics of potential fill–backfill material at very small strains. *Soils and Foundations* **55**, No. 5, 1196–1210.

Shahin, G., Desrues, J., Pont, S. D., Combe, G. & Argilaga, A. (2016). A study of the influence of REV variability in double-scale FEM× DEM analysis. *International Journal for Numerical Methods in Engineering* **107**, No. 10, 882–900.

Shahin, M., Jamieson, K. & Cheng, L. (2020). Microbial-induced carbonate precipitation for coastal erosion mitigation of sandy slopes. *Géotechnique Letters* **10**, No. 2, 211–215.

Shen, Z., Jiang, M. & Thornton, C. (2016). DEM simulation of bonded granular material. part I: contact model and application to cemented sand. *Computers and Geotechnics* **75**, 192–209.

Shi, X., Nie, J., Zhao, J. & Gao, Y. (2020). A homogenization equation for the small strain stiffness of gap-graded granular materials. *Computers and Geotechnics* **121**, 103440.

Shire, T., O'sullivan, C. & Hanley, K. (2016). The influence of fines content and size-ratio on the micro-scale properties of dense bimodal materials. *Granular Matter* **18**, No. 3, 1–10.

Sufian, A., Artigaut, M., Shire, T. & O'Sullivan, C. (2021). Influence of fabric on stress distribution in gap-graded soil. *Journal of Geotechnical and Geoenvironmental Engineering* **147**, No. 5, 04021016.

Tang, C.-S., Yin, L.-y., Jiang, N.-j., Zhu, C., Zeng, H., Li, H. & Shi, B. (2020). Factors affecting the performance of microbial-induced carbonate precipitation (MICP) treated soil: a review. *Environmental Earth Sciences* **79**, No. 5, 1–23.

Terzis, D., Bernier-Latmani, R. & Laloui, L. (2016). Fabric characteristics and mechanical response of bio-improved sand to various treatment conditions. *Géotechnique Letters* **6**, No. 1, 50–57.

Terzis, D. & Laloui, L. (2018). 3-D micro-architecture and mechanical response of soil cemented via microbial-induced calcite precipitation. *Scientific Reports* **8**, No. 1, 1416.

Terzis, D. & Laloui, L. (2019a). Cell-free soil bio-cementation with strength, dilatancy and fabric characterization. *Acta Geotechnica* **14**, No. 3, 639–656.

Terzis, D. & Laloui, L. (2019b). A decade of progress and turning points in the understanding of bio-improved soils: A review. *Geomechanics for Energy and the Environment* **19**, 100116.

Thornton, C. (2000). Numerical simulations of deviatoric shear deformation of granular media. *Géotechnique* **50**, No. 1, 43–53.

Tlili, M., Amor, M. B., Gabrielli, C., Joiret, S., Maurin, G. & Rousseau, P. (2002). Characterization of caco3 hydrates by micro-raman spectroscopy. *Journal of Raman Spectroscopy* **33**, No. 1, 10–16.

Utili, S. & Nova, R. (2008). DEM analysis of bonded granular geomaterials. *International Journal for Numerical and Analytical Methods in Geomechanics* **32**, No. 17, 1997–2031.

van Paassen, L. A. (2009). *Biogrout, ground improvement by microbial induced carbonate precipitation*. Ph.D. thesis, Delft University of Technology.

van Paassen, L. A., Ghose, R., van der Linden, T. J., van der Star, W. R. & van Loosdrecht, M. C. (2010). Quantifying biomediated ground improvement by ureolysis: large-scale biogrout experiment. *Journal of Geotechnical and Geoenvironmental Engineering* **136**, No. 12, 1721–1728.

Šmilauer, V. *et al.* (2021). *Yade Documentation 3rd ed.* The Yade Project, doi:10.5281/zenodo.5705394, http://yade-dem.org/doc/.

Wang, Y., Konstantinou, C., Soga, K., Biscontin, G. & Kabla, A. J. (2022). Use of microfluidic experiments to optimize MICP treatment protocols for effective strength enhancement of MICP-treated sandy soils. *Acta Geotechnica* , 1–22.

Wang, Y. & Leung, S. (2008a). Characterization of cemented sand by experimental and numerical investigations. *Journal of Geotechnical and Geoenvironmental Engineering* **134**, No. 7, 992–1004.

Wang, Y., Soga, K., Dejong, J. T. & Kabla, A. J. (2019). A microfluidic chip and its use in characterising the particle-scale behaviour of microbial-induced calcium carbonate precipitation (MICP). *Géotechnique* **69**, No. 12, 1086–1094.

Wang, Y.-H. & Leung, S.-C. (2008b). A particulate-scale investigation of cemented sand behavior. *Canadian Geotechnical Journal* **45**, No. 1, 29–44.

Wang, Y.-N., Li, S.-K., Li, Z.-Y. & Garg, A. (2023). Exploring the application of the micp technique for the suppression of erosion in granite residual soil in shantou using a rainfall erosion simulator. *Acta Geotechnica* , 1–13.

Weil, M. H., DeJong, J. T., Martinez, B. C. & Mortensen, B. M. (2012). Seismic and resistivity measurements for real-time monitoring of microbially induced calcite precipitation in sand. *Geotechnical Testing Journal* **35**, No. 2, 330–341.

Whiffin, V. S., van Paassen, L. A. & Harkes, M. P. (2007). Microbial carbonate precipitation as a soil improvement technique. *Geomicrobiology Journal* **24**, No. 5, 417–423.

Wichtmann, T., Triantafyllidis, T. *et al.* (2009). Influence of the grain-size distribution curve of quartz sand on the small strain shear modulus Gmax. *Journal of Geotechnical and Geoenvironmental Engineering* **135**, No. 10, 1404.

Worrell, E., Price, L., Martin, N., Hendriks, C. & Meida, L. O. (2001). Carbon dioxide emissions from the global cement industry. *Annual review of energy and the environment* **26**, No. 1, 303–329.

Wu, H., Wu, W., Liang, W., Dai, F., Liu, H. & Xiao, Y. (2023). 3D DEM modeling of biocemented sand with fines as cementing agents. *International Journal for Numerical and Analytical Methods in Geomechanics* **47**, No. 2, 212–240.

Wu, S., Li, B. & Chu, J. (2021). Stress-dilatancy behavior of MICP-treated sand. *International Journal of Geomechanics* **21**, No. 3, 04020264.

Xiao, P., Liu, H., Xiao, Y., Stuedlein, A. W. & Evans, T. M. (2018). Liquefaction resistance of bio-cemented calcareous sand. *Soil Dynamics and Earthquake Engineering* **107**, 9–19.

Xiao, Y., He, X., Zaman, M., Ma, G. & Zhao, C. (2022). Review of strength improvements of biocemented soils. *International Journal of Geomechanics* **22**, No. 11, 03122001.

Xiao, Y., Stuedlein, A. W., He, X., Han, F., Evans, T. M., Pan, Z., Lin, H., Chu, J. & van Paassen, L. A. (2021a). Lateral responses of a model pile in biocemented sand. *International Journal of Geomechanics* **21**, No. 11, 06021027.

Xiao, Y., Wang, Y., Wang, S., Evans, T. M., Stuedlein, A. W., Chu, J., Zhao, C., Wu, H. & Liu, H. (2021b). Homogeneity and mechanical behaviors of sands improved by a temperature-controlled one-phase MICP method. *Acta Geotechnica* **16**, No. 5, 1417–1427.

Xiao, Y., Zhao, C., Sun, Y., Wang, S., Wu, H., Chen, H. & Liu, H. (2021c). Compression behavior of MICP-treated sand with various gradations. *Acta Geotechnica* **16**, No. 5, 1391–1400.

Xu, W., Zheng, J., Chu, J., Zhang, R., Cui, M., Lai, H. & Zeng, C. (2021). New method for using N-(N-butyl)-thiophosphoric triamide to improve the effect of microbial induced carbonate precipitation. *Construction and Building Materials* **313**, 125490.

Xu, X., Guo, H., Cheng, X. & Li, M. (2020). The promotion of magnesium ions on aragonite precipitation in MICP process. *Construction and Building Materials* **263**, 120057.

Yang, J. & Gu, X. (2013). Shear stiffness of granular material at small strains: does it depend on grain size? *Géotechnique* **63**, No. 2, 165–179.

Yang, P., Kavazanjian, E. & Neithalath, N. (2019). Particle-scale mechanisms in undrained triaxial compression of biocemented sands: insights from 3D DEM simulations with flexible boundary. *International Journal of Geomechanics* **19**, No. 4, 04019009.

Yang, P., O'Donnell, S., Hamdan, N., Kavazanjian, E. & Neithalath, N. (2017). 3D DEM simulations of drained triaxial compression of sand strengthened using microbially induced carbonate precipitation. *International Journal of Geomechanics* **17**, No. 6, 04016143.

Yilmaz, Y., Deng, Y., Chang, C. S. & Gokce, A. (2023). Strength–dilatancy and critical state behaviours of binary mixtures of graded sands influenced by particle size ratio and fines content. *Géotechnique* **73**, No. 3, 202–217.

Yu, T., Souli, H., Péchaud, Y. & Fleureau, J.-M. (2022). Optimizing protocols for microbial induced calcite precipitation (MICP) for soil improvement–a review. *European Journal of Environmental and Civil Engineering* **26**, No. 6, 2218–2233.

Zeng, C., van Paassen, L. A., Zheng, J.-j., Stallings Young, E. G., Hall, C. A., Veenis, Y., Van der Star, W. R., Konstantinou, M. & Kavazanjian Jr, E. (2022). Soil stabilization with microbially induced desaturation and precipitation (MIDP) by denitrification: a field study. *Acta Geotechnica* , 1–16.

Zeng, C., Veenis, Y., Hall, C. A., Young, E. S., van Der Star, W. R., Zheng, J.-j. & van Paassen, L. A. (2021). Experimental and numerical analysis of a field trial application of microbially induced calcite precipitation for ground stabilization. *Journal of Geotechnical and Geoenvironmental Engineering* **147**, No. 7, 05021003.

Zeng, Y., Chen, Z., Lyu, Q., Cheng, Y., Huan, C., Jiang, X., Yan, Z. & Tan, Z. (2023). Microbiologically induced calcite precipitation for in situ stabilization of heavy metals contributes to land application of sewage sludge. *Journal of Hazardous Materials* **441**, 129866.

Zhang, A. & Dieudonné, A.-C. (2023a). Effects of carbonate distribution inhomogeneity on the improvement level of bio-cemented sands: A DEM study. In *International Conference of the International Association for Computer Methods and Advances in Geomechanics*, Springer, pp. 554–561.

Zhang, A. & Dieudonné, A.-C. (2023b). Effects of carbonate distribution pattern on the mechanical behaviour of bio-cemented sands: A DEM study. *Computers and Geotechnics* **154**, 105152.

Zhang, A. & Dieudonné, A.-C. (2024). Cementor: a toolbox to generate bio-cemented soils with specific microstructures. *Biogeotechnics* , 100081.

Zhang, A., Magnanimo, V., Cheng, H., Heimovaara, T. J. & Dieudonné, A.-C. (2024). DEM investigation into the small-strain stiffness of bio-cemented soils. *Submitted* .

Zhang, N., Yang, S., Xiong, L., Hong, Y. & Chen, Y. (2016). Nanoscale toughening mechanism of nacre tablet. *Journal of the Mechanical Behavior of Biomedical Materials* **53**, 200–209.

Zhang, X., Chen, Y., Liu, H., Zhang, Z. & Ding, X. (2020). Performance evaluation of a MICP-treated calcareous sandy foundation using shake table tests. *Soil Dynamics and Earthquake Engineering* **129**, 105959.

Zhou, Y., Liu, Q., Hu, M., Xu, G., Xu, R., Chong, X. & Feng, J. (2020). Investigation on the stability, electronic, optical, and mechanical properties of novel calcium carbonate hydrates via first-principles calculations. *International Journal of Quantum Chemistry* **120**, No. 10, e26219.

Zou, Z., Habraken, W. J., Matveeva, G., Jensen, A. C., Bertinetti, L., Hood, M. A., Sun, C.-y., Gilbert, P. U., Polishchuk, I., Pokroy, B. *et al.* (2019). A hydrated crystalline calcium carbonate phase: Calcium carbonate hemihydrate. *Science* **363**, No. 6425, 396–400.

Zuo, L. & Baudet, B. A. (2015). Determination of the transitional fines content of sand-non plastic fines mixtures. *Soils and Foundations* **55**, No. 1, 213–219.

# LIST OF FIGURES

# LIST OF PUBLICATIONS

## Journal Publications

- Zhang, A., Collin, F. & Dieudonné, A.C. Numerical insights into the post-peak strength of bio-cemented sands: a focus on the grain-bridging cementation pattern. *Under preparation.*

- Zhang, A., Magnanimo, V., Cheng, H., Heimovaara, T. J. & Dieudonné, A.C. DEM investigation into the small–strain stiffness of bio-cemented soils. *Under review.*

- Zhang, A. & Dieudonné, A.C. (2024). Cementor: a toolbox to generate bio-cemented soils with specific microstructures. *Biogeotechnics*, 100081.

- Zhang, A. & Dieudonné, A.C. (2023). Effects of carbonate distribution pattern on the mechanical behaviour of bio-cemented sands: A DEM study. *Computers and Geotechnics* **154**, 105152.

## Conference and Workshop

- Zhang, A. & Dieudonné, A.C. (2024). A small-strain stiffness model for bio-cemented sands. *IS-Grenoble: Geomechanics from Micro to Macro.* Selected as a theme lecture.

- Zhang, A. & Dieudonné, A.C. (2022). Effects of carbonate distribution inhomogeneity on the improvement level of bio-cemented sands: A DEM study. *International Conference of the International Association for Computer Methods and Advances in Geomechanics*; 554-561.

- Zhang, A. & Dieudonné, A.C. (2022). DEM study on the effect of carbonate distribution on the mechanical behaviour of bio-cemented sands. *International workshop on Bio- and Intelligent Geotechnics.*

- Zhang, A., Dieudonné, A.C. & Heimovaara, T. J. (2021). Insights into the impact of carbonate distribution pattern on the mechanical behaviour of bio-cemented sands. *ALERT Geomaterials Workshop 2021.*

- Li, L., Zhang, A. & Dieudonné, A.C. (2021). Constitutive modelling of bio-cemented soils: effect of cement spatial distribution. *ALERT Geomaterials*; 68.